# Controlled Nanostructuring by ALD:
# Thermoelectricity from low defects to high effects

Dissertation
zur Erlangung des Doktorgrades
des Department Physik
der Universität Hamburg

vorgelegt von

Sebastian Zastrow

geboren am 22. Oktober 1982 in Steinheim

Hamburg, den July 8, 2014

Universität Hamburg
DER FORSCHUNG | DER LEHRE | DER BILDUNG

"So every time I see some piece
of medical research saying that
caffeine is good for you, I
high-five myself. Because I'm
going to live forever."

## Abstract

The controlled implementation of nm-size inclusions, grains, interlayers or surfaces has become one of the key factor to design highly efficient thermoelectric materials. Atomic Layer Deposition (ALD) offers the possibility to functionalise the surface of 3D structures with a high surface to volume ratio. For the first time we present a systematic study of the electronic thermoelectric and galvanomagnetic properties of ALD grown $Sb_2Te_3$. The low deposition temperature of $80\,°C$ was used to photolithographically pattern a device to measure the Seebeck coefficient $S$, the electrical conductivity $\sigma$ as well as the Hall coefficient $R_H$ on the same film. A model has been developed to describe the thickness dependence of the transport properties due to the additional 2D conduction channel as well as surface scattering according to the Fuchs-Sondheimer model. To proof the concept of surface modifications of thermoelectric materials by ALD, a rotation flow-through/exposure mode particle reactor was build. The surface of $Bi_2Te_3$ particles has been covered with $Al_2O_3$ shells of varying thickness. The influence of the shell thickness on the thermoelectric properties (and $ZT$) have been systematically studied.

## Kurzzusammenfassung

Die kontrollierte Implementierung von nm-skaligen Defekten, Kristalliten, Zwischenlagen oder zusätzlichen Oberflächen hat sich als entscheidender Faktor für das Kreieren von hoch effizientem thermoelektrischem Material herausgestellt. Atomlagenabscheidung (ALD) bieten die Möglichkeit Oberflächen von beliebig geformten Strukturen mit hohen Oberflächen zu Volumen Verhältnis zu funktionalisieren. In dieser Arbeit werden zum ersten Mal die elektronischen thermoelektrischen und galvanomagnetischen Eigenschaften von ALD hergestelltem $Sb_2Te_3$ charakterisiert. Die niedrige Wachstumstemperatur von $80\,°C$ wurde genutzt, um photolithographisch eine Plattform zu strukturieren, die das Messen des Seebeck Koeffizienten $S$, der elektrischen Leitfähigkeit $\sigma$ und des Hall Koeffizienten $R_H$ an einer Schicht erlaubt. Ein Modell wurde eingeführt, das sowohl die Einflüsse eines 2D Transportkanals als auch die der Oberflächenstreuung gemäß der Fuchs-Sondheimer Gleichung vereint. Um die Effizienzsteigerung durch Oberflächenmodifikation von thermoelektrischem Material mittels ALD zu überprüfen, ist ein neuartiger Durchfluss/Infiltrations-Rotationsreaktor entwickelt worden. Mit diesem sind $Bi_2Te_3$ Partikel mit unterschiedlich dicken $Al_2O_3$ Schichten bedeckt worden. Der Einfluss der Dicke der $Al_2O_3$ Hülle auf die thermoelektrischen Eigenschaften (und $ZT$) wurde systematisch untersucht.

# Contents

# Nomenclature

## Symbols and constants

| Symbol | Description | Units |
|---|---|---|
| $\sigma$ | electrical conductivity | S/m |
| $\rho$ | electrical resistivity | $1/(\Omega \, \text{m})$ |
| $S$ | Seebeck coefficent | $\mu$/K |
| $\Pi$ | Peltier coefficent | V |
| $N$ | Nernst coefficient | V/(KT) |
| $\kappa$ | thermal conductivity | W/(mK) |
| $\kappa_e$ | electronic part of the thermal conductivity | W/(mK) |
| $\kappa_l$ | lattice part of the thermal conductivity | W/(mK) |
| $Z$ | thermoelectric figure of merit | 1/K |
| $PF$ | thermoelectric power factor | $\text{V}^2/(\text{K}^2\Omega \, \text{m})$ |
| $n$ | charge carrier concentration | $1/\text{m}^3$ |
| $\mu$ | charge carrier mobility | $\text{Vs}/\text{m}^2$ |
| $n_{\text{Hall}}$ | Hall carrier concentration | $1/\text{m}^3$ |
| $\mu_{\text{Hall}}$ | Hall carrier mobility | $\text{Vs}/\text{m}^2$ |
| $R$ | resistance | $\Omega$ |
| $V$ | voltage | V |
| $U$ | potential difference | V |
| $I$ | current | A |
| $H$ | magnetic field intensity | A/m |
| $B$ | magnetic field | T |
| $R_{\text{xx}}$ | longitudinal magneto resistance (LMR) | $\Omega$ |
| $R_{\text{xy}}$ | transversal magneto resistance (TMR) | $\Omega$ |
| $R_{\text{H}}$ | Hall coefficient | $\text{m}^3/\text{C}$ |
| $R_{\text{Hall}}$ | Hall resistance | $\Omega$/T |
| $V_{\text{te}}$ | thermovoltage | V |
| $T_{\text{hot}}$ | temperature on the hot side | K |

| $T_{\text{cold}}$ | temperature on the cold side | K |
| $T_{\text{ave}}$ | average temperature | K |
| $\eta$ | energy conversion efficiency | % |
| $\eta$ | reduced Fermi energy | – |
| $f_0$ | equilibrium distribution function | – |
| $f$ | distribution function | – |
| $g$ | density of state | $1/(\text{Jm}^3)$ |
| $E$ | energy | J |
| $E_{\text{F}}$ | Fermi energy | J |
| $\vec{k}$ | wave vector | 1/m |
| $\vec{r}$ | room coordinate | m |
| $v$ | average carrier velocity | m/s |
| $r$ | scattering parameter | – |
| $t$ | time | s |
| $t$ | thin film thickness | m |
| $\tau$ | relaxation time | s |
| $\tau_e$ | charge carrier relaxation time | s |
| $\tau_0$ | average charge carrier relaxation time | s |
| $m^*$ | carrier effective mass | kg |
| $m_{\text{dF}}$ | density of state effective mass | kg |
| $i$ | current flux/density | $\text{A/m}^2$ |
| $j$ | heat flux/density | $\text{W/m}^2$ |
| $\zeta$ | electric field | V/m |
| $\xi$ | reduced energy | – |
| $l_{\text{ph}}$ | phonon mean free path | m |
| $l_e$ | electron mean free path | m |
| $\tau$ | scattering time | s |
| $d_{\text{g}}$ | grain diameter | m |
| $R$ | grain boundary reflection coefficient | – |
| $p$ | surface scattering (specularity) factor | – |
| $r_{\text{H}}$ | Hall scattering factor | – |
| $D_{\text{hkl}}$ | crystalline grain size | m |
| $x$ | number of ALD cycles | – |
| $b$ | thin film width | m |
| $d$ | distance between device voltage contacts | m |
| $m$ | temperature scattering exponent | – |
| $\gamma_{\text{d}}$ | overall device thermal resistance | K/W |
| $G_{\text{2D}}$ | 2D (sheet) conductance | $1/\Omega$ |

| | | |
|---|---|---|
| $\sigma_{\text{bulk}}$ | bulk electrical conductivity | S/m |
| $\sigma_{\text{3D}}$ | calculated $\sigma$ with the FS-model | S/m |
| $\sigma_{\text{2D}}$ | sheet conductivity | S/m |
| $S_{\text{tot}}$ | calculated $S$ | μV/K |
| $S_{\text{3D}}$ | $S$ contribution of the 3D bulk channel $S$ | μV/K |
| $S_{\text{2D}}$ | $S$ contribution of the 2D surface channel $S$ | μV/K |
| $n_{\text{3D}}$ | $S$ volume carrier concentration | $1/m^3$ |
| $n_{\text{2D}}$ | $S$ sheet carrier concentration | $1/m^2$ |
| $L$ | Lorenz factor | WΩ/K$^2$ |
| $C$ | specific heat capacity | J/(kg·K) |
| $C_m$ | molar heat capacity | J/(mol·K) |
| $\rho_{\text{m}}$ | molar heat capacity | kg/m$^3$ |
| | | |
| $k_{\text{B}}$ | Boltzmann-constant: $1.38 \cdot 10^{-23}$ | J/K |
| $e$ | elementary charge: $1.60 \cdot 10^{-19}$ | C |
| $h$ | Planck constant: $6.63 \cdot 10^{-34}$ | Js |
| $\mu_0$ | magnetic constant: $4\pi \cdot 10^{-7}$ | N/A$^2$ |
| $L_0$ | Lorenz number $\approx 2.44 \cdot 10^{-8}$ | WΩ/K$^2$ |

## Acronyms

| | |
|---|---|
| FWHM | full width half maximum |
| PIXE | particle induced X-Ray emission |
| TEG | thermoelectric generator |
| RTG | radioisotope thermoelectric generator |
| ALD | atomic layer deposition |
| CVD | chemical vapour deposition |
| MBE | molecular beam epitaxy |
| VLS | vapour liquid solid |
| SPS | spark plasma sintering |
| DHP | direct hot pressing |
| GST | germanium(Ge)antimon(Sb)telluride(Te) |
| PCM | phase-change memory |
| AAO | anodized aluminum oxide |
| TMA | trimethylaluminium |
| BTE | Boltzmann transport equation |
| UPC | upper conduction regime |
| LCR | lower conduction regime |

| | |
|---|---|
| UVB | upper valence band |
| LVB | lower valence band |
| LMR | longitudinal magneto resistance |
| TMR | transversal magneto resistance |
| SdH | Schubnikov-de Haas |
| WAL | weak anti-localisation |
| AFM | atomic force microscope |
| EDX | energy dispersive X-Ray spectroscopy |
| XRD | X-Ray diffraction |
| SEM | scanning electron microscope |
| TEM | tunnel electron microscope |
| LFA | laser flash analysis |
| UHV | ultra high vacuum |
| WL | weak localisation |
| TI | topological insulator |
| VB | valence band |
| CB | conduction band |
| AC | alternating current |
| DC | direct current |
| RT | room temperature |

# Chapter 1

# Introduction and motivation

The field of thermoelectrics has a relatively long tradition in physics. Since Thomas Johann Seebeck first observed the influence of temperature gradients in conductors in 1821, not more than 200 years have past. He found that, in a closed circuit of two metals with a temperature difference at it's contact points, a magnetic field can be observed [1]. A short time later the origin of the magnetic field was, according to Ampere's circuital law, found to be an electric current driven by the heat flow. In 1834 Jean C. A. Peltier discovered the vice versa effect, that an electrical current can cause a temperature gradient between both ends of the junction [2, 3]. This time was the birth of thermoelectricity. Since then, a lot of progress has been made to describe the cross link between heat and charge transfer. Magnus *et al.* discovered that the Seebeck coefficient does not depend on the temperature distribution along the materials, which [4]. Later, the (stationary) solutions found of the Boltzmann's transport equation (BTE), devised by Ludwig Boltzmann in 1872, were able to describe most thermoelectric phenomena (see e.g. [5, 6]). Additionally, E. Becquerel experimentally discovered the Seebeck coefficient of many materials and compounds (see e.g. [7]). A lot of the materials analysed by Becquerel are still under discussion in terms of their thermoelectric performance [8]. Another big peak for the research on thermoelectric materials was in the 1950's and 60's. Here Goldsmid, Ioffe and others were able to describe the (anisotropic) electronic transport of efficient thermoelectric materials like $Bi_2Te_3$, $Sb_2Te_3$ and their solid solutions [9, 10]. But also general studies in the field of semiconductors by D. A. Wright, the supervisor of Goldsmid, and others have made great progress in describing transport phenomena which are the basis of many transport theories and also a special motivation for this work [11, 12]. By improvements in the fabrication of single crystalline semiconducting materials, the progress in building higher powered magnets and low temperature cryostats, researchers were able to have a deeper look into electronic transport properties of solid state materi-

als. The thermoelectric material development of this time has found it's application in the field of radioisotope thermoelectric generators (RTG's) in NASA-projects like the Apollo missions[1] and the deep space explorers - the Voyager probes. On earth the developed materials are used in Peltier-Elements (cooling devices), for example in portable refrigerators. Although thermoelectric devices have found some applications, only a small number of scientific publications in this field can be found from the 1970's to the 1990's, where the interest starts to rise again. Inspired by the upcoming field of nanostructuring, new theories on thermoelectric transport in low dimensional (<3D) structures were developed. These predicted enhancements in the conversion efficiency of heat differences into electrical energy by increasing the thermoelectric figure of merit ($ZT$) [13]. Especially for supperlattice structures based on materials with two different band gaps, a remarkable increase of $ZT$ was predicted. Indeed a few years later first groups were able to show this enhancements by measurements on nanometer-sized structures like on Si/SiGe or PbTe/PbSeTe-superlattices [14–17]. On the other hand, one of the highest $ZT$ value measured on $Sb_2Te_3$/$Bi_2Te_3$ superlattices and published by Venkasubramanian ($ZT$=2.4), is waiting to be reproduced [18, 19]. And there is a good reason for that:

Thermoelectric materials with high $ZT$-values in general have a complex electronic structure. Goldsmid for example showed, that a high thermoelectric efficiency is connected to multivalley band-structures with a high anisotropy [6]. This means, that the simplified transport equations often cannot describe the electronic behaviour of such materials sufficiently, because the assumption of, e.g. single bands and a parabolic band structure are not valid. But these simplifications are often used to derive theoretical solutions for high $ZT$-materials. Additionally, if the material is amorphous or polycrystalline, the transport properties are sums over all crystal directions, which makes it even harder to describe the electronic properties of "real" materials. Because the foreign element concentration in thermoelectric materials is often very high for a dopand (>$10^{19}$ cm$^{-3}$), they can not be assumed as classical semiconductors, but more like semimetals. However, the absolute contents of admixed elements or compounds is often in a range in which they are hardly detectable (<1%) with standard element content evaluation techniques like for example energy-dispersive X-Ray spectroscopy (EDX). The "real" composition often stays in the dark. Therefore a good understanding of the basic, undoped material is necessary to study their behaviour in general and to learn which parameters influence the transport properties.

Atomic Layer Deposition (ALD) is a well developed method for producing thin films, especially of oxide materials like for example the ALD model system $Al_2O_3$ [20, 21].

---

[1] The experimental RTG (SNAP) was designed to act as power supply for the Apollo Lunar Surface Experiments Package (ALSEP).

This self-limiting, chemical process gives an excellent control of the stoichiometry and the thickness of the deposited material even in non flat structures with high aspect ratios [22]. However, the deposition rate is very low, so that even depositing some tens of nanometers could take days if complex structures have to be infiltrated. Because of this, ALD has mostly been used for producing very thin but high insulating layers, e.g. in the silicon solar cell production and on three-dimensional topographies for electronic devices [23, 24]. There is a lot of progress in developing new chemicals to produce different compounds by ALD [22, 24]. For this work, the development of the precursor chemistry for producing tellurium-based materials was highly motivating. This processes originally have been designed to produce layers on 3D structures for electronic devices like phase-change memory (PCM). These devices are using the properties of chalcogenide materials, like for example GeSbTe (GST), to switch between a high resistivity amorphous and a high conductive crystalline phase by slow or fast cooling [25, 26]. Here is the link to thermoelectrics. $Sb_2Te_3$ - which is possible to deposit by ALD since Pore *et al.* developed this process in 2009 - is also a standard thermoelectric p-type material due to it's peak performance at room temperature (RT). In this work, the first time known to the author, the electronic thermoelectric properties of ALD grown $Sb_2Te_3$ thin films have been systematically evaluated, to study the potential of ALD films of thermoelectric materials to create conformal coated complex 3D nanostructures. There are three major motivations to use ALD to deposit $Sb_2Te_3$:

(1): Tellurium is a very rare element in the earth crust. This makes it is not only very expensive but also very limitedly available. A cautious sustainable use of Tellurium is necessary. Functionalise only the surface of nanostructures by ALD can greatly reduce the consumption of tellurium.

(2): The deposition temperature is very low. This expands not only the number materials on which $Sb_2Te_3$ can be deposited, it also decreases the amount of energy which is necessary for the synthesis. Because the defect formation energy is decreasing with temperature, the produced $Sb_2Te_3$ thin films are expected to have nearly perfect stoichiometry. This can be an important advantage to study the transport properties of pure $Sb_2Te_3$, since the defect concentration is found to be naturally high in this material [27].

(3): ALD can cover nanostructures of nearly any geometry. There are several publications on nanograined $Bi_{2-x}Sb_xTe_3$ which show an enhancements of the thermoelectric figure of merit $ZT$, by reducing the lattice thermal conductivity due to the increased phonon scattering at the grain boundary surfaces. This was the motivation to produce core shell structures by depositing $Al_2O_3$ and $Sb_2Te_3$ on $Bi_2Te_3$ with ALD. For this special application a new flow-through type particle reactor is designed and build up which is presented in this work.

# Chapter 2

# Thermoelectrics

Thermoelectric (TE) effects describe the influence of the heat flow on the charge carrier and vice versa. If two dissimilar conductors (*a* and *b*) are connected thermally parallel and electrically in series (see figure 2.1), an electric potential differential (thermovoltage $V_{te}$) can be measured in the open circuit when a temperature difference ($\Delta T$) is applied at the junctions of this circuit (thermocouple), known as the **Seebeck effect**. This thermovoltage, driven by the heat flow, arises when the charge carriers with lower energy pass from material *a* to the material *b* in which their energy state is higher (see figure 2.1 (a)) [6]. The differential Seebeck coefficient under open circuit conditions is defined as [5]

$$S_{ab} = \frac{\mathrm{d}V}{\mathrm{d}T}. \tag{2.1}$$

In the case of actual measurements, one has to take into account, that the Seebeck coefficients are in general temperature dependent. However, for reasonable small temperature gradients the Seebeck coefficient can be approximated with

$$S_{ab}(T_{ave}) = \frac{V_{te}}{T_{hot} - T_{cold}} = \frac{V_{te}}{\Delta T}, \tag{2.2}$$

where $T_{ave}$ is defined as the corresponding average temperature at which $S_{ab}$ is measured. In reverse to the Seebeck effect, a temperature difference between the junctions can be measured, if a current $I$ is applied to the circuit, what is called **Peltier effect** (see figure 2.1 (b)). Due to the energy difference of the electrons passing from one material to the other, heat energy is rejected/absorbed from the reservoirs. The heat rate exchange $Q$ between the junctions is defined as [5]
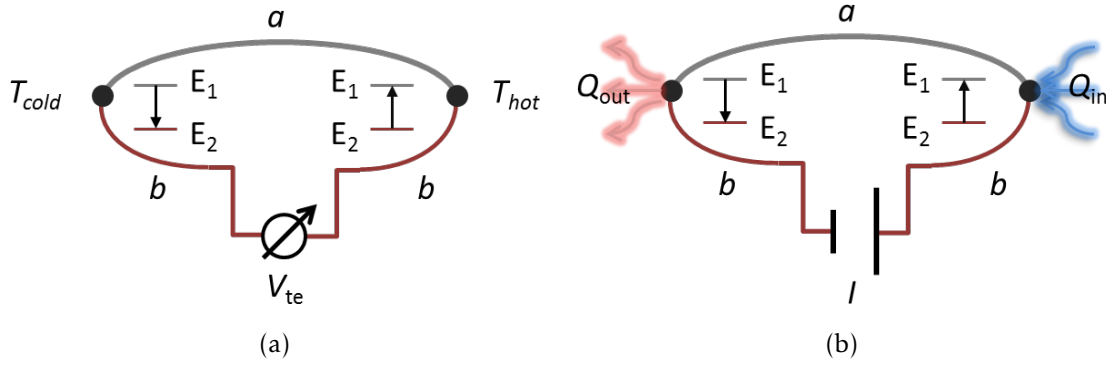
$$Q = \Pi_{ab}I, \tag{2.3}$$

**Figure 2.1:** (a) Seebeck effect: A thermovoltage $V_{te}$ arises in the junctions of material $a$ and $b$, forced by a temperature difference of $\Delta T = T_{hot} - T_{cold}$. (b) Peltier effect: Heat absorption $Q_{in}$ and liberation $Q_{out}$ in the junctions of the thermocouple, driven by the current $I$.

with the Peltier coefficient $\Pi_{ab}$. As the third of the thermoelectric effects, the **Thomson effect** describes the rate of heat generation $q$ in a conductor with the current density $i$ and an applied temperature gradient $\frac{dT}{dx}$

$$q = \beta i \frac{dT}{dx}, \tag{2.4}$$

where $\beta$ is the Thomson coefficient. The effect is small compared to Joule heating and therefore not easy to measure. However, in principle it is possible to derive the Seebeck coefficient by integrating the Thomson coefficient over the temperature

$$\beta = T \frac{dS}{dT}. \tag{2.5}$$

All the thermoelectric effects discussed are in general dependent on magnetic fields $B$ [28]. In the presence of a magnetic field $B_z$, a transverse electric field $E_y$ arises from the longitudinal temperature gradient, called **Nernst effect**:

$$|N| = \frac{E_y}{B_z} \left( \frac{dT}{dx} \right)^{-1}, \tag{2.6}$$

with the Nernst coefficient $|N|$. The process connected to the Peltier effect is called **Ettinghausen effect**. A transverse temperature gradient arises in a conductor with a longitudinal current $I_x$ applied [28]:

$$|P| = \frac{1}{I_x B_z} \left( \frac{dT}{dy} \right)^{-1}, \tag{2.7}$$

where $|P|$ is the Ettinghausen coefficient.

## 2.1 Thermoelectric devices, materials, and the efficiency problem

There are two major applications for the use of thermoelectric effects in solid state materials: The conversion of heat energy (by a temperature difference) into electrical energy (**thermoelectric generators**) and vice versa: the use of electrical energy to create a temperature gradient (**thermoelectric coolers**). In principle both devices look the same (see figure 2.2). Thermoelectric generators, which convert heat to electrical
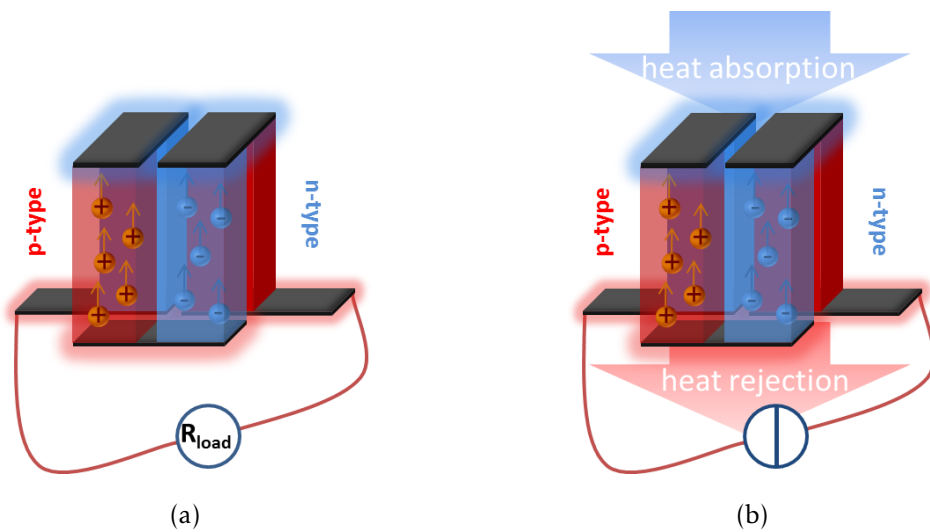


**Figure 2.2:** Figure (a) shows four legs of a thermoelectric generator. If a temperature difference is applied (with two reservoirs) a consumer can be driven. Figure (b) shows the application using the vice versa effect - a principle of a Peltier element. If a current is applied, on one side heat of the reservoir can be absorbed and will be rejected on the other side.

energy, are based on the Seebeck effect. If a temperature gradient is applied between the two ends of a material, a voltage can be measured. To drive a consumer, two different materials are necessary. In thermoelectric devices, the materials are usually chosen to be one p- and one n-type conductor to maximise the total voltage output of such a device. In the Peltier-mode, mostly used as cooling device, a current is applied which forces the heat flow from one side to the other.

For most applications, the efficiency of a TE-device is the key-parameter. In actual devices, factors like the temperature gradient, contact resistances and many more have to be taken into account. However, beside these technical problems, the maximum efficiency $\eta$ is determined by the thermoelectric parameters of the materials. These parameters are concluded in the dimensionless figure of merit ($ZT$)

$$ZT_{\text{ave}} = \frac{S^2 \sigma}{\kappa} T_{\text{ave}}, \tag{2.8}$$

where $S$ is the Seebeck coefficient [V/K], $\sigma$ the electrical conductivity [S/m] and $\kappa$ the thermal conductivity [W/(m·K)]. $T_{\mathrm{ave}}$ is the average temperature of the hot and the cold side of the device. With this factor, the ideal energy conversion coefficient of a material is given by [10]:

$$\eta = \frac{T_{\mathrm{hot}} - T_{\mathrm{cold}}}{T_{\mathrm{hot}}} \cdot \frac{\sqrt{1 + Z T_{\mathrm{ave}}} - 1}{\sqrt{1 + Z T_{\mathrm{ave}}} + \frac{T_{\mathrm{hot}}}{T_{\mathrm{cold}}}}. \tag{2.9}$$

The thermoelectric efficiency matches the Carnot efficiency if $Z \to \infty$. Actual available thermoelectric materials show a $ZT$ factor of around 1 which corresponds to an efficiency of about 10% [1] if the ratio of $T_{\mathrm{hot}}$ to $T_{\mathrm{cold}}$ is equal to 0.5 [29]. Beside this theoretical case, recent studies claim that the number of industrial applications will be tenfold increased, if $ZT \geqslant 2$ [29]. The ideas for reaching this value will be discussed in chapter 3.

## 2.2 Thermoelectric transport in the Boltzmann picture

In quantum theory the probability for a charge carrier occupying a state of energy $E$ is given by the equilibrium Fermi-Dirac statistic [6]:

$$f_0(E(\vec{k}), T) = \frac{1}{\exp\left(\frac{E - E_{\mathrm{F}}}{k_{\mathrm{B}} T}\right) + 1}, \tag{2.10}$$

where $E_{\mathrm{F}}$ is equal to the chemical potential at $T = 0$, $k$ is the wave vector and $k_{\mathrm{B}}$ is the Boltzmann constant. There are three mechanisms which can change the equilibrium distribution function [30]:

- (i) diffusion because of regional differences in the electron density

- (ii) the presence of external fields

- (iii) electron collisions

We have to expand the equation with a room- ($\vec{r}$) and time-coordinate ($t$) to describe the deflection of the equilibrium function. With the use of Liouville's theorem of constant density in the phase-space and with substitution of the energy by the wave vector, we get, in the absence of collision [30]:

$$f(\vec{k} + \mathrm{d}\vec{k}, \vec{r} + \mathrm{d}\vec{r}, t + \mathrm{d}t) - \vec{f}(\vec{k}, \vec{r}, t) = 0. \tag{2.11}$$

---

[1] by assuming temperature independent thermoelectric properties and negligible power losses from the device

In the presence of collision, a correction term has to be added which is approximated with the relaxation time-approach:

$$\frac{\partial f}{\partial t}_{\text{collusion}} = -\frac{f(\vec{k}) - f_0(\vec{k})}{\tau_e(\vec{E})} \tag{2.12}$$

with the relaxation time $\tau_e$, which is approximated to be a function of the energy $E$ and the scattering parameter $r$:

$$\tau_e = \tau_0 E^r. \tag{2.13}$$

The scattering parameter $r$ is a function of the dominant scattering mechanism, i.e. $r$ is equal to -1/2 in the case of acoustic phonon scattering, or $r = 3/2$ for ionised impurity scattering. However, with respect to Matthiessen's rule (see equation 3.3), the relaxation times are reciprocal additive. This can lead to mixing scattering factors between the discrete values, making it difficult to distinguish between different scattering mechanisms with only looking at the scattering parameter.

Since we have addressed possible deflections of the equilibrium distribution function, we can find the **Boltzmann equation** by differentiating equation 2.12 with respect to the time [30]

$$\vec{k} \cdot \frac{\partial f}{\partial \vec{k}} + \vec{r} \cdot \frac{\partial f}{\partial \vec{r}} = \frac{\partial f}{\partial t}_{\text{collusion}} = -\frac{f(\vec{k}) - f_0(\vec{k})}{\tau_e(\vec{E})}. \tag{2.14}$$

To obtain the solution for the case of an applied temperature gradient and an electric field, one can use the linear (Boltzmann) approximation for small deflexions $|f - f_0| << f_0$, with

$$\frac{\partial f_0}{\partial \vec{r}} = \frac{\partial}{\partial \vec{r}} \left( \frac{1}{\exp\left(\frac{E - E_F}{k_B T}\right) + 1} \right) \tag{2.15}$$

$$= -\frac{\partial f_0}{\partial E} \left( \frac{\partial E_F}{\partial \vec{r}} + \frac{E - E_F}{T} \right) \frac{\partial T}{\partial \vec{r}}, \tag{2.16}$$

and

$$\frac{\partial f}{\partial \vec{k}} \cong \frac{\partial f_0}{\partial E} \frac{\partial E}{\partial \vec{k}} \tag{2.17}$$

$$= \frac{\partial f_0}{\partial E} \vec{v}. \tag{2.18}$$

If we assume the fields and flows only in the x-direction, which is a reasonable assumption in the case of polycrystalline materials, we can find [5, 6, 30]

$$\frac{f(E) - f_0(R)}{\partial \tau_e} = v_x \frac{\partial f_0}{\partial E} \left( \frac{\partial E_F}{\partial x} + \frac{E - E_F}{T} \frac{\partial T}{\partial x} \right). \tag{2.19}$$

The energy is measured as distance downwards from the top of the valence band for hole- and upwards from conduction band for electron energies [5]. We can now define the current density $j$ and the heat density $q$. With the density of state $g(E)$, the number of charge carriers per unit volume in the range $E + dE$ to $f(E)g(E)dE$ and using the carrier velocity $v$ (and elementary charge $e$), the current density for electrons (-) or holes (+) is [6]:

$$i = \pm e \int_0^\infty v f(E) g(E) dE, \tag{2.20}$$

and the heat density:

$$j = \pm \int_0^\infty (E - E_{\mathrm{F}} f(E) g(E) dE. \tag{2.21}$$

Since the thermal velocity is always greater then the drift velocity in the regime of interest, the charge carrier velocity can be assumed to be isotropic and therefore to be $1/3$ of the mean square velocity $v$ [5, 30]. For this case, the energy dependence $E$ of $v_{\mathrm{x}}$ is given by:

$$v_{\mathrm{x}}^2 = \frac{2}{3} \frac{E}{m^*}, \tag{2.22}$$

where $m^*$ is the effective mass corresponding to the band structure. The equilibrium distribution function $f_0$ does not contribute to the heat and charge flow. We can replace $f$ by $f - f_0$ and insert equation 2.19 and 2.22 in 2.20:

$$i = \mp \frac{2e}{3m^*} \cdot \int_0^\infty \tau_e E g(E) \frac{\partial f_0}{\partial E} \left( \frac{\partial E_{\mathrm{F}}}{\partial x} + \frac{E - E_{\mathrm{F}}}{T} \frac{\partial T}{\partial x} \right) dE, \tag{2.23}$$

and

$$j = \pm \frac{E_{\mathrm{F}}}{e} \cdot i + \frac{2e}{3m^*} \cdot \int_0^\infty \tau_e E^2 g(E) \frac{\partial f_0}{\partial E} \left( \frac{\partial E_{\mathrm{F}}}{\partial x} + \frac{E - E_{\mathrm{F}}}{T} \frac{\partial T}{\partial x} \right) dE. \tag{2.24}$$

Setting the temperature gradient $\frac{\partial T}{\partial x} = 0$ one can find the expression for the electrical conductivity $\sigma$ with the electrical field $\zeta = \pm \frac{1}{e} \cdot \frac{\partial E_{\mathrm{F}}}{\partial x}$

$$\sigma = \frac{i}{\zeta} = -\frac{2e^2}{3m^*} \cdot \int_0^\infty \tau_e E g(E) \frac{\partial f_0}{\partial E} dE, \tag{2.25}$$

and with the boundary condition of no current flow ($i = 0$), we can find the expression for Seebeck coefficient $S = \frac{1}{e} \frac{\partial E_{\mathrm{f}}}{\partial x} \left( \frac{\partial T}{\partial x} \right)^{-1}$ to be

$$S = \pm \frac{1}{eT} \cdot \left[ E_{\mathrm{F}} - \int_0^\infty \tau_e E^2 g(E) \frac{\partial f_0}{\partial E} dE \cdot \left( \int_0^\infty \tau_e E g(E) \frac{\partial f_0}{\partial E} dE \right)^{-1} \right]. \tag{2.26}$$

The electronic part of the thermal conductivity $\lambda_e$ is given by $j \cdot \frac{\partial T}{\partial x}$. With the use of equation 2.23 and 2.24, $\lambda_e$ can be find to be

$$
\kappa_e = \frac{2}{3m^*T} \left\langle \left[ \left( \int_0^\infty \tau_e E^2 g(E) \frac{\partial f_0}{\partial E} \mathrm{d}E \right)^2 \left( \int_0^\infty \tau_e g(E) \frac{\partial f_0}{\partial E} \mathrm{d}E \right)^{-1} \right] \right.
$$
$$
\left. - \int_0^\infty \tau_e E^3 g(E) \frac{\partial f_0}{\partial E} \mathrm{d}E \right\rangle.
\tag{2.27}
$$

Since all integrals in the equations 2.25, 2.26 and 2.27 have the same form, it is possible to express the transport coefficients with general integrals. If we use the relaxation time approximation from equation 2.13 and the density of state $g(E)$ approximation for parabolic bands[2] near the band minimum or maximum (for small values of $E$ and $k$) [5]

$$
g(E) = \frac{4\pi(2m^*)^{3/2}}{h^3} |E|^{1/2} \mathrm{d}|E|,
\tag{2.28}
$$

we can write the general integrals to [6]

$$
K_s = -\frac{2T}{3m^*} \cdot \int_0^\infty \tau_e E^{s+1} g(E) \frac{\partial f_0}{\partial E} \mathrm{d}E
\tag{2.29}
$$
$$
= \frac{8\pi}{3} \left( \frac{2}{h^2} \right)^{3/2} (m^*)^{1/2} T\tau_0(s + r + 3/2)(k_B T)^{s+r+3/2} F_{s+r+1/2},
\tag{2.30}
$$

where $F_n$ are the Fermi-Dirac integrals

$$
F_n(\xi, E_F) = \int_0^\infty \xi f_0(\xi, E_F) \mathrm{d}\xi,
\tag{2.31}
$$

with the reduced energy $\xi = \frac{E}{k_B T}$. The Fermi-Dirac integrals can be solved numerically. Typically the values are given for the different values of the reduced Fermi-energy $\chi = \frac{E_F}{k_B T}$ see e.g. [5, 6]. We can now express the electronic thermoelectric coefficients necessary for the calculation of $ZT$:

$$
\sigma = \frac{e^2}{T} K_1
\tag{2.32}
$$
**electrical conductivity**

$$
S = \frac{1}{T^2} \left( K_2 - \frac{K_1^2}{K_0} \right)
\tag{2.33}
$$
**Seebeck coefficient**

---

[2]Which is similar to the free-electron expression, but taking the electron-lattice interaction into account by replacing the electron mass $m_e$ with the effective mass $m^*$.

$$\lambda_e = \pm \frac{1}{eT} \left( E_\text{F} - \frac{K_1}{K_0} \right) \tag{2.34}$$

**electrical thermal conductivity**

The expressions highlight the fact, that in general the electronic thermoelectric properties can not be seen as independent variables. However the solution for every material system ($v$, $r$ and $m^*$) has to be solved individually, it is possible to make general statements for limited cases of $\chi$. In the case of $E_\text{F} << 4k_\text{B}T$, which is in the regime of metals and degenerate semiconductors, one can expand the Fermi-Dirac integrals and find [6]

$$S = \pm \frac{\pi^3}{3} \frac{k_\text{B}}{e} \frac{k_\text{B}T \cdot (r + 3/2)}{E_\text{F}} = \pm \frac{\pi^3}{3} \frac{k_\text{B}}{e} \frac{(r + 3/2)}{\chi}. \tag{2.35}$$

In the case of large $\chi$, $S$ becomes small (in the range of $\mu$V/K) and linear in $T$ which reflects the behaviour of metals. If we expand the Fermi-Dirac integrals for small $\chi < -2/k_\text{B}T$, for non-degenerate semiconductors, the expression of $S$ in the Boltzmann picture can be found to be

$$S = \pm \frac{k_\text{B}}{e} \left( \frac{k_\text{B}T}{E_\text{F} - r - \frac{5}{2}} \right). \tag{2.36}$$

## 2.3 Crystal and electronic structure $\text{Bi/Sb}_2\text{Te}_3$

Since the early 1950's, $\text{Bi/Sb}_2\text{Te}_3$ and their compounds have been intensively studied, focusing on their good thermoelectric characteristics at room temperature [28,31–34]. To understand the thermoelectric and galvanomagnetic transport properties of the chalcogenide $\text{V}_2 - \text{VI}_3$ group materials, one has to have a closer look to the crystal structure of these material group. Both alloys have a tetradymite crystal structure (space group $D_{3d}^5 - R\overline{3}m$) with five atoms per unit cell (two Sb/Bi and three Te) [35]. The lattice parameters are given in table 2.1. The crystal lattice of $\text{Bi/Sb}_2\text{Te}_3$ forms periodic quintuple layers (QL) perpendicular to the trigonal c-axis [36]. Each layer consists of the element stacking of

$$...\text{Te}(2) - \text{Bi/Sb} - \text{Te}(1) - \text{Bi/Sb} - \text{Te}(2)...^3,$$

with predominantly ionic-covalent bonds inside the QL (Te(1)) and weak van der Waals bonding between the Te(2) layers (see figure 2.3 (a)) [35, 37]. In this hexagonal description (see table 2.1), the unit cell contains 15 atoms with 3 QL's [38]. This exceptional crystal structure obviously leads to anisotropic electronic transport prop-

---

[3]The signifier (1) and (2) denote the different bonding mechanisms.

| compounds | unit cell | a [nm] | $\Theta[°]$ | c [nm] |
|---|---|---|---|---|
| Bi$_2$Te$_3$ [39] | tetradymite | 1.0473 | 24.17 | - |
| Sb$_2$Te$_3$ [39] | tetradymite | 1.0447 | 23.55 | - |
| Bi$_2$Te$_3$ [40] | hexagonal | 0.43835 | - | 3.36 |
| Sb$_2$Te$_3$ [41] | hexagonal | 0.4275 | - | 3.49 |

**Table 2.1:** Lattice constants of Bi/Sb$_2$Te$_3$ in the tetradymite and in the hexagonal unit cell. References can be found in the row compounds.

erties [28, 33, 42]. In reference to the main results of this work, the emphasis of the following discussion will be on the electronic structure of Sb$_2$Te$_3$. Beside the complex crystal structure, Sb$_2$Te$_3$ also has a complex band structure with two six-valley valence bands leading to six Fermi surfaces for the upper- (UVB) and the lower valance band (LVB) respectively. Kulbachinskii *et al.* studied the electronic band structure of intrinsic and doped Sb$_2$Te$_3$ single crystals grown by the Bridgman method [43]. Although he was not able to separate the assumed Fermi surfaces with Shubnikov-de Haas (SdH) effect measurements, he observed four different relaxation times by measuring the photoinduced transient thermoelectric effect (TTE). These have different mobilities and effective masses, two for each, the UVB and LVB (see figure 2.3). Depending on the position of the Fermi energy $E_\mathrm{F}$ relative to the valance band maximum $E_\mathrm{VBM}$, the anisotropy of the electrical conductivity $\sigma_{zz}/\sigma_{xx}$ can be of several one-digit numbers [38]. However, the anisotropy of the Seebeck coefficient is measured to be relatively small ($S_\perp/S_\parallel \approx 1.2$) [28].

The actual casting of stoichiometric Sb$_2$Te$_3$ with a perfect ratio of 40 at. % Sb and 60 at. % Te can be very challenging. Due to the layered structure and the low bond polarity between Sb and Te (electronegativities of $X_{\mathrm{Sb}}$=1.9 and $X_{\mathrm{Te}}$=2.1), Sb$_2$Te$_3$ has a high ability to form antisite (antistructural) defects where Sb atoms occupy a Te lattice position [43, 44]. This small energy barrier for this element exchange leads to a off-stoichiometry of Sb$_2$Te$_3$ with an excess of Sb. As consequence, to the best knowledge of the author, this compound is always found to be "natural" p-doped, independent from the cast method. Even in single crystal cast Sb$_2$Te$_3$ with very high purity initial elements (5N), a Hall hole concentration of minimum $10^{24}\,\mathrm{m}^{-3}$ but more often $10^{26}\,\mathrm{m}^{-3}$ is found [35, 43, 45].

van der Waals bonds

van der Waals bonds

• Bi/Sb
• Te(2)
• Te(1)

(a)

c-axis ⊗

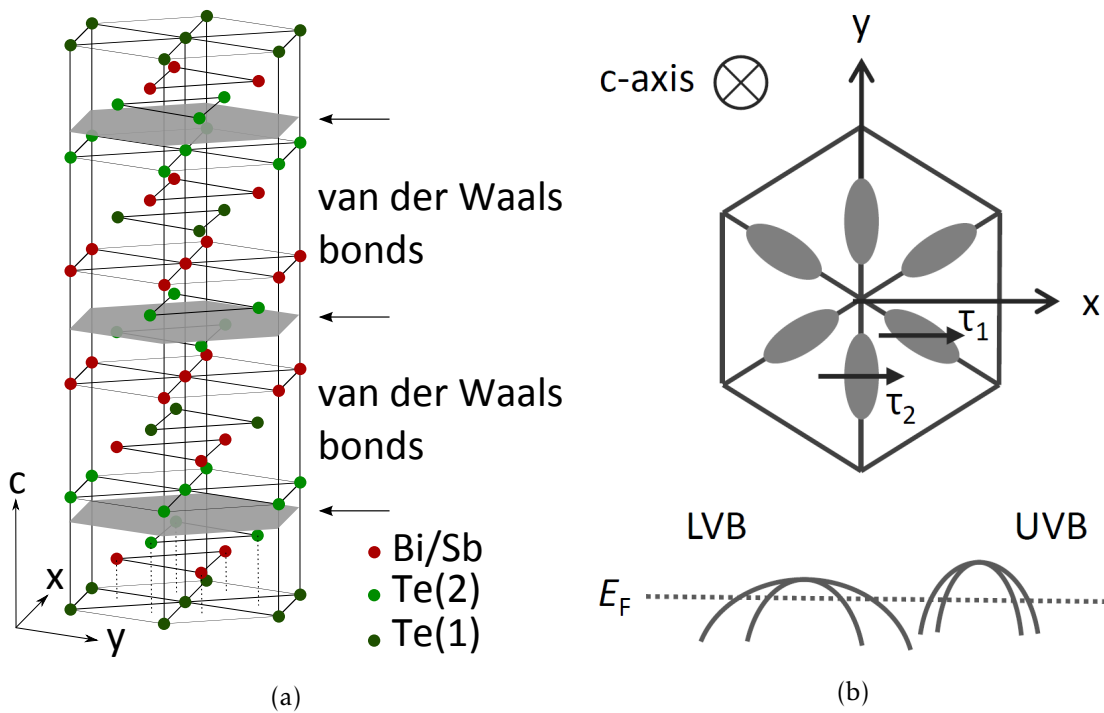$\tau_1$

$\tau_2$

LVB

UVB

$E_F$

(b)

**Figure 2.3:** (a) The hexagonal cell of $Bi/Sb_2Te_3$ with four quintuples separated by van der Waal gaps between two Te(2)-layers. The weak polar bonds between the Te-Sb forces the ability to form antisite defects $Sb_{Te}$ leading to a "natural" p-doping of $Sb_2Te_3$. (b) The Fermi surfaces in the x-y-plane, assumed to be isotropic along the c-axis [43]. The lower figure is a scheme of the the UVB and LVB, where two different scattering times $\tau_i$, as it has been found in [43].

# Chapter 3

# Nanostructuring and Thermoelectrics

Nanostructuring and enhanced/optimized thermoelectric performance are two synonyms often used together in headers of scientific publications. "Optimisation" and "Enhancing" refer to describe two major aspects of creating "good" or "excellent" thermoelectric material properties:

- Increasing the thermoelectric figure of merit $ZT$ relative to the "as cast" materials. This means either improving the Seebeck coefficient $S$, the electrical conductivity $\sigma$ or both ($PF$) - or decreasing the (lattice) thermal conductivity $\kappa$, in a specific temperature regime.

- Shifting the maximum of the thermoelectric figure of merit $ZT$ to a temperature regime which is, in the authors point of view, interesting for applications.

Both can be necessary if the material should be used in Peltier- or thermoelectric power-devices. Now we have named what is meant, when we talk about optimisation or enhancement of thermoelectric materials, we have to discuss what this means for the physical parameters. Since the Seebeck coefficient, the electrical conductivity and the electronic part of the lattice thermal conductivity are determined by the electron/hole transport behaviour, this three parameters are linked (see equations 2.32, 2.33 and 2.34). Therefore it is generally not possible to influence only one of them without effecting the other two. However, there are ways to improve $ZT$ by just changing the ratio of them, because the Seebeck coefficient accounts with the power of two in the $ZT$-factor and $S$ and $\sigma$ are generally not linear scaled (see figure 3.1). The optimisation of the power factor $S^2\sigma$ is often done by manipulating the majority carrier concentration with either doping or slightly changing the ratio of elements of the chosen compounds (variation of the stoichiometry). General calculations shown a power
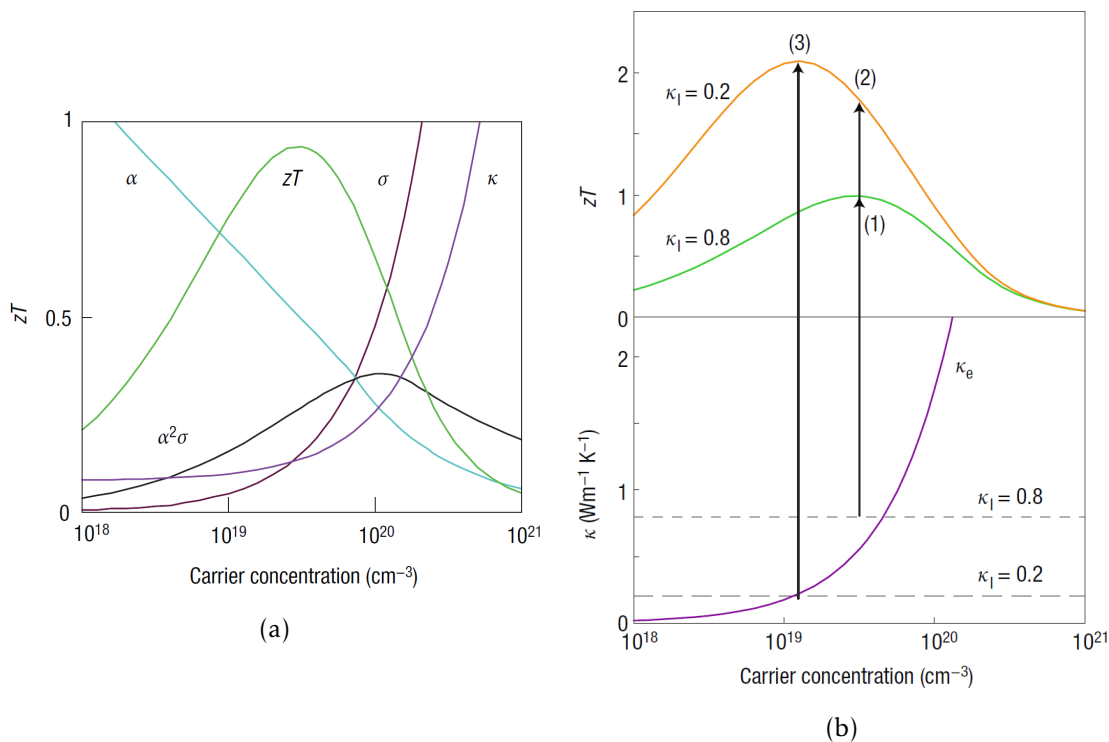
(a)

(b)

**Figure 3.1:** (a) The thermoelectric figure of merit $ZT$ and the dependent parameters as a function of the charge carrier concentration. (b) Thermal conductivity as a function of carrier concentration. The reduction of the lattice thermal conductivity $\kappa_l$ can significantly increase $ZT$ (from point (1) to (2)). This allows a re-optimization to lower carrier concentrations, higher Seebeck values and therefore a higher $ZT$ (point (3)). Trends bases on empirical data for $Bi_2Te_3$ of [46]. From: "Complex thermoelectric materials," by G. Jeffrey Snyder and Eric S. Toberer, 2008, *Nature Materials 7*, p. 105 - 114, 2013 by Nature. Reprinted with permission.

factor (and $ZT$) maximum for carrier concentrations[1] in the range of $10^{18}$ - $10^{21}\,\mathrm{cm^{-3}}$, which are typically values of heavily doped semiconductors and of course dependent on the material/compound [47, 48]. This effect can be reached without nanostructuring and is more a material science aspect.

An further approach to increase the thermoelectric figure of merit is to decrease the thermal conductivity $\kappa$. At thermoelectric advisable charge carrier concentrations, electrons and phonons contribute approximately equal to the total thermal conductivity. The phonon thermal conductivity, often called lattice thermal conductivity $\kappa_l$, has different scattering probabilities in contrast to those of charge carrier scattering. To distinguish between $\kappa_l$ and the charge carrier thermal conductivity $\kappa_e$, a new ex-

---

[1]More precisely it is determined by the Fermi energy $E_\mathrm{F}$.

pression of the thermoelectric figure of merit can be defined (see equation 2.8) to

$$ZT_{\text{ave}} = \frac{S^2 \sigma}{\kappa_l + \kappa_e} T_{\text{ave}}. \tag{3.1}$$

Ioffe *et al.* suggests, that a solid solution of two semiconductors with the same crystal structure can decrease $\kappa_l$ by increasing the phonon scattering probability, but without affecting the charge carrier transport [6, 10]. This is due to the fact, that the phonon mean free path is usually greater then these of charge carriers, which makes it possible to influence the short wavelength phonons, predominating the heat transport, without destroying the long range order of electrons and holes [6]. However, it turned out that also the mid- to long wavelength modes of the phonon spectrum contribute significantly to the heat transport. Different scattering mechanisms influencing the charge carrier and phonon transport will be discussed in the following sections.

## 3.1 Phonon scattering: Nanostructures and the influence on phonon transport

If we include the lattice thermal conductivity $\kappa_l$ in our calculations (see equation 3.1), the effect of nanostructuring can influence phonon transport and therefore the thermoelectric figure of merit $ZT$. In principle it should be possible to modify $\kappa_l$ without effecting the electronic transport properties [6, 10]. Of course the charge carriers interact with phonons and therefore the electronic properties are physically not completely disconnected, but an optimisation is possible since phonons and electrons have different energy-frequency dispersions and mean free paths. One of the strategies to reduce $\kappa_l$ is to lower the specific heat (lowering the phonon density of states) and average group velocity phonons (shape of the dispersion relation) [49]. This means forming nanostructures (e.g. superlattices or low dimensional structures) with sizes in the range or smaller than the phonon mean free path $l_{\text{ph}}$ in parallel to the transport direction. An decrease of the thermal conductivity using this approach has been demonstrated for example with an Ge/Si superlattices structures [50] and Si nanowires [51] or a combination of both [52]. However the principle of decreasing $\kappa_l$ by this method has been proven since the average phonon mean free path in this elements is comparably large, these relatively pure materials have a poor thermoelectric performance due to their unoptimised carrier concentrations. For applications around room temperature, alloys of $V_2VI_3$ Bi/Sb and Te compounds are, up to now, still the best thermoelectric materials available ($ZT \approx 1$). To reach such effects in this compounds, nanostructuring in the order of the mean free path of phonons in this material systems would be necessary. These can be found to be around an order

of magnitude lower then in Si/SiGe, which means only a few nm at room temperature [49]. However it is challenging to reach such regimes in $Bi_2Te_3$, $Sb_2Te_3$ and their alloys, there are size effects on a larger length scale which can lead to an increase of phonon scattering by e.g. lattice defects, interfaces and grain boundaries.

**Interface, point defect and grain boundary phonon scattering - classical size effects**

Interface scattering is efficient if the interface layers are rough or/and have a large acoustic mismatches [49]. The impact on the mean free path of this scattering mechanism $l_{ph}^{ib}$ has to be weighted with all mean free paths ($l_{ph}^i$) contributing to the total mean free path $l_{ph}^{tot}$ by using the Matthiessen rule [48, 49]

$$\frac{1}{l_{ph}^{tot}} = \sum_{i=1}^{n} l_{ph}^i = \frac{1}{l_{ph}^{imp}} + \frac{1}{l_{ph}^{ib}} + \frac{1}{l_{ph}^{uk}}..., \tag{3.2}$$

where the dominant scatterers listed here are impurity/alloy or defect scattering $l_{ph}^{imp}$ and phonon-phonon Umklapp scattering $l_{ph}^{uk}$. Note that equation 3.2 is only a rough approximation since all mean free paths depend on the phonon frequency $\nu$ and generally are anisotropic (especially $l_{ph}^{ib}$ strongly depends on the 3D-layer or grain structure).

Since the crystal structure and therefore the phonon transport is anisotropic, grains with different lattice directions can create interfaces without adding different elements or alloys to the structure. This fact is used in the ball milling approach, where optimised thermoelectric materials are fine grained by the impact energy of the added balls, under heavy rotation of the beakers. After the milling process the powder has to be compacted, which is typically done by SPS (Spark Plasma Sintering - a current is induced to heat up the material during the pressing process) or via conventional hot pressing (the pressing shell is heated up - no current flow through the sample). Performance increases due to reduced lattice thermal conductivity by this method have been shown for example by Poudel *et al.* who reached a $ZT$ value of 1.4 for ball milled $(Bi, Sb)_2Te_3$ [53].

Because of the large length scale compared to the (average) phonon mean free path, interface and grain boundary scattering are only sufficient for the low frequency (and therefore long mean free path) phonon contribution to the lattice thermal conductivity [6]. In contrast to this, point defect scattering effects the high frequency (small mean free path) components of phonon-frequency dispersion relation. Defect scatterers are for example local variations of the elastic constant and the density in isomorphous crystals by vacancies or impurities in compounds [5, 6]. However there are

several kinds of approaches to create phonon scatterers, the general condition that phonons should be scattered more sufficiently then charge carriers, should be fulfilled [54, 55]. The combination of the ball milling process and the covering of these particles with a shell of a different material to increase the effect of surface scattering seems to be a promising next step to enhance phonon scattering. Therefore it is necessary to conformal cover the particles with thin shells before pressing. This is the major asset of Atomic Layer Deposition (ALD), which will be introduced in the the next chapter.

## 3.2 Charge carrier scattering: Nanostructures and the influences on the electron transport

Now that we have discussed the influence of size effects in nanostructures on the phonon transport, it is of course necessary to think about the charge carrier transport in such systems. Since the mean free path as well as the frequency dispersion relation is different for charge carriers and phonons, one would expect different structure size effects. In this section some of the dominant scattering mechanisms in systems in which at least one dimension is in the order of the carrier mean free path $l_e$ will be discussed. On the basis of the emphasis of this work, we will focus on the effects in thin films where one dimension (the thickness $t$) fulfil this requirement. However, these size effects are expected to influence the carrier transport in system with more then one reduced dimensions, e.g. nanowires or nanoribbons, too.

### 3.2.1 Grain boundary and surface scattering - classical size effects

In the most cases when $Bi/Sb_2Te_3$ thin films are grown, the structure consists of plane parallel, but randomly oriented polycrystallites, rather than being single crystalline [56, 57]. This is due to the island growth behaviour of such material systems, which is typical for $Sb_2Te_3/Bi_2Te_3$ thin film growth, independent from the method used (see section 4.2 and [57–65]). The growth mechanism starts with the formation of non connected islands, which grow together with increasing amount of deposited material. As a consequence, these islands are the origin of the grains in thicker (closed) films, leading to the polycrystallinity of such thin films. The boundaries of these grains are determined by the surfaces of two different crystal directions facing at each other at their common borders. Of course the disturbance of the lattice orientation is expected to show deviations from single crystal bulk transport due to the additional scattering. Mayadas and Shatzkes *et al.* formulated a model, which describes the quantitative

influence of grain boundary scattering on the charge carrier transport [66]. This leads to a modification of the total scattering time $\tau^*$ by obeying Matthiessen's rule

$$\frac{1}{\tau^*} = \frac{1}{\tau} + \frac{1}{\tau_{\mathrm{gb}}}, \qquad (3.3)$$

where $\tau$ is the background scattering time, caused by defects, impurities and phonon scattering and $\tau_{gb}$ is the grain boundary scattering time. Mayadas and Shatzkes obtained a geometry factor $\alpha$, which describes the relation of the average grain size diameter $d_{\mathrm{g}}$ in relation to the electron mean free path $l_{\mathrm{e}}$ combined with the grain boundary reflection coefficient $R$ [57]

$$\alpha = \frac{l_{\mathrm{e}}}{d_{\mathrm{g}}} \cdot \frac{R}{1 - R}. \qquad (3.4)$$

The modification to the electrical conductivity $\sigma_{\mathrm{bulk}}$ can then be found to be [57]

$$\sigma_{\mathrm{gb}} = \sigma_{\mathrm{bulk}} \cdot 3 \cdot \left[ \frac{1}{3} - \frac{1}{2}\alpha + \alpha^2 - \alpha^3 \ln\left(1 + \frac{1}{\alpha}\right) \right]. \qquad (3.5)$$

As an additional scattering source for charge carriers in thin films, collisions of electrons/holes with the film surface may have to be taken into account if the thickness of the film is in the order of the electron mean free path $l_e$ [57]. The increase of the electrical resistivity or the decrease of the electrical conductivity has been described by Sondheimer[2] *et al.* [67, 68]. In fact the analytic solution of the equation is complicated and we will limit the discussion to a more simplified (qualitative) solution. This is adequate, since the quantitative boundary conditions of the different scattering parameters are not known and therefore an analytic solution is not possible. However, the basic parameters which affect the surface scattering mechanisms shall be introduced here. In figure 3.2 a scheme of the scattering mechanism and the parameters are shown. The surface scattering depends on the mean free path $l_{\mathrm{e}}$ with respect to the film thickness $t$ and the probability of scattering. This probability factor $p$ in general is a function of the surface roughness. In the case of a totally smooth film surface, the interface scattering has no influence on the conductivity since the carriers do not loose any momentum in the direction of the current flow (estimated to be one dimensional perpendicular to the film axis), due to the fact that the scattering is fully specular (see figure 3.2 dotted grey line). On the other hand, if the surface has a certain roughness, the assumption of a horizontal interface is not longer valid. As a consequence the charge carriers are diffusive scattered and loose momentum in the direction of the charge flow - reducing the electrical conductivity. If the ratio of $t/l_{\mathrm{e}} > 1$, the expression for the reduced conductivity $\sigma_{\mathrm{FS}}$ as a function of the background conductivity

---

[2]First attempts for surface scattering has been done by Thomson *et. al.* and later by Fuchs *et al.* how solved the Boltzmann transport equation for such surface scattering [57,67].
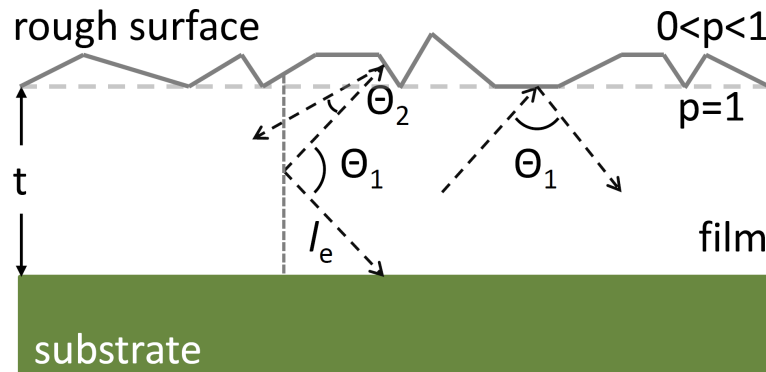
**Figure 3.2:** Scheme of the surface scattering mechanism and the influence of the surface roughness on the scattering probability factor $p$. The grey dotted line corresponds to fully specular scattering in the case of a totally smooth film surface ($p$=1) and the diffusive scattering in the case of a rough surface (solid grey line; $0 < p < 1$).

$\sigma_\mathrm{bulk}$ can be calculated to[3] [61]

$$\sigma_\mathrm{FS} = \sigma_\mathrm{bulk} \left[ 1 - \frac{3}{8} \frac{l_\mathrm{e}}{t} (1 - p) \right],$$ (3.6)

known as the Fuchs-Sondheimer model. The factor $p$ is the surface scattering factor, linked to the amount of charge carriers scattered either fully specular ($p$=1) or fully diffuse ($p$=0). Of course this equation is simplified, since the scattering probability as well as the mean free path are function of the frequency of the carriers. However $p$ and $l_e$ are means, this model is able to make a quantitative description of the reduction of the electrical conductivity in thin films with respect to the surface roughness and the thin film thickness [57].

### 3.2.2 Quantum confinements effects

Quantum confinement effects in thermoelectric materials are under steady debate. Several publications describe different quantum confinement effects in low dimensional structures and the effect on the thermoelectric transport properties - see e.g. [69–71]. Since in this work the thermoelectric properties of thin films and core shell structures are discussed, we will concentrate on the two dimensional calculations. The highly cited paper of Hicks *et al.* from 1993 predicted a strong increase of the thermoelectric figure of merit $ZT$ by quantum size effects in 2D superlattice structures [13]. In a simple cubic lattice with a single parabolic band structure and an energy inde-

---

[3]Das *et al.* mentioned that numerical calculations have shown, that this function is valid for ratios down to $t/l_\mathrm{e} \approx 0.1$ [61]

pendent scattering time $\tau$, the electronic energy dispersion relation is given by [13]

$$E(k_x, k_y, k_z) = \frac{\hbar^2}{2} \left( \frac{k_x^2}{m_x} + \frac{k_y^2}{m_y} + \frac{k_z^2}{m_z} \right), \tag{3.7}$$

where $k_i$ are the momentums given by the inverse of the lattice constant $a$ ($k_i = \frac{1}{a}$) and $m_i$ are the effective masses for the respective lattice direction. If we now confine the free electron dispersion in one direction by an infinite potential barrier (in the following along the z-direction) by reducing the thickness to nm scale, the dispersion relation is modified to [13]

$$E(k_x, k_y, k_z) = \frac{\hbar^2}{2} \left( \frac{k_x^2}{m_x} + \frac{k_y^2}{m_y} + \frac{\pi^2}{m_z t^2} \right), \tag{3.8}$$

where $t$ is the layer thickness. This is the energy dispersion of an infinite width film (along the x-y plane). The energy dispersion along the the x-y plane is still continuous, but discrete along the z-axis. The energy levels are now split up into several subbands with the energy dependence of $E_z \propto \frac{1}{t^2}$. Since the density of state $g(E)$ is a function of the energy dispersion $E(\vec{k})$, the Fermi energy $E_F$ and the Fermi-Dirac distribution $f$, all electronic parts of the thermoelectric properties are influenced by this quantum confinement effect. This leads to the effect, that the Fermi energy (and therefore all electronic transport properties) can be influenced by tuning for example the doping level and the layer thickness $t$. In the case of $Bi_2Te_3$ these calculations predict a significant increase of the $ZT$ value for a layer thickness below 4 nm [13].

However, these theoretical calculations have limitations: They assume only one subband of the confined z-direction bands contribute to the electronic transport. This limitation is only valid if the separation of the subbands is large (meaning very small $t$) and $E_F$ is lower then the relative energy level of the second subband, which strongly depends on the majority carrier concentration.

# Chapter 4

# Atomic Layer Deposition

Atomic Layer Deposition (ALD) bases on non reversal gas-solid-reactions of at least two vapour chemicals (so called: precursors or reactants) alternate pulsed into a reaction chamber and separated with a purge step by flushing with inert gas e.g. nitrogen, a conformal thin film is produced by the chemical reaction between the different vapours [24]. The precursors are chemically designed to react only with each other, leading to a self-limiting process. This means that the growth of the film is not linked to the exposure time (after saturation of the surface has taken place) in which the chemical is left in the reaction chamber, but only by the repetitions of the process. Once the start precursor material has reacted with the surface, the classical ALD-process shows a constant growth rate (layers per cycle) and therefore an excellent thickness control on nearly every three-dimensional surface is possible [22]. The basic scheme of a two precursor ALD cycle step is shown in figure 4.1. Starting with the pulse of precursor one (I), the chemical reacts with the surface atoms (in general with the OH-group on the top of the substrate material) forming the nucleation layer (II). The volatile gas-solid reaction produces by-products (often called: waste-gas) containing these parts of the precursor chemicals which do not form the solid compound. To get rid of this waste-gas and the non-reacted precursor gas, a purge step is done by flushing the chamber with a small flow of inert gas or just by evacuating it (II). This step is necessary to prevent any gas-gas reaction between the non reacted precursor materials or the waste-gas and the following precursor two. When the second precursor is in contact with the surface (III), it reacts with the first layer material. After this, the first layer of the compound is formed and the cycle begins once again (IV).

Let us conclude the properties of ALD growth. On the one hand, the deposition method has some major advantages:

- Deposition not only on flat substrates, it is also possible to conformally coat 3D-
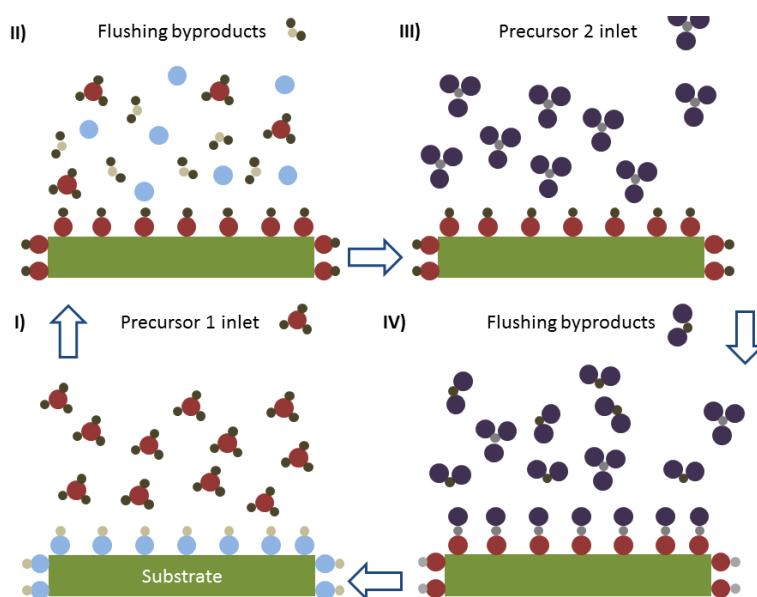
**Figure 4.1:** Scheme of a 2 precursor ALD cycle starting with the substrate-first-precursor-reaction (I).

structures with high aspect ratios.

- Excellent thickness controllability due to the self-limiting reaction.

- High material purity because of the defined chemical reaction and the low deposition temperature.

- No need for ultra high vacuum which simplifies the ALD-machine design.

On the other hand, there are disadvantages:

- Low deposition rates - typically in the range of 0.01 - 2 Å/cycle, while one cycle can take seconds in the case of coating flat substrates or several minutes when complex structures have to be infiltrated.

- The list of elements and compounds which can be deposited is limited to the precursor chemistry, but the list increases fast in the last 10 years (for a list of precipitable compounds and elements see e.g. [24]).

- Not every surface material can be coated without surface activation.

In contrast to the ALD of metal-oxides (e.g. $Al_2O_3$, $SiO_2$ or $TiO_2$), where the processes are well established, the information about the deposition of chalcogenides is very limited.

This leads to the question: Why is ALD a good method to produce $Sb_2Te_3$ thin films? First of all a very precise method established to conformally coat particles with thin

film shells, especially $Sb_2Te_3$. On the other hand there is also a good reason to characterise the galvono- and thermoelectric properties of ALD grown thin films of this materials on flat substrates: In comparison to other deposition techniques, this method has a very low deposition temperature (see fig. 4.2), which is expected to suppress the formation of defects in such material compounds. In the case of the research on
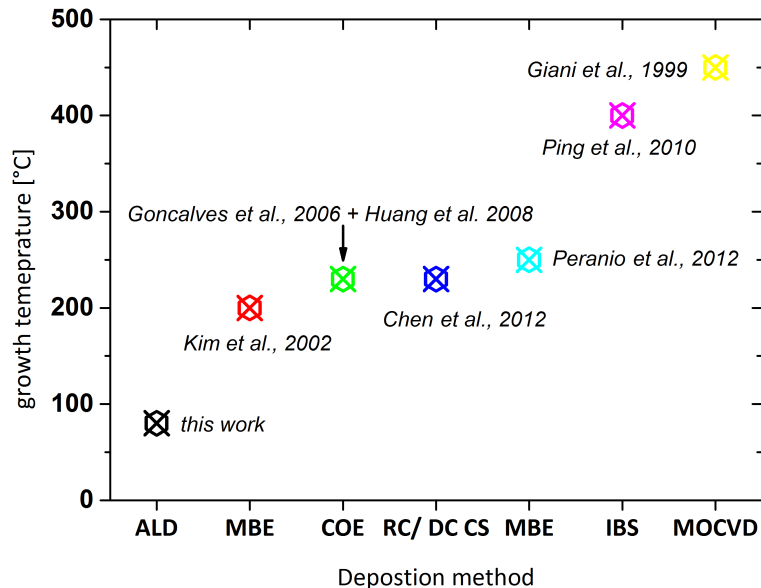


**Figure 4.2:** This figure shows some examples of the growth temperature of different thin film deposition techniques. This list not intended to be exhaustive. MBE - molecular beam epitaxy [72, 73]. COE - co-evaporation [58, 74]. RC/DC CS - radiofrequency (RF) and direct current (DC) co-sputtering [75]. IBS - ion beam sputtering deposition [76]. MOCVD - metal organic chemical vapour deposition [60].

$Sb/Bi_2Te_3$ and its compounds, this could be of vital importance:

The production of pure antimony/bismuth-telluride in its 2:3 phase is a major problem. Due to the weak polarity of the Sb/Bi-Te bonding this kind of material system often forms so called antistructural defects which lead to a shift of the stoichiometry [77]. This means a Sb/Bi atom can occupy an Te position or the other way a round. The negatively charged antistructural defects are compensated by a high hole concentration, making $Sb_2Te_3$ grown under stoichiometric conditions nearly always a p-type conductor [77]. A lot of effort has been put into the challenge to produce stoichiometric $(Sb/Bi)_2Te_3$ with a low defect content, e.g. via post-annealing under Te-atmosphere [78–80]. Because the formation of solid $Sb_2Te_3$ in the ALD process results from a chemical reaction (see eq. 4.1) and the deposition temperature is low (which means a lower energy in the system to form antistructural defects) compared to other deposition techniques, there are good chances to get a lower defect concentration in the produced films. But the biggest advantage from the low deposition temperature

is the possibility to pre-structure the ALD thin film via photolithography techniques. This will be discussed in the chapter 5.

## 4.1 Design, concept and realisation of ALD-reactors

Several different types of ALD-reactors are commercially available and a lot of self-made or modified reactors can be found in the field of research and development, all build and optimized for their special field of application [81–84]. Since all samples presented in this work originate from two self-made ALD-reactors, the special concept of each will be presented in this section. All deposition parameters specific to this work are for these machines only and can differ widely if the same process is run on other ALD-reactors. Nevertheless, there is one generally important rule which should be obeyed designing an ALD-machine:

Precursor-gas flow should only be possible in the direction of the vacuum pump without risk of condensation. This can be assured by the following steps:

- A constant inert gas (carrier gas) flow from the precursor line into the direction of the reaction chamber.

- Keeping a positive heat gradient from the precursor bottles (lower $T$) to the reaction chamber (higher $T$).

- Always separate the precursor-gases from each other to prevent inadvertent reactions.

### 4.1.1 Boost modification on home-made exposure reactor

The exposure-reactor is originally designed and build for the deposition onto porous nanostructures, especially for creating nanotubes and nanowires by depositing in self-assembled aluminium-oxide membranes (AAO-membranes), see e.g. [85, 86]. The term "exposure" means, that the precursor can be kept in the reaction chamber for a determined time, letting the precursor gases penetrate (by gas diffusion) structures with high aspect ratios. In the case of thin film depositions on flat substrates, this time can be chosen to be very short, because the surface is easily accessible by the reactant gases. The time and pressure scheme in figure 4.3 illustrates a basic two precursor process with in the exposure modus. In principle, there are two precursor valves (valves **2** and **3** in figure 4.4) which control the flow of reactant gas (the basic ALD-process is illustrated in figure 4.1). A flowmeter guarantees a constant flow of the inert gas, so that no reflux of gas from the chamber into the valve- and precursor-line is possible.
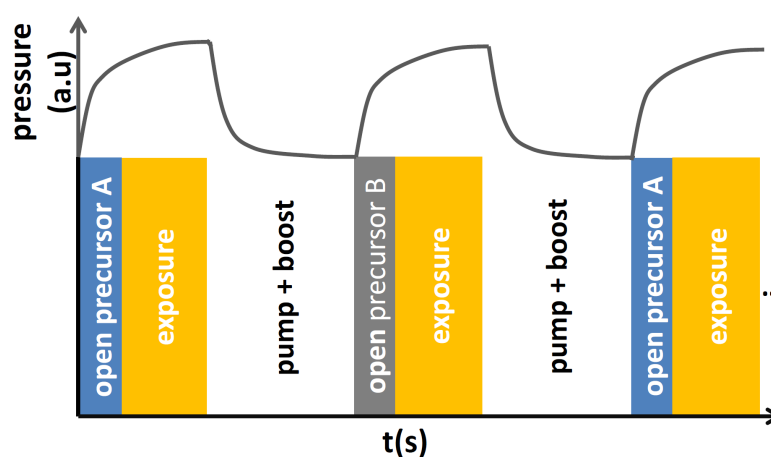
**Figure 4.3:** Pressure and time scheme for a two precursor ALD-cycle.

The valves **1** and **4** have been installed later to increase the base pressure in the precursor container bottles because of the following reasons:

The vapour pressure of the two precursor chemicals are very low at the chosen temperature. This leads to the problem, that the pressure difference between the precursor container and the reaction chamber is too low to have an adequate amount of reactant gas in the chamber. Since the growth rate strongly decreases with increasing temperature (see figure 4.8 and [25]) and the precursor chemicals tend to decompose at higher temperatures, the precursor temperature has to be as low as possible. To support the precursor-gas-flow, the pressure difference between the chamber and the precursor container is increased by a certain pressure - controlled by the *Boost pressure regulator* (see figure 4.4 - of inert gas ($N_2$ or Ar)). Therefore, the ALD machine has been modified by installing additional valves, which have to control the gas pulses between the boost pressure regulator and the precursor bottles (see figure 4.4). The inert gas boost is done during pumping (valve **5** open), when the line between the precursor container and the chamber is closed (when valve **1** as well as **3** are closed and **1** or **4** are open). For a more detailed view of the process, please compare table 4.1 and figure 4.4.

### 4.1.2 Boost flow-through/exposure particle-reactor

Creating core/shell micro- and nano-particles by coating with ALD, for the passivation or functionalisation of particle surfaces as well as for tuning optical or mechanical properties of materials, is becoming a rising field in research for various applications [21, 87–89]. For the conformal and homogeneous coverage, it is absolutely necessary that every part of the surface has the same probability for the chemical pre-
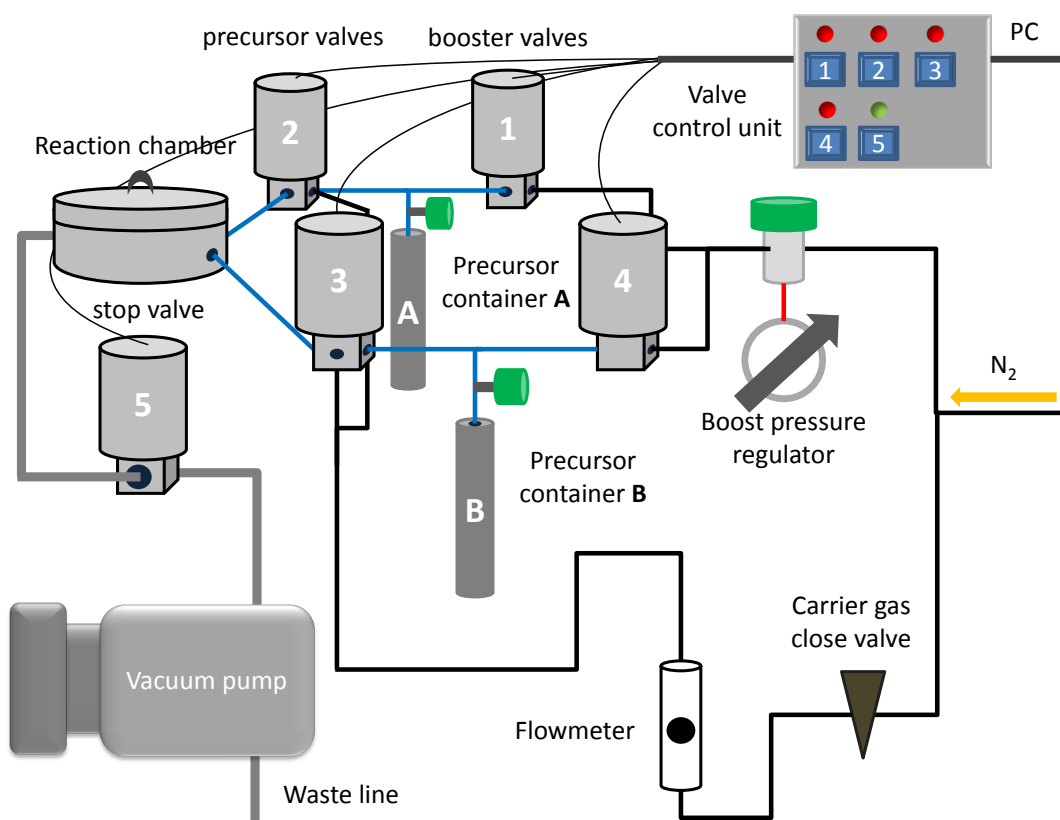
**Figure 4.4:** Scheme of the modified home made exposure-mode ALD-reactor with boost mode.

| # | step name | precursor | valves open | valves closed |
|---|-----------|-----------|-------------|---------------|
| 0 | pump + boost | A | 5,1 | 2,3,4 |
| 1 | open | A | 2 | 1,3,4,5 |
| 2 | exposure | - | - | all |
| 3 | pump+boost | B | 5, 4 | 1,2,3 |
| 4 | open | B | 3 | 1,2,4,5 |
| 5 | exposure | - | - | all |
| 6 | goto 0 | - | - | all |

**Table 4.1:** A basic boost-ALD recipe for one cycle. The boost valve open time is always shorter then the pump time.

cursor reaction. In principle there are two reactor designs which are able to ensure such coating: the fluidized bed and the rotary reactor (see figure 4.5). The concept of the fluidized bed reactor is adapted from the CVD coating process [90, 91]. The particles are kept in levitation by a constant flow of carrier and/or precursor gases. This flow has to be optimized for the density and size of the specific particles to avert either flushing them in the waste gas line or, if the gas flow is too low to overcome the gravitational force, that the particles stay on the ground. On the one hand, this process has

**Rotary reactor**    **Fluidized bed reactor**
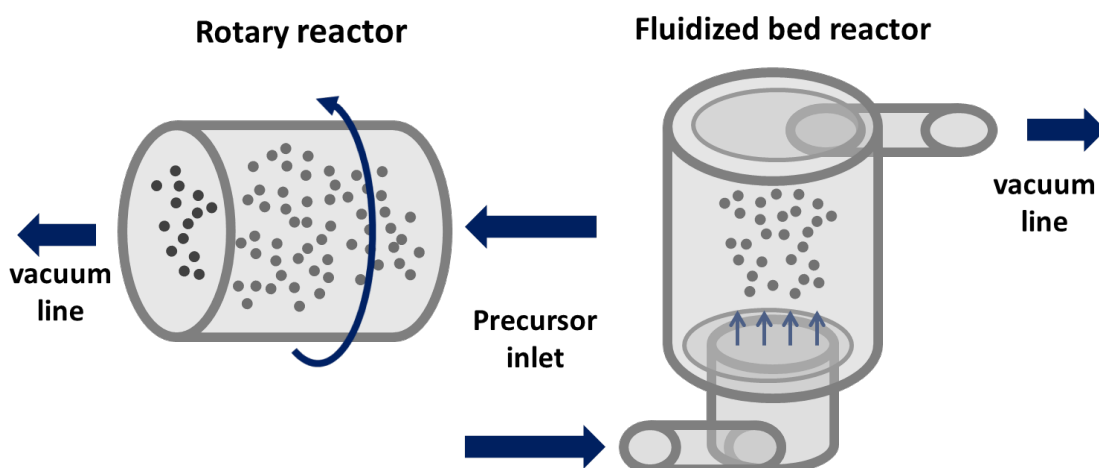


**Figure 4.5:** Basic schemes of the two particle reactor designs. The fluidized bed reactor on the right has the advantage of the higher weight capability and shorter pulse times, but with the disadvantages of higher investment costs, more complicated process parameters, and larger precursor consumption. The rotary reactor is easier and cheaper to build, but has a smaller loading capability.

the advantage of being able to cover large quantities of particles conformally, but on the other hand, a high amount of precursor is necessary (and wasted) and the particle size distribution has to be as small as possible to ensure homogeneously coated particles. It is more complicated in designing, building up, and running than the rotary reactor. Due to this facts, a fluidized bed reactor is not optimal for the use in scientific research fields, where typically small amounts of powder will be coated and possibly not commercially available precursor gases are used. For this reasons, the rotary reactor (see figure 4.5) is chosen to be the better option: In contrast to the fluidized

**1** inner chamber closing    **3** rotating inner chamber
**2** PTFE membrane    **4** non rotating outer chamber
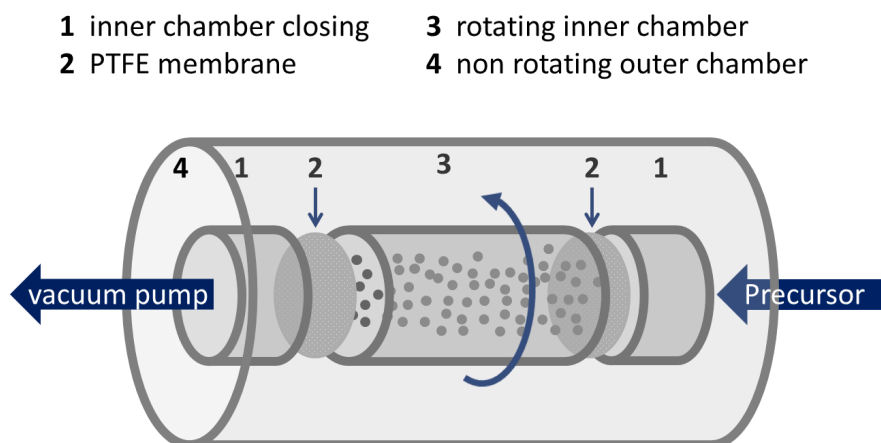


**Figure 4.6:** Scheme of the inner part of the reaction chamber, where the particles are kept in motion by the rotation of the inner chamber. The outer chamber is fixed to ensure gas fitting for the precursor flow.

bed principle, the rotary reactor has a different technique to ensure that the whole surface of every particles is accessible to the gas precursor. By rotation of the reaction chamber, the enclosed particles are constantly in motion and the complete surface can react with the precursor. The inner rotating-chamber is designed to keep two Polytetrafluorethylen[1] (PTFE) membranes on the each side, which are thermally stable up to around 250 °C. These prevent the particles from leaving the reaction chamber either in the waste line or in the precursor inlet (see figure 4.7). To make sure that the coating is homogeneous, the precursor is kept in the chamber for a specific time (exposure mode). The inner chamber is covered by a fixed outer chamber. This is necessary, since due to the rotation no gas line fittings can be connected to the chamber, the precursor and the waste line. One of the major challenges is the connection between the
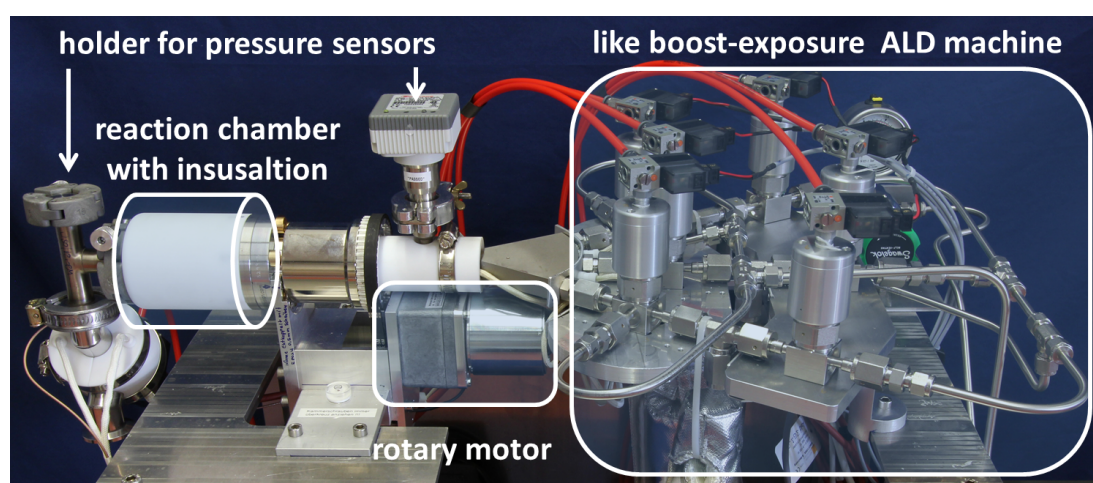


**Figure 4.7:** Picture of the rotary reactor without precursor bottles and the regulation electronics. The right part is similar to the boost modus ALD reactor (see figure 4.4. On the left side the vacuum rotation throughput, the rotation motor and the reaction chamber, covered with insulator material, is visible.

rotating part of the reactor (the inner chamber) and the gas flow line. Therefore, a gasket is needed which can resist the heating temperature, the material deposition and which is tight enough for the reaction pressure to be around $10^{-1} - 10^{-3}$ mbar. This is done by a magneto-fluid gasket which separates the moving from the non-moving parts. The whole outer chamber, including the gasket, a rotation fitting to connect the inner chamber and the motor to power the rotation is a commercially available setup (*VACOM - MagiDriveMD35H*), with a maximum working temperature of 200 °C (short time stability: 250 °C), a maximum drive of 230 rpm and UHV capability. The inner chamber is a self-made stainless steel container with two separators for the PTFE membrane holders (see figure 4.6). In the next step, we have to ensure that all parts

---

[1] Better known under under its trade name *Teflon*.

which are in contact with the precursor gases are as homogeneously heated as possible. All heat transfer has to be indirect because of the technical restrictions of heating the rotating parts. The outer chamber is heated by three 200 W heaters. Heat transfer to the inner chamber is guaranteed by the outer chamber heater and the connection to the gas line which is heated as well.

## 4.2 Growth of $Sb_2Te_3$ by ALD

Pore *et al.* were the first who reported the ALD growth of metal-tellurides and -selenides, including the process used in this work for $Sb_2Te_3$, with the motivation to produce $Ge_2Sb_2Te_3$ (GST) for phase-change random-access memory devices [25]. They invented a new kind of alkylsilyl compounds $(Et/Me_3Si)_2Te/Se$ (inspired by precursor chemistry used in MOCVD[2] processes see e.g. [60]), which should react sufficiently with metal-chloride precursors to solid and stable metal-telluride/selenides. For safety reasons (tellurium and selenium are highly toxic) and due to handling the alkylsilyl compound, $(Et_3Si)_2Te/Se$ was chosen for depositions, because the precursor is liquid at room temperature and seems to be thermally stable enough to not self-decompose [25]. In combination with the good reactivity with the commercially available $SbCl_3$ (solid at RT) it is probably the most promising candidate to create high purity $Sb_2Te_3$ thin films.

The reaction mechanism have been studied in a second publication by in-situ monitoring the mass spectrometry during the ALD pulses [92]. The basic reaction is as following:

$$2SbCl_3(g) + 3(Et_3Si)_2Te(g) \rightarrow Sb_2Te_3(s) + 6Et_3SiCl(g) \qquad (4.1)$$
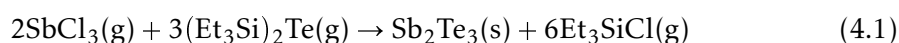
Different types of substrates and nanostructures have been coated with $Sb_2Te_3$. Table 4.2 gives an overview of the templates analysed with SEM. Several more have been tested (e.g. CdSe, $BaF_2$,...) with either very similar results to those listed or without deposition. The major problem of $Sb_2Te_3$ deposition with the self-made reactors

| material | flat substrates | nanowires (diameter) | particles (diameter) |
|---|---|---|---|
| $Si/SiO_2$ | 500 µm/300 nm $SiO_2$ | - | - |
| GaSb | 500 µm/native Oxide | - | - |
| GaAs | 500 µm/native Oxide | MBE (∅ about 50 nm) | - |
| $Bi_2Te_3$ | - | VLS (∅ about 200 nm) | mortar (~1 µm) |

**Table 4.2:** Overview of used materials and structures as templates for the atomic layer deposition of $Sb_2Te_3$.

---

[2]MOCVD: metal organic chemical vapour deposition

arises from the low precursor vapour pressure of the $(Et_3Si)_2Te/Se$ precursor and the decreasing growth rate with increasing temperature of this special process [25]. Unlike the inventors of this process (Pore *et al.* ), we found a minimum deposition temperature of 80 °C and a growth rate of 0.16 Å/cycle with a high error due to the surface roughness, while they report to have a growth rate of 0.6 Å/cycle at 60 °C [25]. For a detailed overview of the deposition parameters and the growth rate see figure 4.8 (a) and table 4.3. The parameters for the deposition cycles have been optimized to get



(a)                                  (b)
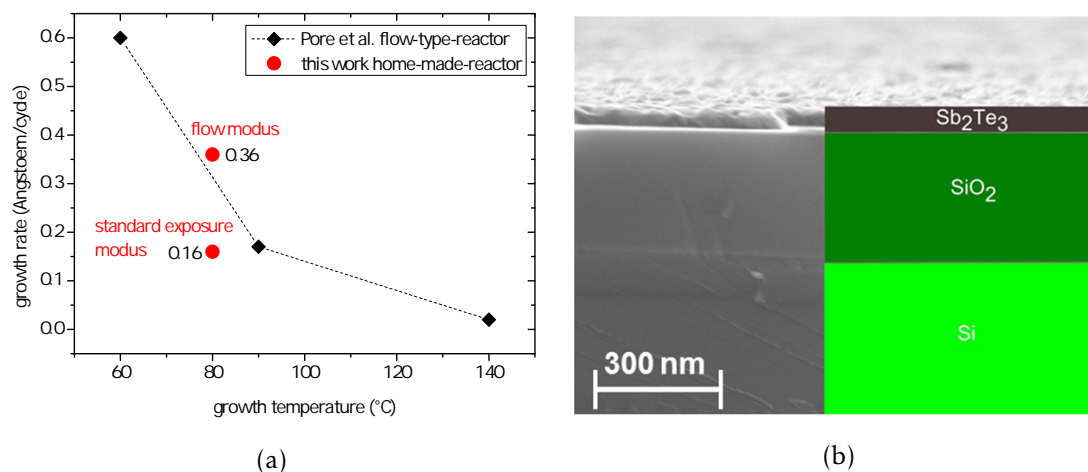
**Figure 4.8:** (a) Comparison of the literature growth rate, with the rate found in this work. (b) ALD Sb$_2$Te$_3$ thin film grown on top of a Si/SiO$_2$ wafer.

smooth films and an acceptable growth rate on Si/SiO$_2$ substrates. The chosen growth parameters can be found in table 4.4 labeled as "standard". The parameters are in good agreement with the optimized values found by Gu *et al.* [64]. A more detailed look on the growth behaviour of Sb$_2$Te$_3$ for different substrates and under variation of the growth parameters will be given in the following sections.

| parameters | Pore et al. [25] | this work |
|---|---|---|
| $T_{SbCl_3}$ | 30 °C | 55 °C |
| $T_{(Et_3Si)_2Te}$ | 40 °C | 77 °C |
| $T_{growth}$ | 60 °C | 80 °C |
| ALD modus | flow | exposure |
| growth rate | 0.6 Å/cycle | 0.16 Å/cycle |

**Table 4.3:** Growth parameter comparison.

To study the morphology of the Sb$_2$Te$_3$ ALD growth, thin film depositions on flat wafers have been made. As substrate a high resistivity phosphor doped Si <100> wafer of 500 μm thickness with 300 nm of thermal evaporated SiO$_2$ was used. De-

positions on substrates with lattice constants close to Sb$_2$Te$_3$, like e.g. GaAs, BaF or GaSb, have shown similar growth behaviour (see figure 9.5 in appendix). Figure 4.9 shows the surface after the deposition of three different numbers of ALD cycles ($x$). The upper third of the figure shows a Scanning Electron Microscope (SEM) images
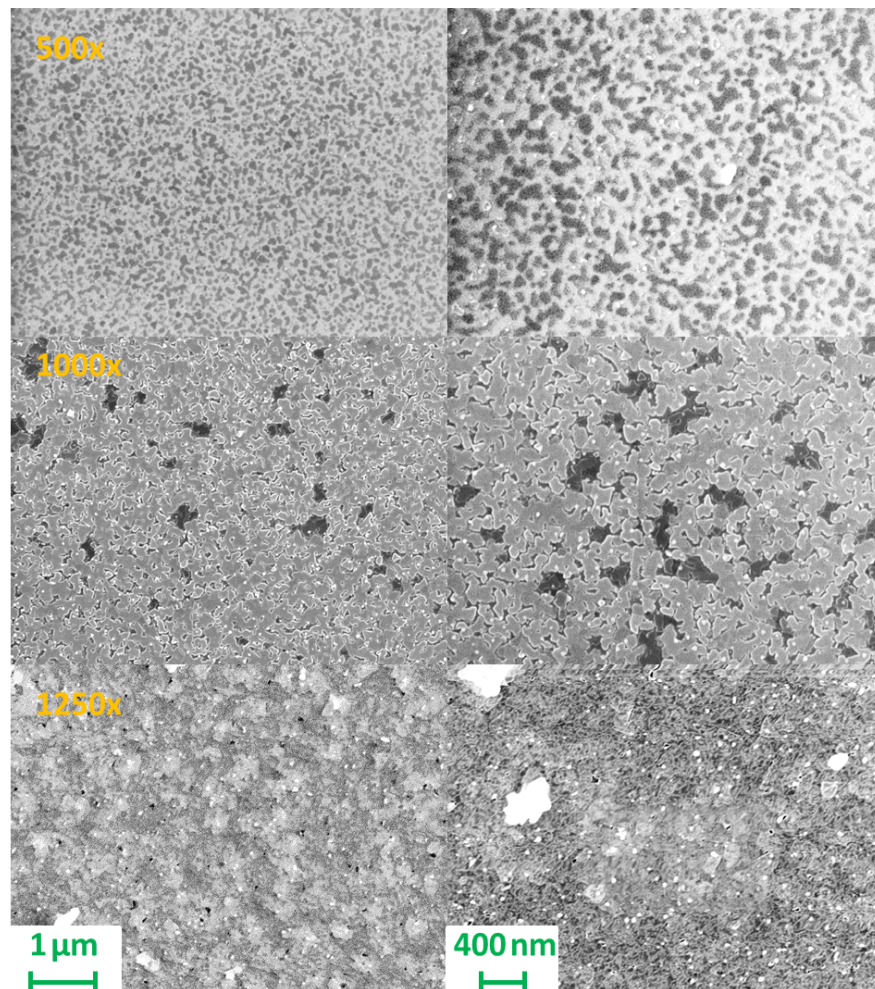


**Figure 4.9:** Growth of Sb$_2$Te$_3$ on Si/SiO$_2$ substrates at two different magnifications. The number of ALD cycles is labelled.

of 500 ALD cycles of Sb$_2$Te$_3$ in two different magnifications. In accordance to resistance measurements, where only an infinite resistance could be measured, no closed film was observed at this cycle number. Increasing the number of cycles, the films get denser. In contrast to the SEM pictures, which seem to show closed films, no electrical measurements were possible below 2000 ALD cycles. The pictures in figure 4.9 are representative for the Sb$_2$Te$_3$ growth behaviour. The non-closed film, observable below 2000 ALD cycles indicate a different growth mechanism in contrast to the the "classical" layer-by-layer growth. In contrast to ALD processes like Al$_2$O$_3$ or SiO$_2$,

which show growth rates in the range of 0.1-0.2 nm per cycle, Sb$_2$Te$_3$ has an order of magnitude lower deposition rate (see figure 4.8 and [25]). The strongly decreasing deposition rate with increasing substrate temperature indicates that adsorption and desorption of the precursor material are competitive processes during [93]. Addition- ally, Gu *et al.* reported a massive material loss due to desorption (see figure 4.10)[3], if the substrate temperature is increased up to 180°C and identify an optimal ALD temperature window of 60 − 70 °C [63] for creating relative smooth and polycrys- talline Sb$_2$Te$_3$ films. Pore *et al.* found the minimum deposition temperature to be 60 °C, but have used a flow type reactor instead of an exposure-mode-reactor used in this work [25, 63]. This is why the reactor (and therefore the substrate) temperature was chosen to be as low as possible, limited only by the low vapour pressure of the (Et$_3$Si)$_2$Te precursor. As lower limit, 80 °C as reactor- and 77 °C (Et$_3$Si)$_2$Te precursor- bottle temperature were used in the used home-made boost-exposure-reactor. The
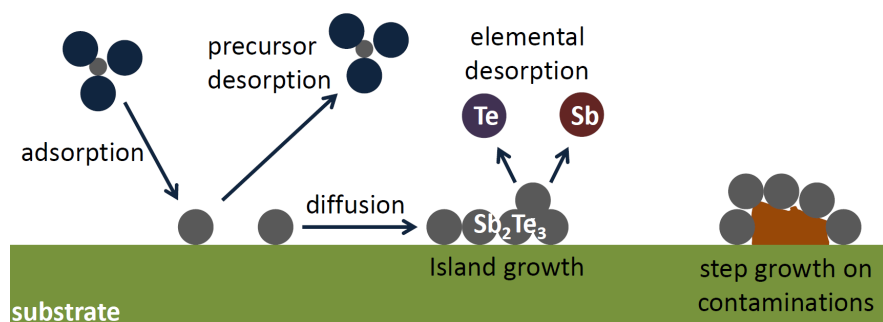


**Figure 4.10:** Scheme of the growth of Sb$_2$Te$_3$ showing the competitive mechanisms of absorp- tion and desorption.

dominant growth mechanism can be identified as Volmer-Weber island growth. The system tries to minimize the surface and interface energy, forcing the surface atom diffusion [94]. As result, the deposition starts at nucleation points (for example on surface contaminations, defects or edges of the substrate), subsequently larger islands are formed resulting in a polycrystalline film. This mechanism is typical for Sb$_2$Te$_3$ thin film growth. As a consequence of the weak van der Waals coupling of the quintu- ple layer and to the substrate, the Sb$_2$Te$_3$ thin film achieve his lattice parameter from the beginning of the growth [95]. Similar results to the ALD growth mechanism in this work can be found in literature with several other deposition techniques on many kinds of substrate materials (e.g. MBE, CVD, co-evaporation,...) [56, 58–64, 95, 96].

---

[3]using the slightly different tellurium-precursor: (Me$_3$Si)$_2$Te

### 4.2.1 Structural and compositional analysis

Beside the morphology analysis, the structural and compositional analysis has been performed. By X-ray diffraction (XRD) measurements information about the crystal structure can be obtained. Figure 4.11 shows the XRD pattern of a 50 nm Sb$_2$Te$_3$ film and the corresponding clean Si/SiO$_2$ substrate measurement. Nearly all peaks can
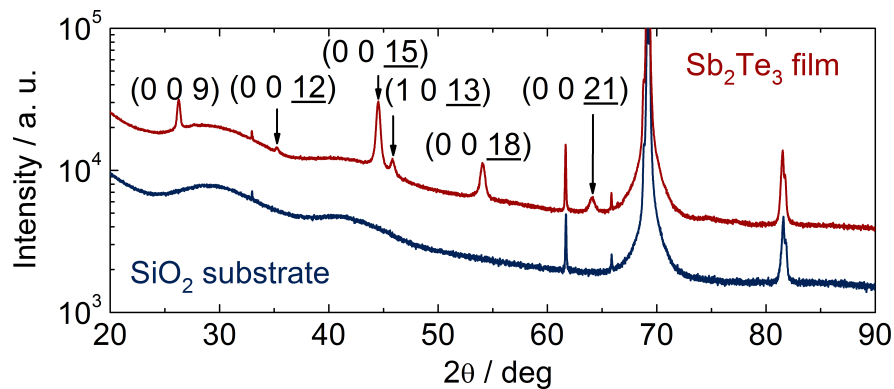


**Figure 4.11:** XRD-pattern of a 50 nm Sb$_2$Te$_3$ and of the Si/SiO$_2$ substrate. Reprinted with permission [97].

be identified as peaks of the $(00n)$-direction, which is corresponding to the c-axis of the hexagonal cell of Sb$_2$Te$_3$ (see figure 4.11). So the major growth direction is along the c-axis, as it is expected from the alternated pulsing of the Sb and Te-precursor in combination with the layered structure of Sb$_2$Te$_3$ due to the weak van der Waals bonds between the quintuple layers (see figure 2.3 (b)) [95]. The additional (10$\underline{1}$3) peak belongs to plates growing perpendicular to the c-axis which can be found in the SEM pictures (see figure 4.9). Such spontaneous generation of free-standing plates are found to be driven strain effects if the lattice mismatch between thin film and substrate is large [56].

Additional energy dispersive X-ray spectroscopy (EDX) measurements on several films and at different positions in average show a concentration of 39.96 at% and 60.04 at% (see table 9.1 in the appendix) of Sb and Te respectively, which is very close to the 2:3 Sb/Te ratio expected from the XRD analysis. To confirm the stoichiometric ratio, PIXE (particle induced X-Ray emission)-measurements have been performed by using a 3.5 MeV H$^+$ beam[4]. In the analysed area (1 $\times$ 1 mm) a Te/Sb ratio of 1.49 $\pm$ 0.03 was found which matches - within the error - the ideal stoichiometry. This fact re-emphasises the major advantages of ALD growth in reference to the material quality of Sb$_2$Te$_3$ thin films: the chemical growth mechanisms and the low deposition

---

[4]Thanks to Dr. Frans Munnik from Helmholtz Zentrum Dresden Rossendorf (HZDR), who performed the measurements.

temperature.

## 4.2.2 Structural analysis of $Sb_2Te_3$ thin films under different growth conditions

To determine the growth behaviour in more detail, additional experiments under different ALD-conditions have been made. Since the $Sb_2Te_3$ growth is a function of absorption and desorption of the precursor ligand as well as the desorption of the contributed elements, the temperature has been chosen to be fixed to the lower limit of 80 °C to minimize the energy for the desorption process. Nevertheless, the valve open time parameter can be varied. Since $Sb_2Te_3$ and/or the elements show a strong tendency to surface diffusion, highlighted by the island growth (see figure 4.9 and figure 4.10), variations of the exposure and pump times should have an effect on the film growth [64]. Therefore, a structural analysis has been performed by keeping the number of ALD cycles constant and continuously reducing these times controlled by the specific valve times (see table 4.4). As a lower limit, a flow-type reactor behaviour has been emulated by constantly evacuating the reaction-chamber without any exposure time (flow modus). The different parameters can be found in table 4.4. For

| name | open (1 and 2) (s) | exposure (s) | pump (s) | $T_{ch}$ | $T_{Te}$ | $T_{Sb}$ |
|---|---|---|---|---|---|---|
| standard | 2 | 20 | 25 | 80 °C | 77 °C | 55 °C |
| 25/40 | 2 | 40 | 25 | " | " | " |
| 10/15 | 2 | 15 | 10 | " | " | " |
| 10/7 | 2 | 7 | 10 | " | " | " |
| 10/2 | 2 | 2 | 10 | " | " | " |
| flow mode | 2 | - | 10 | " | " | " |

**Table 4.4:** Growth parameters (valve times) and temperatures for the depositions under different growth conditions but with a constant number of 2000 ALD cycles. The flow-mode has been emulated by externally keeping the pump-valve open.

the evaluation of the thickness and the surface roughness, Atomic force microscopy (AFM) measurements have been performed on the lithography design Hall-bar structures. Indeed, the growth rate of the thin film changes slightly with the pulse time, but there is a big difference for the flow mode. Figure 4.12 (a) shows the layer thickness in respect to the pump/exposure time. The thickness of the film grown under flow conditions is nearly twice as high as depositions with exposure times. Because of the missing exposure time, the desorption is suppressed, resulting in a higher film thickness. The surface roughness can be determined by AFM (see figure 4.13), is shown in figure 4.12 (b). A constant reduction with respect to the pump/exposure times underlines the effect of diffusion and the Volmer-Weber growth behaviour. By increasing the
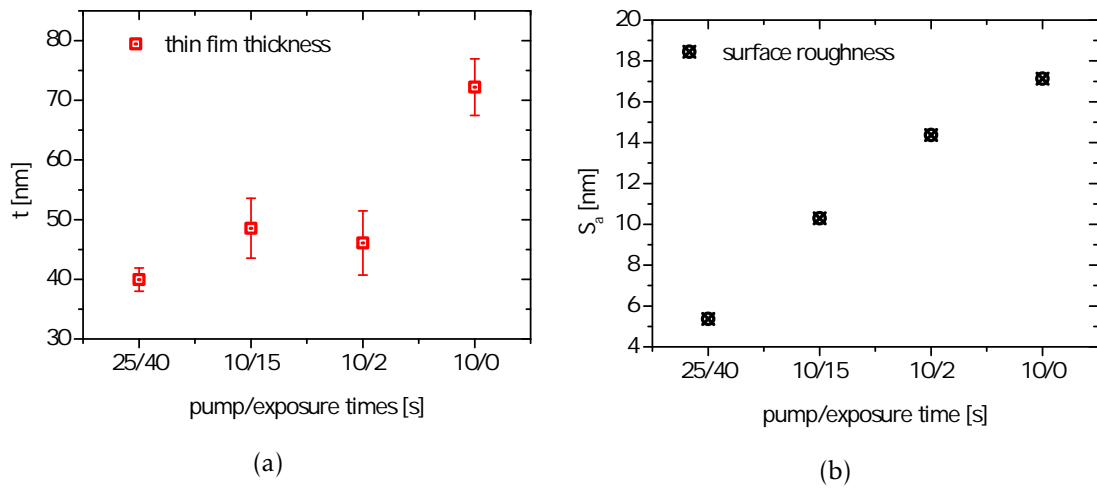
**Figure 4.12:** Figure (a) shows the film thickness of the samples with different growth parameters. All samples have been produced with $2000\,x$ ALD cycles. In figure (b) the surface roughness is shown as a function of the pump/exposure time, showing a clear trend to higher roughness with lower exposure and pump times.

time in which the $Sb_2Te_3$ system can rearrange itself, the growth parallel to the surface and therefore perpendicular to the c-axis is more pronounced, resulting in larger plane islands. This fact can also be seen in the XRD data. Using the Full Width at Half Maxima (FWHM) $\Delta\theta$ of the X-ray peaks, the grain size perpendicular to the layer axis of the thin films can be calculated by using the Sherer-equation (see figure 4.14) [98]:

$$D_{hkl} = \frac{K\lambda}{\Delta\theta_{hkl}\cos\theta},$$ 

(4.2)

where $D_{hkl}$ is the crystalline size, hkl are the Miller indices of the analysed lattice planes, $\lambda$ is the used X-ray wavelength, $\Delta\theta_{hkl}$ is the FWHM of the corresponding peak, $\theta$ is the Bragg angle and $K$ crystalline-shape factor [99]. In absence of detailed shape information, $K = 0.9$ is a reasonable approximation [99, 100].

## 4.3  Growth of $Al_2O_3$ by ALD

The trimethylaluminium(TMA)/water (AlMe$_3$/H$_2$O) process to produce $Al_2O_3$ thin films is one of the most intensively studied ALD-processes [20]. The well understood growth behaviour/mechanism from the first surface reaction and the wide resistances against temperature, pulse time and atmosphere pressure changes as well as being highly reactive with oxygen/moisture if the machine is not leakage free, makes it a perfect proof of principle process [20]. Therefore, the $Al_2O_3$ deposition was the first process running on the new developed particle reactor checking the general function-

(a)



(b)
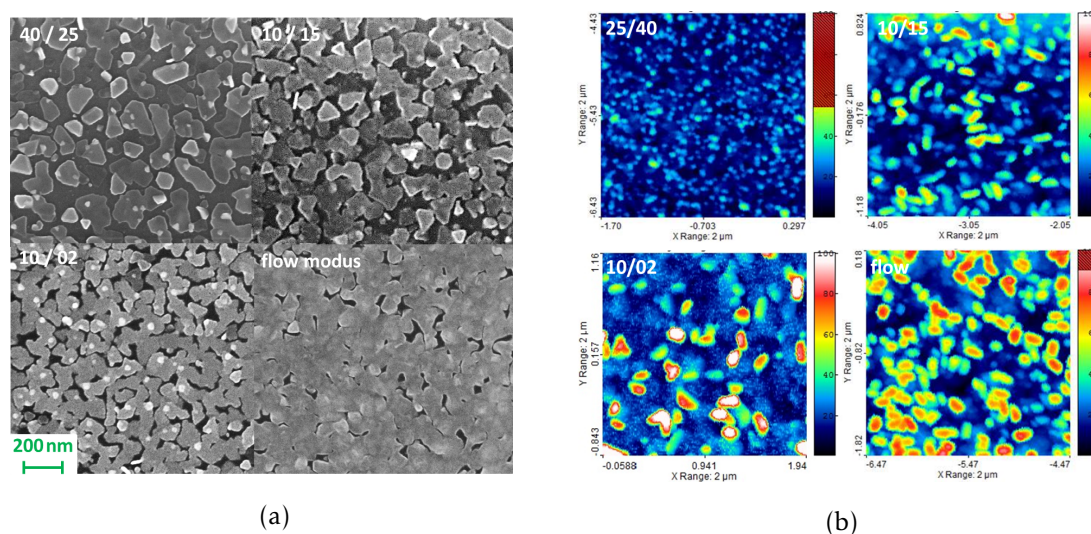
**Figure 4.13:** Figure (a) shows the SEM images of the surface of the thin films grown with different pump/exposure times. In figure (b) the AFM images of the respective films are shown. Clearly visible the increasing surface roughness with decreasing pump/exposure times. All films have been grown with 2000 x ALD cycles.



(a)



(b)
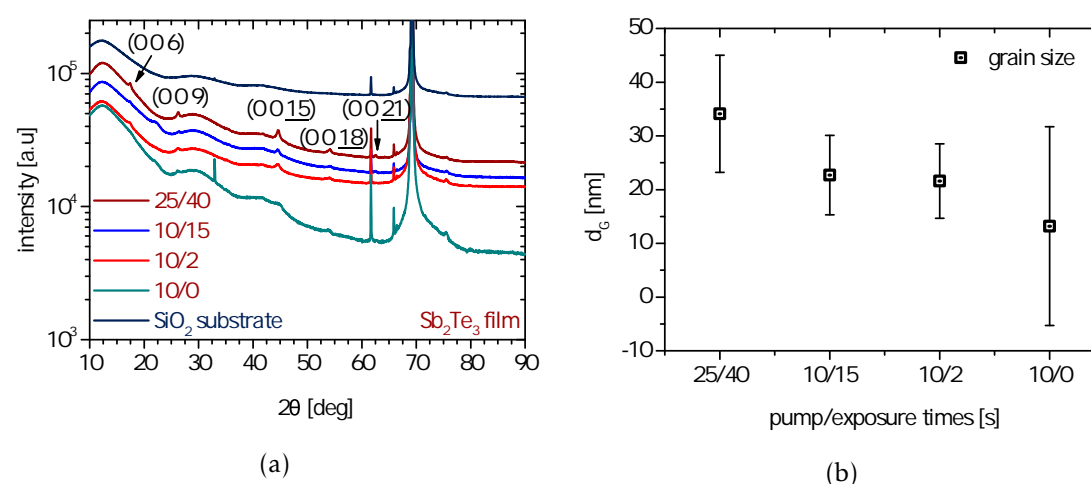
**Figure 4.14:** Figure (a): XRD pattern of the ALD Sb$_2$Te$_3$ thin films with pulse time variation. Figure (b): The grain size calculated with equation as a function of pulse time.

ality of the machine. First, the growth rate on flat Si/SiO$_2$ substrates is determined by measuring the film thickness by ellipsometry of different TMA+H$_2$O cycle numbers at a growth temperature of 120 °C (see figure 4.15). Both precursor bottles are keep at room temperature with precursor pulse times of 0.2 s and 2 s for TMA and H$_2$O respectively. The growth rate is evaluated with a linear fit to the measured value and is calculated to be 1.49Å/cycle which is in good agreement with results previously published by Puurunen et al. [20].

Atomic Layer Deposition
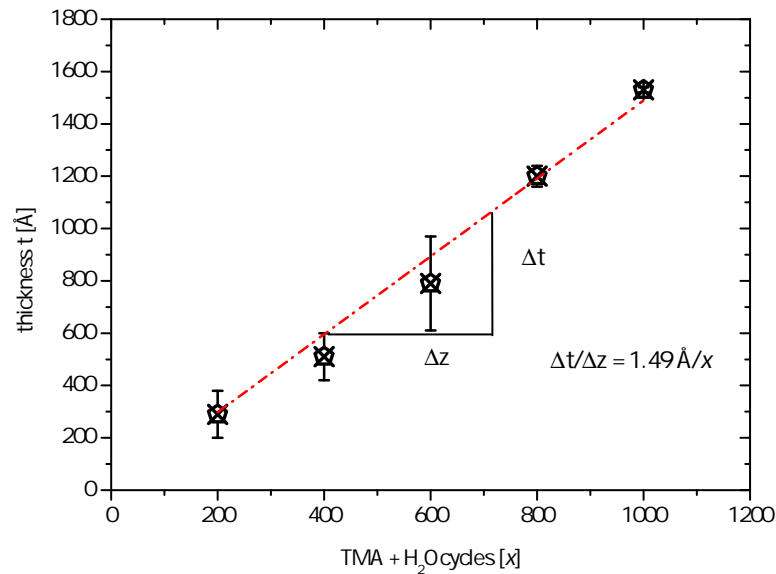
**Figure 4.15:** $Al_2O_3$ thin film thickness against ALD cycles. The growth rate is determined by the linear regression between the measurement points and is evaluated to be 1.49 Å per cycle.

## 4.4 ALD growth of $Sb_2Te_3$ and $Al_2O_3$ on nanowires/ribbons and particles: core shell structures

$Sb_2Te_3$ films have been grown on different nano- and mesostructures to show the applicability of the conformal ALD coating. In this section we present selected examples of core shell structures. The left side in figure 4.16 (a) shows SEM-pictures of uncoated VLS grown GaAs wires with a diameter of approximately 50 nm. In the upper part of the picture the GaAs substrate, the on-grown wires and some randomly orientated humps can bee seen. The right side pictures correspond to 2000 ALD cycles of $Sb_2Te_3$ deposited on this GaAs structures. Hexagonal plates of $Sb_2Te_3$ on top of the (crystalline) edges of the GaAs surface highlight the anisotropic growth behaviour of the material. Due to this plates, the $Sb_2Te_3$ shell of GaAs wires varies in thickness and cannot assumed to be homogeneous. In figure 4.16 (b) the core shell structure of VLS grown $Bi_2Te_3$ nanowires/ribbons[5] are shown. As well as in the case of GaAs, one can find hexagonal plates on the surface of this structures, but the TEM image (shown in the inset) indicates a more homogeneous growth of $Sb_2Te_3$ on $Bi_2Te_3$ nanostructures. Further HRTEM investigations show a nearly single crystalline shell. However, this single crystallinity is expected because of the almost matching lattice spacings of both materials (see table 2.1). The island growth behaviour seen on flat substrates is not

---

[5]Grown by Bacel Hamdou, see i.e. [80]

---

## 4.4. ALD growth of $Sb_2Te_3$ and $Al_2O_3$ on nanowires/ribbons and particles: core shell structures



(a)            (b)
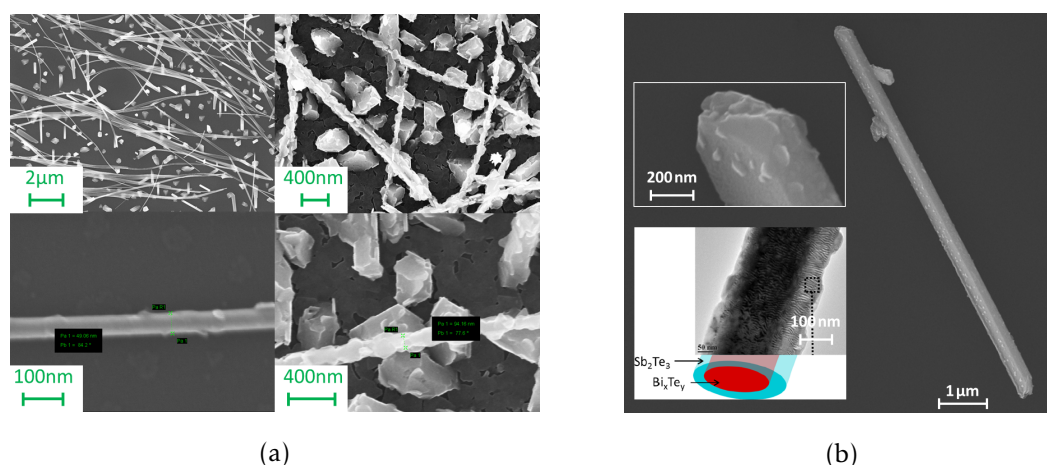
**Figure 4.16:** Figure (a) left side: Uncoated VLS grown GaAs wires on GaAs substrate. Figure (a) right side: GaAs wires with 2000 cycles of $Sb_2Te_3$ showing hexagonal plate structure. Figure (b): SEM and TEM (smaller inset) pictures $Sb_2Te_3$ coated VLS grown $Bi_2Te_3$ nanowires/ribbons, showing a more homogeneously distributed shell, as expected by the small lattice mismatch of both materials.

completely suppressed. The results presented so far have been produced using the Boost- and exposure-mode conventional ALD-reactor with the "standard" growth parameters (see table 4.4). Particle coatings for different numbers of $Sb_2Te_3$ and $Al_2O_3$ cycles have been performed with the use of the particle reactor. In the case $Bi/Sb_2Te_3$-core shell particles it is challenging to distinguish between both compounds with e.g. TEM or EDX, because density and the lattice parameter are very similar. However, the SEM pictures of surface of the $Bi_2Te_3$ particles with a shell corresponding to 0-2000 ALD cycles of $Sb_2Te_3$ presented in figure 4.17 show closer films with increasing number of ALD cycles. The growth rate is possibly higher compared to growth on $Si/SiO_2$,
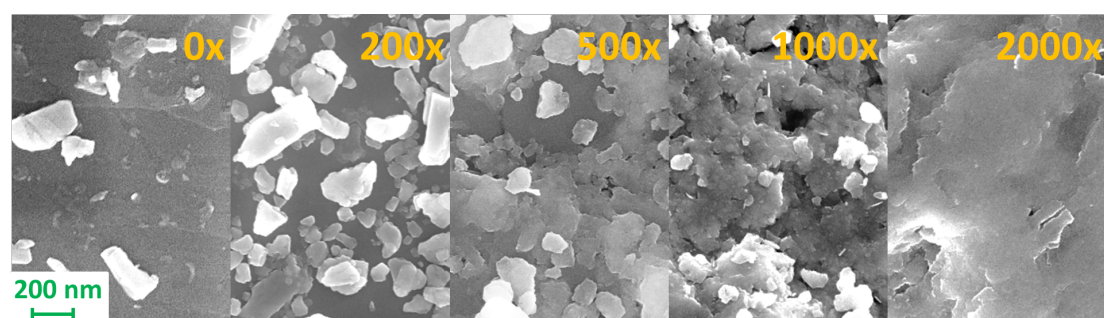


**Figure 4.17:** $Bi_2Te_3$ particles coated with different numbers of $Sb_2Te_3$ ALD cycles.

because the high similarity of both compounds should increase the surface bonding leading to a suppressed desorption. In figure 4.18 we present TEM images[6] of as cast

---

[6]TEM images by Kristina Pitzschel, Humboldt-Universität zu Berlin

and ALD coated Bi$_2$Te$_3$ particles. This core-shell structures have been produced by the particle reactor with 200 cycles of TMA and H$_2$O at 120 °C. In comparison to the uncoated Bi$_2$Te$_3$ particles (smaller inset - double magnification), a less dense film on the surface can bee seen. This shell corresponds to the Al$_2$O$_3$ ALD layer. If we com-
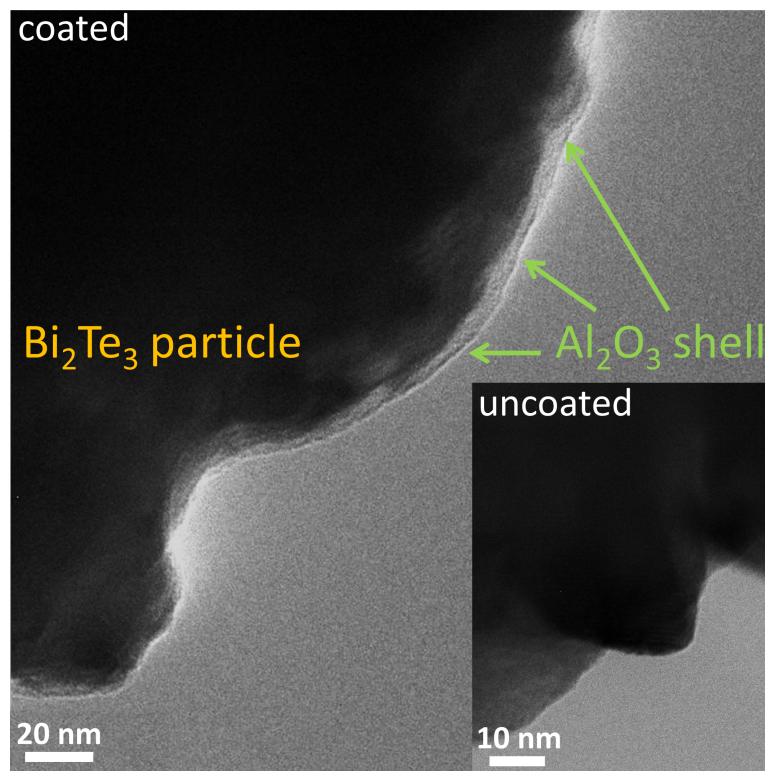


**Figure 4.18:** Large TEM image: Bi$_2$Te$_3$ particles coated with 200 cycles of Al$_2$O$_3$. For comparison the inset shown a TEM picture of an uncoated Bi$_2$Te$_3$. Note: The magnification of the smaller picture is 2 times higher.

pare the results with the deposition of Al$_2$O$_3$ on flat Si/SiO$_2$ substrates using the same precursors with a growth rate of 1.49 Å/cycle (30 nm in the case of 200 cycles), we can find a thinner thickness of about 10 nm on the particles. Two mechanisms are responsible for the suppressed deposition rate: (1): Obviously the rotary reactor design cumbers the growth: Although the constant rotation of the reactor ensures that every part of the surface is accessible to the precursor gas, this accessibility is not valid at every time. When the particles stick together in the case of agglomeration or if they are in touch with the inner reactor surface because of the different centripetal force of each individual particle weight (size), some part of the surface is caped for the precursor gas, leading to a lower deposition rate. This disadvantage maybe decreased by reducing the particle size distribution and by choosing longer exposure times; (2): The starting growth reaction of the Al$_2$O$_3$ on Bi$_2$Te$_3$ is unknown (for example missing OH-

groups at the particle surface), which could lead to a non-linear growth behaviour in the beginning of the $Al_2O_3$ ALD coating. Later, when the complete particle is coated, a linear growth rate is expected. Similar behaviour is known for the deposition of metals on oxide, e.g. Pt on oxide substrates, or vice versa - oxide on metals [101].

# Chapter 5

# Thin film device - preparation and functionality

In contrast to other thin film material casting methods, ALD has the advantage of a comparably low growth temperature (see figure 4.2). This enables the use of photolithography processes prior to the deposition, which gives a great benefit for designing a accurate measurement device. The basic idea, the manufacturing and the functionality of such a device (see figure 5.1) is presented in this chapter.
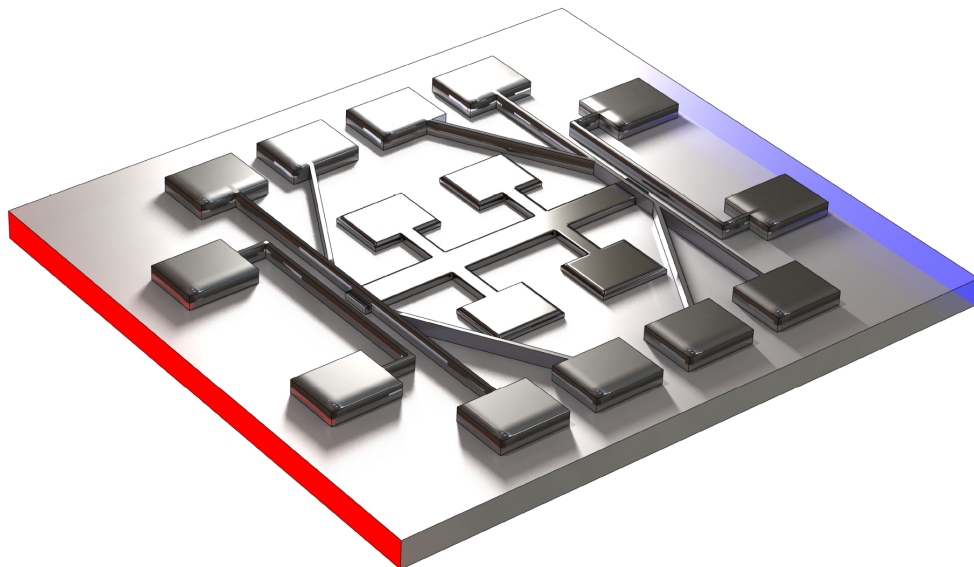


**Figure 5.1:** 3D view of the designed device (Figure drawn by Jens Heißenberg).

## 5.1 The measurement device

To characterise the thermoelectric, electronic and galvanomagnetic properties of the ALD $Sb_2Te_3$ thin films, a well defined device provides a great benefit in the accuracy and reproducibility of such measurements: First, because of the possibility of in-situ measurements of the electronic and thermoelectric transport coefficient at a single film to avoid errors in contrast of using different films for measuring of different properties; and second, the error of the device is probably similar, when comparing different films with each other.

The focus on the electronic thermoelectric properties means measuring: The Seebeck coefficient $S$, the electrical conductivity $\sigma$ and the galvanomagnetic properties: the Hall- and Nernst coefficient, $R_H$ and $N$. Therefore we must be able to: Measure voltage drops in two dimensions (x- and y-direction), measure the temperatures at the points of the DC voltage contacts, apply different temperature gradients and a current across the film (x-direction) and apply different magnetic fields perpendicular to the film plane (z-direction). The control and measurement of the device temperature as well as the AC resistance measurements are performed by the PPMS[1] measurement systems (see figure 5.6). Therefore the geometrical and contact boundary conditions of the device are limited to those of the chip carrier (called: *puck*):

- The overall device has to fit the geometrical conditions of the puck: 8x10 mm.

- No more then 12 contacts are available, from which 2x4 can be used with the internal ETO option for low frequency AC-measurements.

- The contacts must be small compared to the thin film dimensions, but the contact-pads must be large enough to achieve the wire bonding between them and the gold pads on the puck.

- The currents are limited to 10 mA.

For all measured parameters, individual conditions have to be fulfilled. These are described in the second part of this chapter.

## 5.2 Device preparation

In the following section the 2-step lithography process for the device preparation is described. Starting with the $Si/SiO_2$ substrate cleaning, by putting the wafer pieces in an ultrasonic bath in the listed order: Acetone, Isopropanol and distilled water -

---

[1] Physical Properties Measurement System by *QuantumDesign*

2 minutes each. Followed by the pre-patterning step of the Hall bar via spin-coating the positive photoresist $maP-1205$ *(micro resist technology GmbH)* and writing the soft mark using a $PG101$ *(HeidelbergInstruments)* laser beam writer with a minimum resolution of $1\,\mu m$ (see figure 5.2 (a) and (b)). The last step of pre-patterning is the development of the soft mask, using $MAD-331$ *(micro resist technology GmbH)*. Now the substrate is prepared for the ALD and the respective number of cycles of $Sb_2Te_3$ is deposited (figure 5.2 (c)). After the lift-off of the developed structure in acetone, the
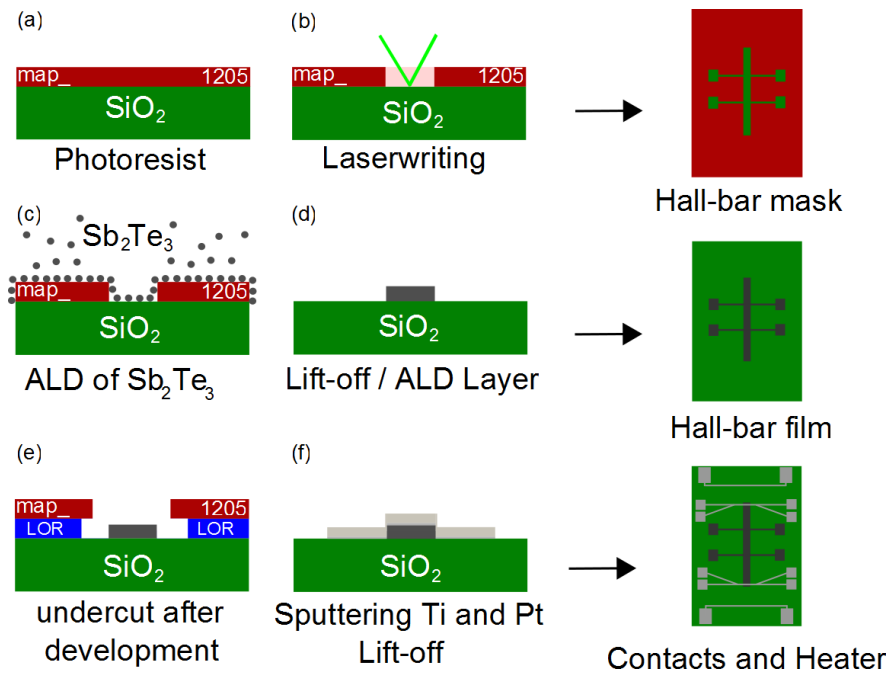


**Figure 5.2:** Flowchart of the two step photolithography process of transport characterisation device fabrication.

photoresist spin-coating step is repeated but now with two layers of photoresist. This is due to problems during the lift-off if only the $maP-1205$ is used as photoresist. Because the contact between photoresist and sputtered layer is too sticky, the contact material was inadvertently removed together with the non developed part of the photoresist during the lift-off. Using a lift-off resist ($LOR$) prior to the spin-on of the photoresist solved this problem. In contrast to the $maP-1205$ photoresist, which can only be removed at the exposed region, the $LOR$ layer is sensitive to the developer at any region which is accessible to the liquid developer. We get an so called "undercut" (see figure 5.2 (e)), meaning that a part of the $LOR$ is removed under the $maP-1205$, preventing a direct connection between the photoresist and the sputtered layer. Now the contact mask (figure 5.2 (e)) can be patterned. After the development (about 20 - 40 s) with $MAD-331$, a barrier layer of Ti (about 20 nm) is sputtered prior to the contact material deposition. This prevents diffusion from the Pt layer (about 80 nm)

into the $Sb_2Te_3$ thin film, which is sputtered on top as contact material. After the lift-off with the remover 1165 (*micro resist technology GmbH*) in a warming cupboard for about 12 h, the device is ready for measurements (figure 5.2 (f)).

## 5.3    Device function and properties - resistance measurements

Now with the $Sb_2Te_3$ layer structured and the contact mask sputtered on top, the device is ready for transport measurements. In a first step the functionality in terms of transport measurements is proven. We start with the most important measurement - the resistance of the thin film. In figure 5.3 a SEM-picture of the device with all necessary contacts named is shown. For the 4-point electrical conductivity measurement, a current $I_{sigma}$ between the contacts **I** an **II** (x-direction) is applied, while measuring the voltage drop $\Delta V_{sigma}$ between the contacts **B** and **D**. Using this geometry the measured resistance is independent of any contact resistances. In the case of ohmic contacts, a linear IV-curve is measurable which can be found in figure 5.4 (a). Additionally, if a magnetic filed $B$ is applied perpendicular to the current flow and
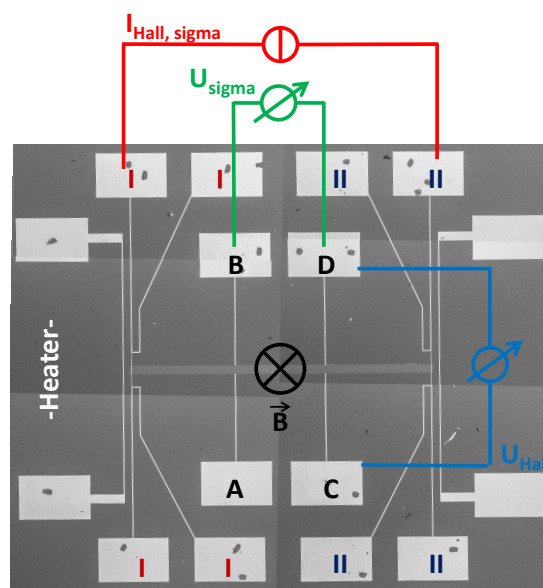


**Figure 5.3:** Combined SEM image of a complete device. The measurement contacts used are highlighted as numbers and letters. The current is applied between between **I** and **II** while the voltage is measured between **B** and **D** for the conductivity measurements and between **D** and **C** for the Hall measurements. The magnetic field is applied perpendicular to the thin film surface and the current flow.

the voltage contacts, the longitudinal magneto resistance (LMR) can be measured as

well with using the same contacts. All measurements are performed with the build in *ElectricalTransportOption* (ETO)[2] of the PPMS-system (*Quatum Design*), either with the *Versalab* - working temperature range between 50-400 K and maximum magnetic fields of $\pm$ 3 T, or with the *Dynacool* - working temperature range between 2-400 K and maximum magnetic fields of $\pm$ 9 T. The ETO works as a constant current source, applying a maximal current $I$ of 10 mA and a maximum voltage $V$ of 10 V with discrete frequencies between 0.5 and 184 Hz and a maximum sampling rate of $2\,\mathrm{s}^{-1}$ [102]. For the conductivity measurements, a current of 10 µA with a frequency of 181.15 Hz is applied. The conductivity can be calculated with the measured resistance and the (fixed) geometry of the sample film, with

$$\sigma = \frac{1}{R_{\mathrm{film}}} \frac{d}{b \cdot t} \frac{1}{\Omega\mathrm{m}}$$

with

$$\frac{d}{b} = \frac{990 \cdot 10^{-6}}{99.8 \cdot 10^{-6}}\mathrm{m}^2$$

and with

$$t = 0.016 \cdot 10^{-9} \cdot x\,\mathrm{m}$$

$$\Rightarrow \sigma = \frac{1}{R_{\mathrm{film}}} \frac{10}{0.016 \cdot 10^{-9} \cdot x} \frac{1}{\Omega\mathrm{m}},$$
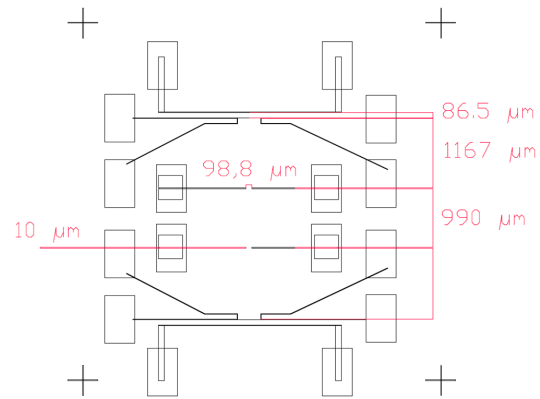


where $b$ is the width of the device and and $d$ is the length between the voltage contacts, giving a fixed factor for every device. $t$ is the thickness of the thin film, determined by the growth rate (0.016 nm) and the number of cycles $x$. Furthermore we have to ensure the resistance measurements work properly if a magnetic field is applied (in z-direction, meaning perpendicular to the film surface) - the Hall measurement. Therefore a current $I_{\mathrm{Hall}}$ between the contacts **I** and **II** is applied, while the voltage drop $V_{\mathrm{Hall}}$ perpendicular to the current and the magnetic field is measured between the contact **A** and **B** or **C** and **D** (see figure 5.3). The Hall resistance $R_{\mathrm{Hall}}$ is defined as the magnetic field dependent voltage drop: $R_{\mathrm{Hall}} = V_{\mathrm{Hall}}(B)/I_{\mathrm{Hall}}$. If the ordinary Hall effect is dominant, the measured resistance is linear proportional to the magnetic field. In figure 5.4 (b) such measurement of a 4500 cycle (72 nm) $Sb_2Te_3$ film is shown, with a clear linear behaviour of $R_{\mathrm{Hall}}(B)$.

---

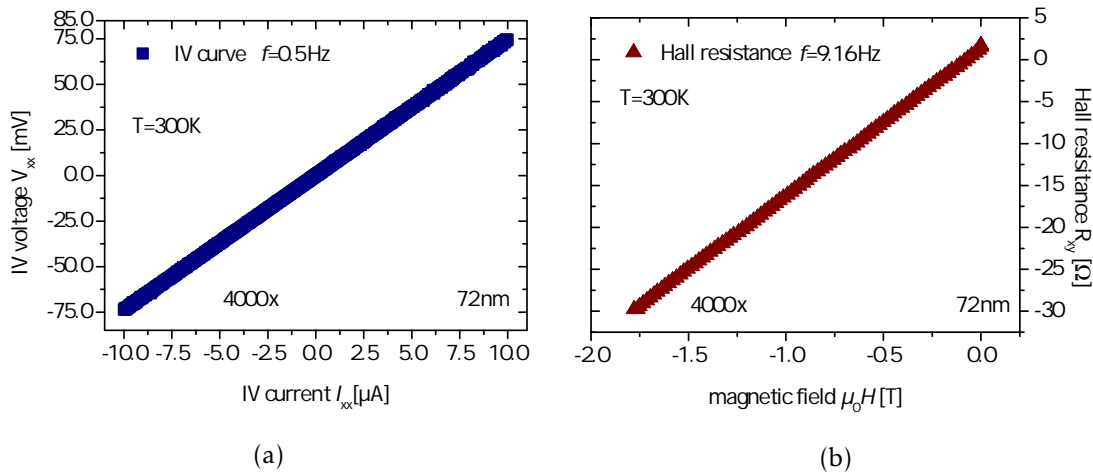[2]ElectricalTransportOption - 2-channel low frequency Lock-In amplifier

**Figure 5.4:** (a) Linear IV-curve of a 72 nm $Sb_2Te_3$ thin film. (b) Measured Hall resistance $R_{Hall}(B)$ of a 72 nm thin film in respect to the magnetic field. Both measurements have been performed at $T=300$ K.

## 5.4 Device function and properties - Seebeck measurements

Now that the functionality of the measurement platform for electrical and galvano-magnetic measurements is proven, we have to ensure that the device is able to measure all parameters for the calculation of the Seebeck coefficient $S$. Therefore it is necessary to precisely measure: first, the thermovoltage $V_{te}$; and second, the temperatures $T_{hot}$ and $T_{cold}$ at both contact points of $V_{te}$ in the case of an applied temperature gradient. A couple of parameters have to proven to ensure the device works properly. For the notation of the contacts see figure 5.5:

- The temperature and the thermovoltage measurement points have to be the same: This is defined by the structure (both are measured with the contacts **I** and/or **II**).

- No temperature drifts are allowed during both, the temperature- and the $V_{te}$-measurements, which means we have to be in a steady state regime: The programmed Seebeck routine written by Tim Böhnert, proven several times with Seebeck measurements of different nanostructures, includes such a stabilisation routine (see e.g. [97, 103–105]).

- The temperature gradient should be high enough to measure the small $V_{te}$ signals (typical in the range of nV to mV depending on the Seebeck coefficient of the material and the applied temperature gradient), but small enough to stay in the regime where the Seebeck coefficient is still linear in $T$: Depending on the material and the voltmeter used, gradients ΔT of 0.1 - 15 K between the thermo-
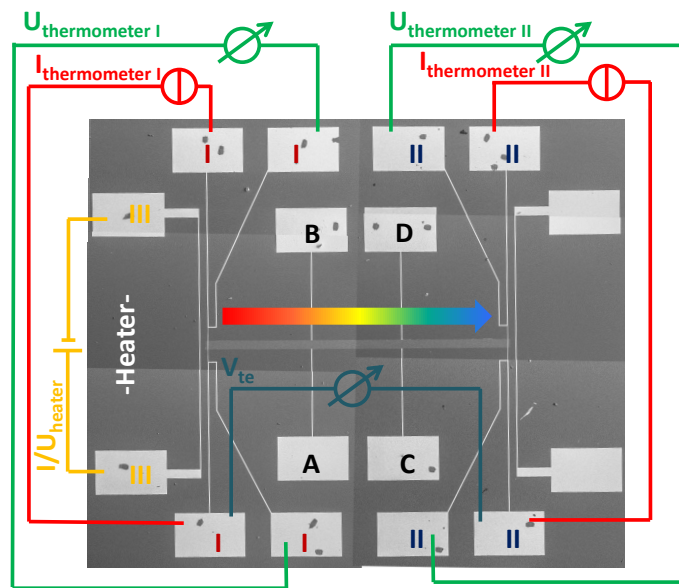
**Figure 5.5:** SEM image of the Seebeck measurement geometry. Contacts **III** correspond to the DC heater for applying a temperature gradient. The resistance of the thermometer **I** and **II** is measured with a Lock-in amplifier, while the DC thermovoltage is measured between contacts **I** and **II**.

voltage contacts are reasonable.

- Beside the precision of the voltmeter, the accuracy of the thermometers has to be high enough to properly resolve the applied temperature gradients, which often dominate the error of $S$. 4-point metal resistance thermometers are chosen to measure the temperature. They should be small enough not to act as local heat sinks (which would create a "local" temperature gradient around their position, influencing the Seebeck measurement) but with a good thermal contact to the film. The temperature dependence of the used platinum is almost linear in the measurement regime of 50-400 K. At all temperature steps, the 4-point resistance of these metal stripes are measured to evaluate the resistance versus temperature curve of the thermometers **I** and **II**. The resulting $T(R)$ curves are fitted by a second order polynomial, resulting in an effective resolution of the thermometers of better than 0.01 K.

- No crosstalk between the electrical measurement channels is allowed: While the thermovoltage is measured with an DC nanovoltmeter, the resistance of the thermometers are measured independently using the lock-in amplifier of the PPMS system with an AC current of 10 μA. The heater DC voltage applied is separated

by the high resistance Si/SiO$_2$ wafer.

A measurement program was written by Tim Böhnert to connect the internal control units of the PPMS systems and the necessary external DC devices for heating and thermovoltage measurements. This builds up the essential part for all Seebeck measurements performed. To get access to the internal measurement contacts, the splitbox connects the internal measurement channels with the DC nanovoltmeter and the DC current source (see figure 5.6), before the signal is sent back to the PPMS measurement system for the AC resistance measurements. During the measurement routine,
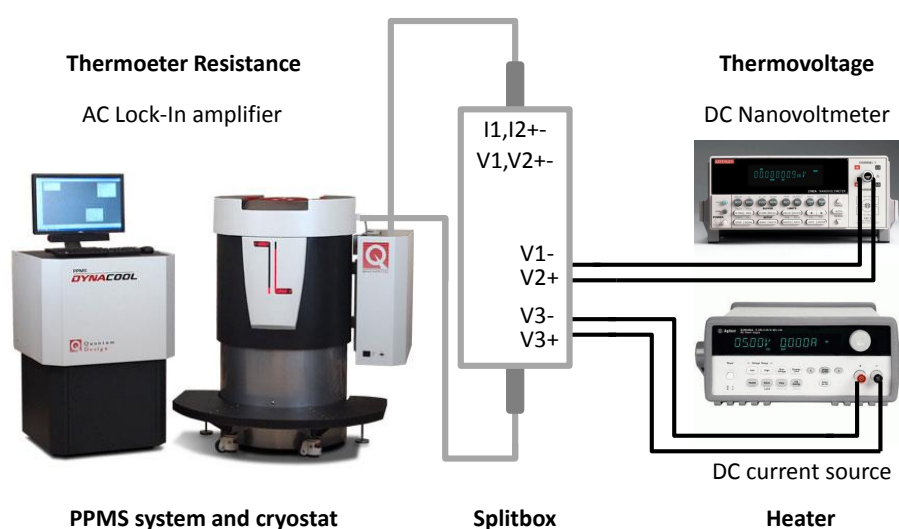


**Figure 5.6:** Scheme of the PPMS system with the included AC lock-in amplifier for the resistance measurements. The splitbox connects the system with the external DC voltmeter and current source for the thermovoltage $V_{te}$ measurement and heater power supply respectively.

the resistances of the two thermometers **I** and **II** (see figure 5.5) is measured with zero heating voltage to evaluate their temperature dependence (thermometer calibration). This has to be done for every measurement, since the resistance and temperature characteristics can differ a lot due to uncertainties during the metal contact sputter process (thickness, position in the chamber, contact resistance between the layer and the contacts etcetera). The temperature control unit of the PPMS systems needs a certain time to stabilise the cooling flow (and pressure) of the cryostat and the built in heater to

reach the specified temperature. Therefore it is necessary to program a delay time to avoid any temperature variations during the transient phase and allow device and sample to reach a thermal steady state.

Due to a relatively wide temperature regime (50-400 K), the temperature gradient differs during the measurement. The gradient is a function of the device heating performance and depends on three points:

- The heating power versus temperature: The induced heating power is proportional to the applied voltage $V_{heater}$ and the heater resistance $R_{heater}$, having the same temperature-resistance behaviour as the metal thermometer (see figure 5.8) since they are sputtered in the process. Therefore the resistance increases with increasing temperature, yielding in a higher output power of the heater ($P = I^2 R_{heater}$) with increasing temperature (see figure 5.7 (a)).

- The thermal resistance of the complete device (see figure 5.7 (b)): The thermal resistance $\gamma_d$ is a function of all thermal resistances parallel to the heating flow $J_x^{overall}$. This flow is assumed to be 1-D along the film (x-axis), because the heater width (y-axis) is much larger then the film width (see figure 5.5).

- The maximum current: Because the internal structure of the used PPMS systems is limited to the 10 mA, the current source is restricted to this value. The choice of the maximum voltage applied is therefore always a mixed calculation due to the change of heater resistance with temperature (see figure 5.7 (c)).



(a)  (b)  (c)
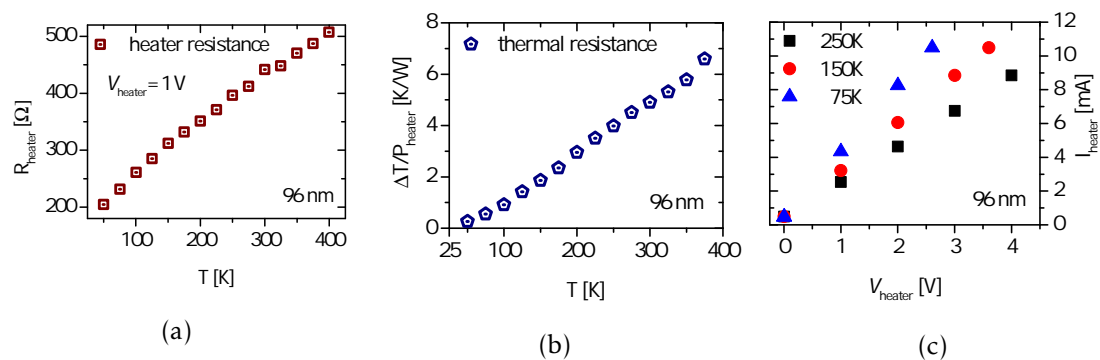
**Figure 5.7:** Heating characteristics of a 6000 cycle (96 nm) $Sb_2Te_3$ thin film device. (a) Heater resistance $R_{heater}$ versus temperature for $V_{heater} = 1$ V. (b) Device thermal resistance $\gamma_d$ versus temperature. The larger the thermal resistance, the larger the temperature gradient. (c) Heater voltage against heater current - reaching the 10 mA limitation with decreasing temperature.

For the evaluation of the temperatures ($T(R_{hot})$ and $T(R_{cold})$) at the voltage contacts, the resistance of both thermometers are measured at $V_{heater} = 0$. By approximating

the resistance versus the temperature curves, the temperature gradient can be calculated with applied heating voltages $V_{\text{heater}} \neq 0$ (see figure 5.8 (a)). The temperature gradient is proportional to the heater voltage, highlighting the direct correlation between the heating power and the gradient ($\Delta T = T(R_{\text{hot}}) - T(R_{\text{cold}}) \propto P$). If the heater current reaches the maximum of $10\,\text{mA}$, especially in the case of small $R_{\text{heater}}$ at low temperatures, the DC voltmeter limits the current (see figure 5.7 (c)).

The calculation of the Seebeck coefficient is determined by the thermovoltage divided
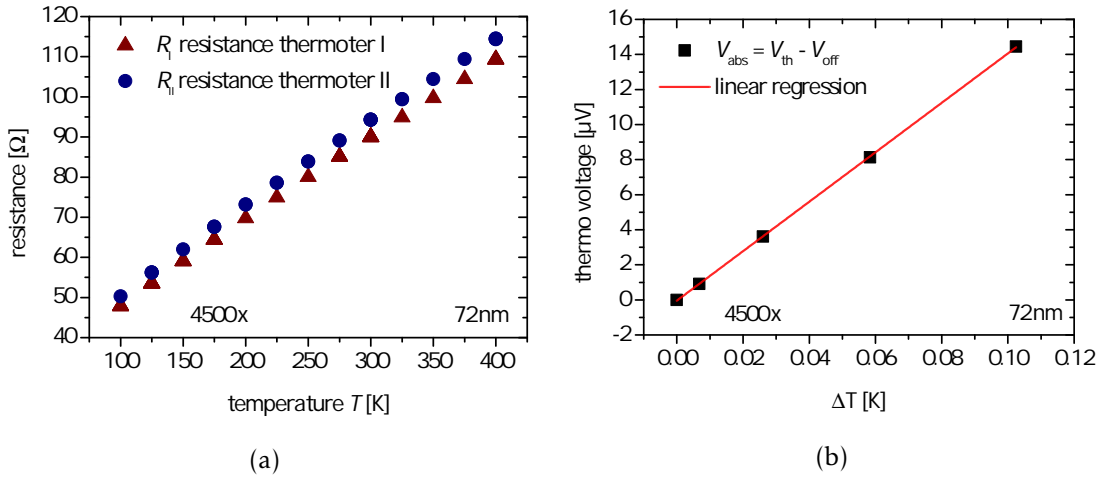


**Figure 5.8:** (a) Resistance in respect to the temperature of both thermometer **I** and **II** of a 4500 x $Sb_2Te_3$. (b) Offset corrected ($V_{\text{off}} = V_{\text{th}}(V_{\text{heater}}{=}0)$) thermovoltage $V_{\text{abs}}$ of the same film measured at $300\,\text{K}$.

by the temperature gradient. The offset corrected thermovoltage ($V_{\text{abs}} = V_{\text{th}} - V_{\text{off}}$) as a function of the temperate gradient ($\Delta T = T_{\text{hot}} - T_{\text{cold}}$) is shown in figure 5.8 (b). From this graph the Seebeck coefficient $S$ is evaluated by assuming the linear approximation $S = \frac{V_{\text{abs}}}{\Delta T}$ is valid for small temperature gradients. Due to an error in the temperature control unit of the used VersaLab, there are problems to stabilise the temperature between 50 and $100\,\text{K}$. For some of the measured films these points are missing. For all films the resistivity thermometers show instabilities between 250 and $400\,\text{K}$, but in a unique manner for every film. Therefore in this region, some of the temperature differences have been interpolated using either: (a) A second order polynomial between the neighbouring temperature regions for each heater voltage. (b) The relation between the heating power and the temperature difference, which is equal to the overall thermal resistance ($\gamma_{\text{d}}$) of the device. This is assumed to be constant for all applied heater voltages, but is a function of temperature.

In addition to the electrical conductivity (temperature $\sigma(T)$ and the magnetic flux $\sigma(T,B)$) depended), the Hall resistance ($R_{\text{Hall}}(T)$) and the Seebeck coefficient ($S(T)$) the Nernst effect $N$ can be measured as well. Therefore both measurement setups have

to be combined. If a temperature gradient is applied by the heater (contacts **III** in figure 5.5) and a magnetic flux is applied perpendicular to the temperature gradient, the inner contacts (named with letters) can be used to measure the Nernst coefficient (contacts **A** and **B** or **C** and **D**).

# Chapter 6

# Transport properties of ALD grown Sb$_2$Te$_3$ thin films

In this chapter measurements on ALD grown Sb$_2$Te$_3$ thin films and the evaluation of the dependence of the transport properties in temperature, magnetic fields and film thickness are shown. All measurements presented here have been performed with either the *Versalab* or *Dynacool* PPMS system (*Quatumdesign*) within measurement temperature regimes of 50 K - 400 K and 2 K - 400 K respectively. Using the device described in the previous section and the DC Seebeck measurement setup (see figure 5.6), the temperature dependence of the electrical conductivity $\sigma(T)$, Seebeck coefficient $S(T)$ and Hall coefficient $R_{\mathrm{H}}(T)$ of thin films thicknesses between 32 to 160 nm are studied. To the best of our knowledge, this is the first time, electronic and thermoelectric properties, especially the Seebeck coefficient, of ALD grown Sb$_2$Te$_3$ are investigated. On the one hand we need to know the thermoelectric transport properties of the different layer thicknesses of Sb$_2$Te$_3$ before covering particles. On the other hand we expect deviations of these transport properties of the ALD grown films in comparison to other thin film deposition techniques, because the comparable low growth temperature is expected to lead to a suppression of the formation of defects that are found to be naturally high in these compounds, due to the very similar electronegativity of both elements (see section 2.3) [44]. The discussion of the measurement results is separated in three sections corresponding to the three major dependencies under which the ALD grown Sb$_2$Te$_3$ thin films are studied in this work: first, the temperature dependence; second, the magnetic field dependence; and third, the influence of thickness of the Sb$_2$Te$_3$ films on the electronic transport properties.

## 6.1 The temperature dependence of the transport properties of $Sb_2Te_3$ thin films

The evaluation of the temperature dependence of the electronic transport properties is a well known method to understand the dominant transport mechanisms in thin films. The three parameters, electrical conductivity $\sigma$, Seebeck coefficient $S$ and Hall coefficient $R_H$ are presented and discussed with respect to the temperature and compared with each other. Due to the different setups used, the temperature regime will be from 50 K - 400 K for the *Versalab* and from 2 K - 400 K for the *Dynacool* system. The Seebeck coefficient measurement are restricted to $T \geqslant 50$ K, since temperature gradient $\Delta T$, as well as the temperature resolution of thermometers decreases with decreasing temperature. This is due to heating power output ($I_{max}$=10 mA) limitation and the decreasing resistance of the metal stripe heater and thermometer to lower $T$ (see section 5.4).

### 6.1.1 Temperature dependence of the conductivity

For all samples the 4-point resistance $R_{xx}(T)$ is measured for different film thicknesses between at least 50-300 K. Since the preferential growth direction was identified to be along the c-axis, the evaluated resistivity corresponds to the in-plane resistance $R_{xx}\perp c$ [35]. With the pre-patterning photolithography step, the device geometry is well defined and the total electrical conductivity $\sigma$ of each film can be evaluated (see section 5.3). The results of these measurements are shown in figure 6.1. All samples show an increasing conductivity with decreasing temperature nearly over almost the entire temperature range, indicating the strong degeneracy of the charge carrier gas and a Fermi level position within the valance band [106]. This temperature dependence is called "metallic behaviour" because in classical metals (as in semiconductors in the extrinsic regime), the carrier concentration is constant and the temperature dependence of the conductivity is dominated by the change of the mobility. The decreasing conductivity in such systems is typically caused by the dominant electron-phonon-scattering, which increases with temperature [107, 108]. In this regime the resistivity-temperature dependence should then obey the power law $\rho \propto T^m$ with a temperature exponent of $m$=1.5 according to the dominant acoustic phonon scattering [109]. In contrast to this, the temperature exponent of the ALD grown $Sb_2Te_3$ thin films is smaller then 1.5 (see figure 6.2 (a)), indicating the presence of other scattering mechanisms contributing to the total mobility $\mu_{tot}$ [1], for example ionized impurity scattering ($m = 1.0$) or grain boundary scattering. Additionally, a change in the carrier

---

[1] regarding to Matthiessen's rule, see equation 3.3.
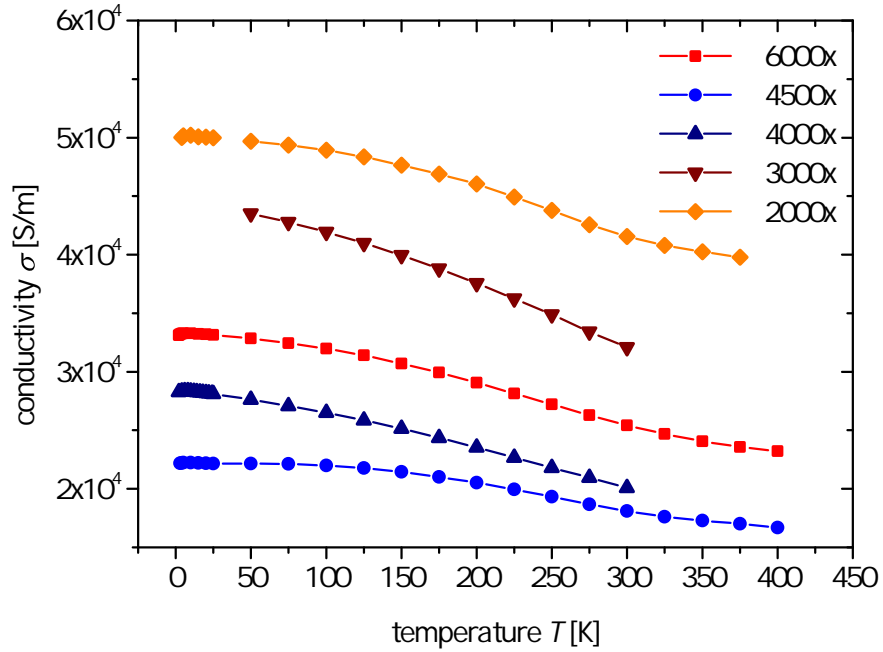
**Figure 6.1:** Temperature dependence of the calculated conductivity for the different ALD-cycles (thicknesses).

effective mass $m^*$ has been addressed to such temperature behaviour [42, 109]. The change of $R_{xx}$ at 300 K to the maximum at around 10 K is only in the range of 20-45% (see figure 6.2 (a)). However, the temperature dependence of $\sigma$ of the $Sb_2Te_3$ thin films is similar, but comparably weaker to single crystal bulk $Sb_2Te_3$ [35, 43, 109, 110]. At around 250 K, the derivation of the conductivity begins to rise again (see figure 6.2 (b)), indicating either a change of the dominant scattering mechanism, or a change of the carrier concentration, due to the excitation of intrinsic electron-hole pairs or of charge carriers of impurity bands. At around $T = 10\,K$, all samples show a global conductivity maximum. In a classical metal transport picture, the conductivity is limited to the scattering events of the impurity scattering, which dominates since the electron phonon scattering nearly vanishes at low temperatures. This would lead to a convergence of the resistance to $\rho_0 = \lim_{T \to 0} \rho(T)$. The effect of the decrease of the conductivity for $T < 10\,K$ will be discussed in section 6.3.

### 6.1.2 Temperature dependence of the Seebeck coefficient

The Seebeck coefficients $S(T)$ of the thin films show a similar temperature behaviour in the measured regime of $50\,K \leqslant T \leqslant 400\,K$ (step-width: 25 K), independent of the ALD cycles deposited. $S$ increases with increasing temperature and shows a maximum at around 350 K. Similar temperature dependence can be found for either bulk,
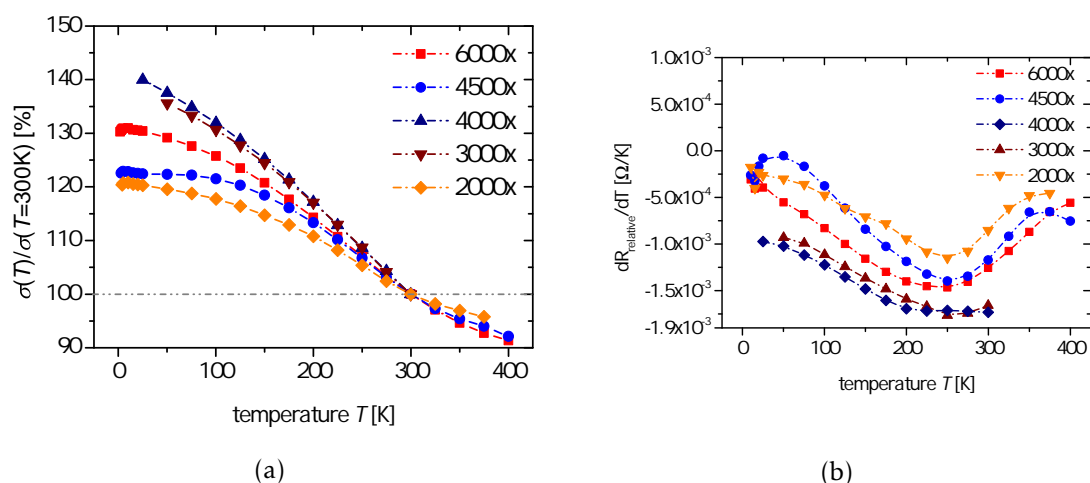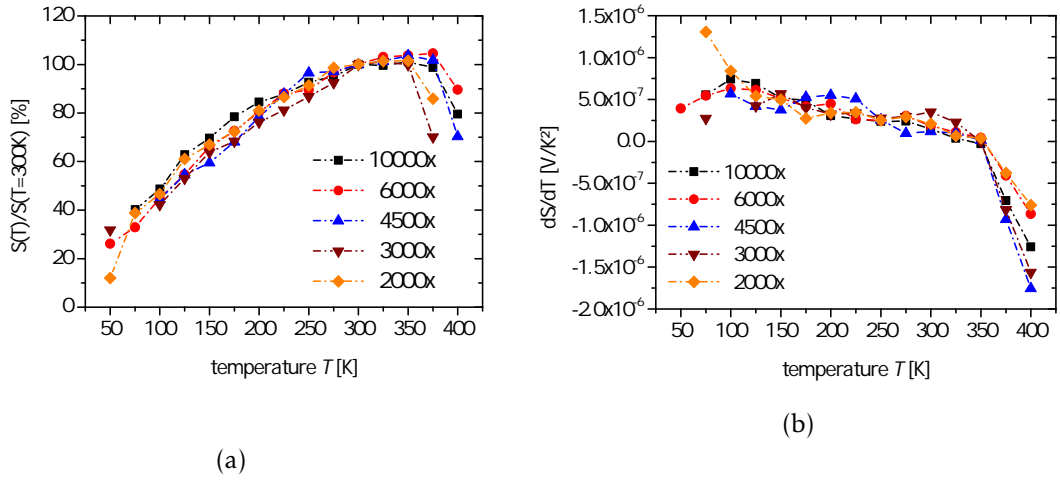
**Figure 6.2:** (a) Relative change of the conductivity with respect to the value of 300 K over the measured temperature regime. (b) Derivative of figure (a) as a function of temperature.

or thin film Bi$_2$/Sb$_2$Te$_3$ and it's alloys for p- as well as n-type materials with different $S_{max}$ in several publications [9, 53, 72, 107, 111]. This temperature behaviour is typical
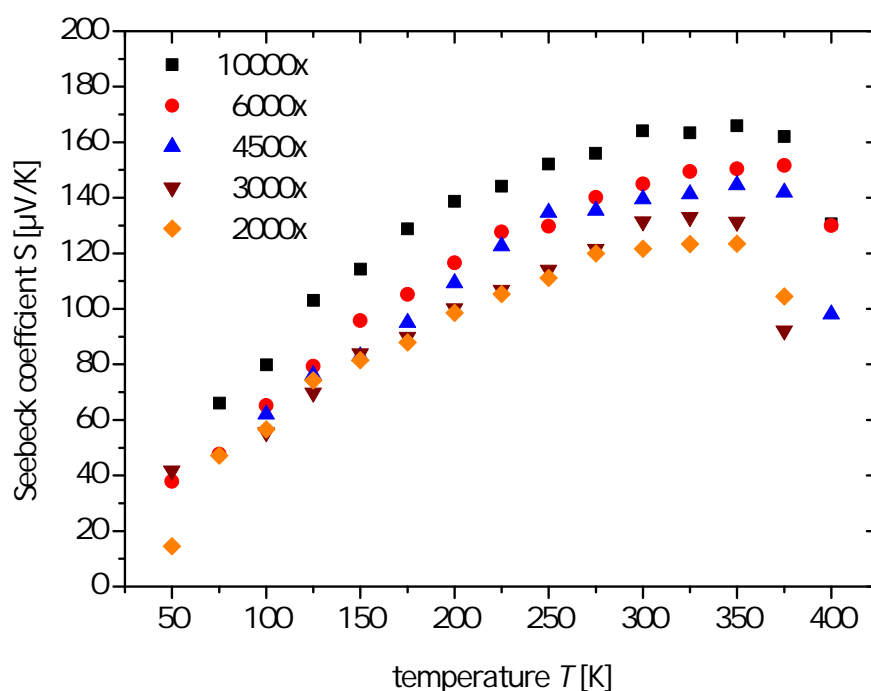


**Figure 6.3:** Seebeck coefficient as a function of temperature for different ALD cycles.

for metals or degenerated semiconductors in the extrinsic region, where the carrier concentration $n$ is constant, which is in consistence with the conductivity results. In the picture of the Boltzmann transport equation ($\tau_e \propto \tau_0 E^r$; where $\tau_e$ is the average

scattering time of the charge carriers) the Seebeck coefficient is a function of the temperature $T$, the Fermi energy $E_F$ and the scattering factor $r$ (see section 2.2). In the region where the $E_F < 4k_BT$ is valid, one can find the approximation for the Seebeck coefficient to be [42]:

$$|S| = \frac{\pi^2}{3}\frac{k_B^2}{e}(r+\frac{3}{2})\frac{T}{E_F},$$ (6.1)

with the Boltzmann constant $k_B$ and the elementary charge $e$. This describes the almost linear increase of $S$ with $T$ found in most metals. Although, the $Sb_2Te_3$ thin films show a similar dependence for $T \leqslant 300\,K$, the $S(T)$ slope changes with temperature. In figure 6.4 (b) the derivation of the Seebeck coefficient (corresponding to the $S(T)$ slope) is shown as function of temperature. The derivation is not constant, resulting in a temperature dependence of either the Fermi energy $E_F$, the scattering factor $r$ or a combination of both, if the assumption of constant carrier concentration is valid. This has been discussed in [97]. Goldsmid *et al.* formulated the temperature dependence



**Figure 6.4:** (a) Relative change of the Seebeck coefficient with respect to the value of $300\,K$ over the measured temperature regime. (b) Derivative $\frac{dS}{dT}$ of the relative change of the Seebeck coefficient as a function of temperature.

of the Seebeck coefficient for $n$=const., which should be valid, if we are in the extrinsic regime [42]. In such case and if the equal-energy-surfaces can be assumed to be spherical or ellipsoidal, the Seebeck coefficient can be found to be [9]:

$$S = \frac{3}{2}\frac{k_B}{e}\cdot\ln T + const.(m^*),$$ (6.2)

where $m^*$ is the effective density of state mass corresponding to the energy dispersion relation which is related to the band structure. In figure 6.5, the Seebeck coefficient is shown as a function of $\ln(T)$ with the linear regression for each layer in the tem-

perature regime between 50 and 300 K, according to the model. Within this regime, the $S \sim \ln(T)$ approximation seems to be quite accurate, but the slope is found to be about half of the value of $\frac{3}{2}\frac{k_B}{e}$ [97]. Similar deviations have been mentioned and discussed for Bi$_2$Te$_3$ in [42, 111], addressed to be a good evidence for more channel conduction due to the complex band structure of Sb$_2$/Bi$_2$Te$_3$. Above 300 K the
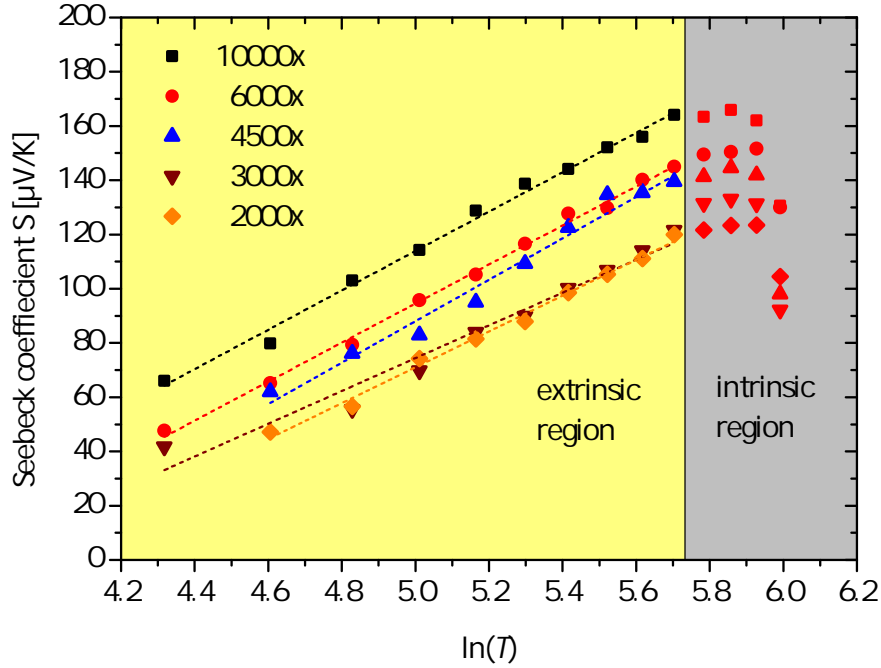


**Figure 6.5:** $S$ as a function of $\ln(T)$ for different ALD cycles corresponding to equation 6.2. The dashed lines are the linear approximations within the assumed extrinsic regime ($n$=const.) for $T \leqslant 300$ K. Above 300 K the change of the $S(T)$ is probably due to the increase of intrinsic charge carriers.

energy of the charge carriers is probably high enough to overcome the band gap of Sb$_2$Te$_3$. The intrinsic carrier concentration starts to become significant and the temperature dependence of the Seebeck coefficient changes to semiconducting behaviour. The peak of $S(T)$ around room temperature is typical for Bi$_2$Te$_3$, which chemical potential position is located in the band gap at this temperature, because of the 10 times lower inherent doping compared to Sb$_2$Te$_3$ [112]. However, the unique chemical casting method and the low deposition temperature of ALD leads to suppressed defect formation and as a result to a 5-10 times lower Hall carrier concentrations $n_{\text{Hall}}$ ($\sim 5 \cdot 10^{18} - 2 \cdot 10^{19}$ cm$^{-3}$, see figure 6.7) compared to values found for single crystalline and polycrystalline ingots of Sb$_2$Te$_3$, typically cast with the Bridgman method[2]

---

[2]A casting method where the element or compound is heated up over the melting point and slowly cooled to the end of the container, resulting in single or polycrystalline growth of the material (see e.g. [113])

($\sim 1 \cdot 10^{20}\,\mathrm{cm}^{-3}$) [43, 109, 114, 115]. Due to the limitation of the PPMS system, no measurements for $T > 400\,\mathrm{K}$ are available. Additionally, one has to be careful with further heating, since irreversible changes in the transport properties of $Sb_2Te_3$ can show up at higher temperatures, e.g. due to: recrystallisation [62, 116], amorphous-crystalline-phase transition [61, 117], formation/transformation of defects (for example $Sb_{Te}$ antisite defects) [73] and/or Tellurium evaporation [78].

### 6.1.3 Temperature dependence of the Hall coefficient $R_H$

For measuring the Hall voltage $U_{Hall}^y$, a magnetic field is applied perpendicular to the current $I_{Hall}^x$, which causes a Lorenz-force to the charge carriers. The Hall resistance $R_{Hall} = \frac{R_{xy}}{B}$ is defined as the slope of the linear approximation of the in-plane longitudinal magneto resistance $R_{xy}(B) = \frac{U_{Hall}^y(B)}{I_{Hall}^x}$. Magnetic fields of $-2\mathrm{T} \leqslant B \leqslant +2\mathrm{T}$ are applied perpendicular to the films surface (see figure 5.3). Since the preferential growth direction is along the c-axis, the Hall resistance is defined as the in-plane Hall resistance $R_{Hall} \perp c$. The Hall coefficient $R_H$ is calculated to

$$R_H = r_H \cdot \frac{R_{Hall}}{t}, \tag{6.3}$$

where $r_H$ is the Hall scattering factor and $t$ is the thickness of the film. The temperature dependence of $R_H$ is shown in figure 6.6 for different film thicknesses. The Hall coefficient is found to be positive for all temperatures and independent from the film thickness, according to the natural hole doping found in $Sb_2Te_3$ and in agreement with the positive Seebeck coefficient. For all samples, $R_H$ is increasing for $10\,K \leqslant T \leqslant 325\,\mathrm{K}$, with a maximum at around $325\,\mathrm{K}$. Corresponding to the peak found in the Seebeck coefficient at this temperature, this is a strong indication for the increase of the intrinsic electron-hole concentration. Using the Lorenz equation for the assumption of one single parabolic band and allowing only elastic scattering, this coefficient is connected to the charge carrier concentration $n_{Hall}$ in the following way [118]

$$R_H = r_H \cdot \frac{1}{e} \cdot \frac{1}{n_{Hall}}. \tag{6.4}$$

In the case of a constant Hall scattering factor ($r_H$=const.), this would lead to a paradoxical decrease of the charge carrier concentration with increasing temperature in ALD grown $Sb_2Te_3$ thin films [97, 109]. In figure 6.7 the resulting carrier concentration is shown as a function of temperature, calculated using equation 6.4 and $r_H$=1, which is a reasonable upper limit for $Sb_2Te_3$ [44]. The Hall scattering factor is connected with the relaxation time and might change with temperature, if the dominant scattering mechanism changes [118]. This influence on $R_H$ in ALD grown $Sb_2Te_3$ thin
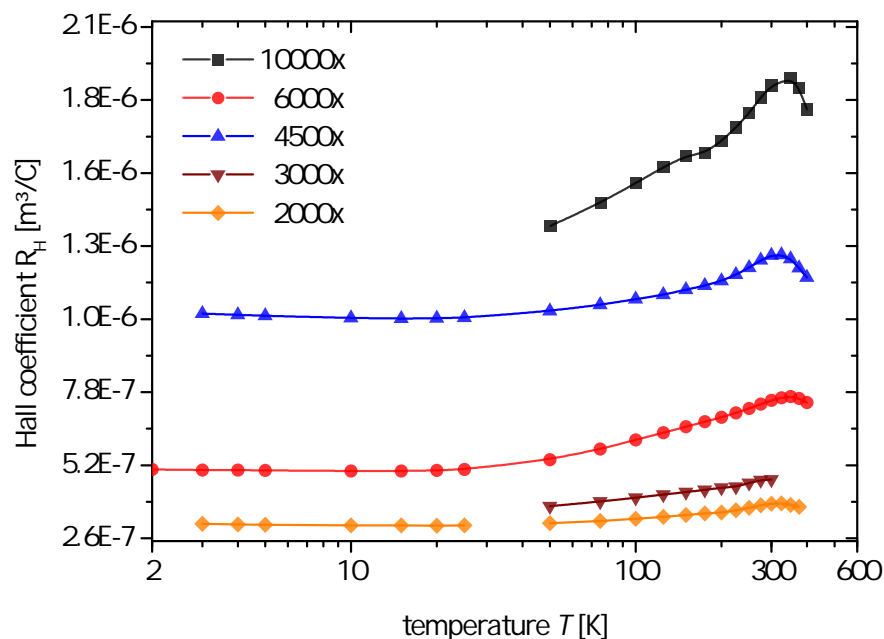
**Figure 6.6:** Temperature dependence of the Hall coefficient $R_H$ calculated with $r_H=1$, for different number of ALD cycles (layer thicknesses).
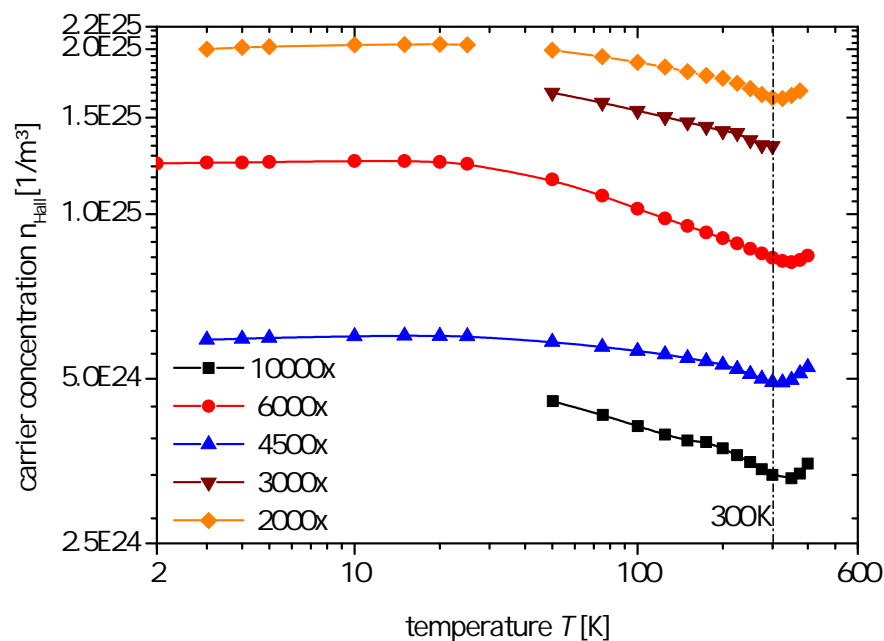


**Figure 6.7:** Temperature dependence of the hall carrier concentration $n_{Hall}$ calculated with the equation 6.4 under the assumption of a single parabolic band, allowing only elastic scattering and using $r_H=1$.

films has been discussed by Zastrow and Gooth *et. al.* [97]. Only little information about this behaviour can be found in literature, but the positive slope of the $R_H(T)$

with increasing temperature has also been connected with the existence of a second valence band contributing to the conduction [109]. Kulbachiskii *et al.* were able to reproduce the positive temperature trend of $R_H$ for $Sb_2Ti_{0.007}Te_3$, with the upper and lower valence band mobilities and hole concentrations calculated by using the Shubnikov-de Haas effect under the assumptions of constant hole concentrations and decreasing mobilities with increasing temperature [109]. However, it was only possible to reproduce this trend for Ti doped $Sb_2Te_3$ single crystals, which temperature behaviour of $R_H$ is different to the dependence found in this work, the existence of more then one conduction channel cannot be excluded for the $Sb_2Te_3$ thin films in this work.

## 6.2 Conclusion: temperature dependent transport properties

The electrical conductivity of the ALD grown $Sb_2Te_3$ thin films is monotonically increasing with decreasing temperature down to about 10 K. This metal like behaviour is typical for strong degenerated semiconductors and natural to $Sb_2Te_3$, since the Fermi energy $E_F$ is expected to be within the valance band probably due to high ability of this compound to form antisite defects [43, 44, 106]. The temperature dependence is much weaker in comparison to the single crystal measurements, indicating a deviating dominant scattering mechanism for thin films, e.g. grain boundary scattering instead of electron phonon scattering. The maximum conductivity is found to be around 10 K, lowering in both temperature directions. At around 275 K the temperature derivation of $\sigma$ shows a minimum, which may be an indication of a change in the dominant scattering mechanism. However, a change of the carrier concentration to higher temperatures is more likely, because a maximum peak of the Hall coefficient $R_{Hall}$ in a similar temperature range can be found. Although, the minimum in $n_{Hall}$ (corresponding to a maximum in $R_{Hall}$) slightly changes for different film thickness, which can be an indication of a small variation in the stoichiometry, the minimum does not depend on the total number of Hall charge carriers. A corresponding extrema can bee seen in the temperature dependence of the Seebeck coefficient, highlighted by a maximum of $S(T)$ in the same temperature regime. The linearity of $S$ with $\ln(T)$ up to 300 K is a signature of the extrinsic (constant carrier concentration) regime [9]. Above 325 K, the Seebeck coefficient starts to decrease as a result of the increasing (intrinsic) carrier concentration [47, 112]. The temperature dependence of the Hall coefficient $R_H$ is quite unique. Contrary to expectations of the extrinsic character of $S$ and $\sigma$, $R_H$ is not constant but increases between 10 and 300 K. As a result the calculated Hall carrier concentrations $n_{Hall}$ (see equation 6.4) show a paradoxical decrease with increasing temperature, indicating either a change in the Hall scattering factor $r_H$ (see Zastrow

and Gooth *et al.* [97]) but being more likely the signature of the existence of a second conduction band [109]. Both, the Seebeck coefficient $S$ as well as the Hall carrier concentration are positive in sign as a consequence of the typically p-type doping of $Sb_2Te_3$. However, due to the unique chemical casting method and the low deposition temperature, the values of $n_{Hall}$ found in this work is orders of magnitudes lower compared to those found in other works, indicating a strong suppression of the native defect content in the ALD grown $Sb_2Te_3$ [43, 72, 73, 76, 109, 114, 115].

## 6.3 Galvanomagnetic measurements - two channel conduction

From the unexpected temperature behaviour of the Hall coefficient (see figure 6.10 (a)) discussed in the above section consequentially follows a decrease of the carrier concentration which is neither consistent with a simple semiconducting, nor with a metal-like transport picture. One explanation for this phenomenon bases on a changing Hall scattering factor $r_H$, due to the shifting of the dominant scattering mechanism in the ALD grown $Sb_2Te_3$ thin films, discussed by Zastrow and Gooth *et al.* [97]. On the other hand, Kulbachiskii *et al.* were able to simulate a change of $r_H$ with temperature in Ti doped $Sb_2Te_3$ single crystals expanding his calculations by adding a second valence band conduction path [109]. Thus the question arises, whether the assumption of simple one-channel conduction is valid for this thin films at all.

A closer look to the magnetic field dependencies of the transversal and longitudinal resistances ($R_{xx}(H)$ and $R_{xy}(H)$ see figure 6.10) give a more detailed picture of the complex mechanisms contributing to the electronic transport in (low dimensional) complex material systems such as $Bi/Sb_2Te_3$ [65, 109, 114, 119–125]. Since the measurement device as well as the PPMS system allows for such measurements without modifications, the herein developed 4-point resistance and the Hall configuration can be used (see figure 5.3). The longitudinal magneto resistance (LMR) $R_{xx}(H)$ shows a quadratic dependence of the magnetic field (see figure 6.10). For non-magnetic semiconducting or metallic materials and compounds, the positive magneto resistance change is a typical signature of two-band conduction [105, 119]. The resistance change is determined by [126]

$$\frac{R_{xx}(H)}{R_{xx}(H=0)} = 1 + \frac{n_1 n_2 \mu_1 \mu_2 (\mu_1 + \mu_2)^2}{(n_1 \mu_1 + n_2 \mu_2)^2} B^2. \qquad (6.5)$$

Since the contributing conductivities ($\sigma_i = e n_i \mu_i$) can not be separated without assuming further approximations to simplify the model, no qualitative values can be extracted from this data. However, since the quadratic dependence of the magnetic fields is valid for magnetic field of $-2\,\text{T} \leqslant \mu_0 H \leqslant +2\,\text{T}$ and down to low temperatures
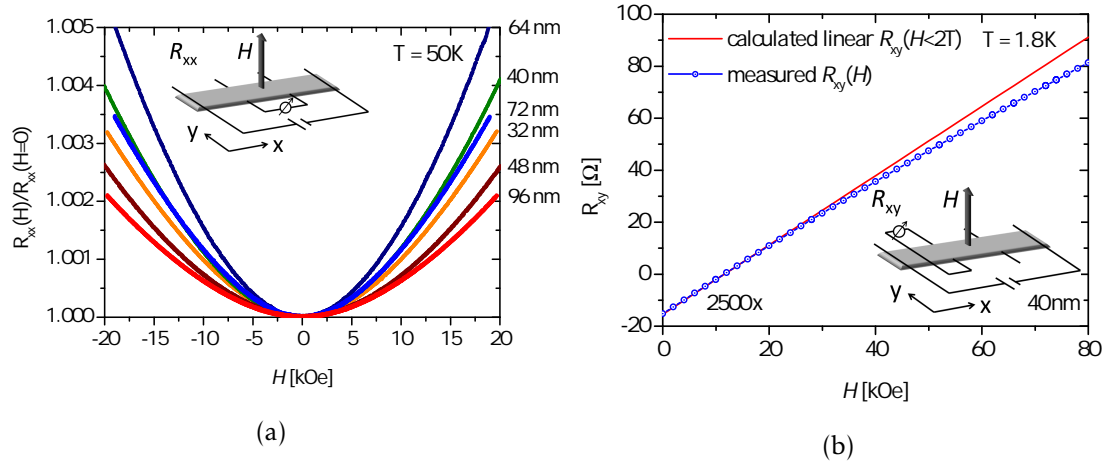
**Figure 6.8:** (a) Transverse magneto resistance ratio of $R_{xx}(H)/R_{xx}(H=0)$ in respect to the applied magnetic field at $T=50\,\text{K}$ for different thin film thicknesses $t$. The curves reveal a pronounced quadratic dependence on magnetic field, showing that multiple conduction channels contribute parallel to the total electrical transport in the thin films [119]. (b) The Hall resistance $R_{xx}$ deviates from linear behaviour at small magnetic fields $\mu_0 H \leqslant 2\,\text{T}$, at low temperatures and high magnetic fields $\mu_0 H > 2\,\text{T}$, as expected from a two conduction channel-model [121]. The insets show the respective measurement geometries.

of about $20\,\text{K}$ for all thicknesses (see figure 6.10), the assumption of two conduction channels contributing to the electronic transport of the ALD grown $Sb_2Te_3$ thin films seems to be very reasonable.

Now we compare the results for transverse magneto resistance $R_{xx}$ with the Hall resistance $R_{xy}(H)$. In section 6.1.3 the $R_{xy}(H)$ has been evaluated for magnetic fields in the range of $-2\,\text{T} \leqslant \mu_0 H \leqslant +2\,\text{T}$ and under the assumption of one conduction channel (or one channel dominating the electronic transport) as previously observed in many $Bi/Sb_2Te_3$ thin film studies, see i.e. [58–62, 64, 97, 127]. This has been reasonable, since the Hall resistances show a linear behaviour in magnetic field. In figure 6.10 (b) the measured $R_{xy}$ of our film as a function of the magnetic field $\mu_0 H > 2\,\text{T}$ at $T = 1.8\,K$ is shown as blue circles. The red line corresponds to the linear interpolation for $R_{xy}(H)$, calculated with the values for magnetic fields between $-2\text{T} \leqslant \mu_0 H \leqslant +2\text{T}$. However, while the linear approximation fits very accurate for low values of B, a deviation between the linear interpolation (red line) and the measured values (blue circles) is observable for higher fields $\mu_0 H \geqslant 2\,\text{T}$. This behaviour is expected for parallel multichannels (with at least two conduction paths) [119–121, 128, 129]. In the two band conduction regime the Hall resistance $R_{xy}(H)$ is given by [130]

$$R_{xy}(H) = \frac{\mu_1^2 n_1 + \mu_2^2 n_2 + (n_1 + n_2)\mu_1\mu_2 B^2}{e\left[(\mu_1 |n_1| + \mu_2 |n_2|)^2 + (n_1 + n_2)^2 \mu_1\mu_2 B^2\right]}. \tag{6.6}$$

Transport properties of ALD grown $Sb_2Te_3$ thin films

Independent of the film thickness, all samples feature a minimum in the resistance (see figure 6.9 (a)) within the measured temperature regime. For a classical semi-conductor with an impurity band, a freeze out regime of the dopant band below a certain temperature is expected, highlighted by an increase in the resistance by orders of magnitudes, due to a strong decreasing carrier concentration, depending on the nature of the impurity band [108]. Whereas in a materials with a metal like conduction the resistance saturates at a residual value due to (temperature independent) impurity scattering [108, 131]. ALD grown $Sb_2Te_3$ thin films neither show a freeze out regime, because of the very moderate slope in temperature, nor a constant residual resistance in both, $\rho$ and $R_H$. The increase of $R_{xx}$ at temperatures below $\approx T < 10\,K$ can be understood with the electron localisation model, introduced by Anderson *et al.* [132]. This effects can occur in disordered systems, like in semiconductor alloys with a large number random distributed impurities and/or defects, where the electron motion is diffusive rather than ballistic. In such systems the probability of random scattering events bringing back the electron to its starting point cannot be neglected, resulting in electron self-interference phenomena. Quantum mechanically the counterwise path has the identical probability which causes a constructive interference of both electron wave functions, causing a higher local probability density - called weak localisation (WL). This coherent back scattering process results in an increase of the resistance, because the localised electrons do not fully contribute to the current flow [65]. Within a characteristic magnetic field $B_\phi$, the resistance increase should disappear since the phase coherence between the two paths is abolished by the field.

This effect leads to a negative LMR effect. Additionally, the electron-electron scattering in a two dimensional system has been addressed as a reason for an increasing resistance at very low temperature in $Sb_2Te_3$ thin films [124, 133]. Due to the Pauli exclusion principle, this scattering event is weak in comparison to other scattering mechanisms [30, 108]. Hence, the contribution to the total scattering time $\tau_{total}$ (Matthiessen rule, see equation 3.3) is only significant at low temperatures, where the temperature dependence of other scattering mechanism nearly vanishes. However, the localisation effect could be one reason for a resistance increase at low temperatures, the magnetoresistance measurements show a different effect in the case of the ALD grown $Sb_2Te_3$ thin films. In fact, at low fields around $\pm 0.3\,T$, a positive LMR can be observed (see figure 6.10 (a)). The form of the field depended resistance is identical to those of the weak anti-localisation effect (WAL), occur in 2-dimensional systems with strong spin-orbit coupling, showing a characteristic sharp dip in the magneto resistivity at low fields (see figure 6.10 (a)) [124, 134]. The localisation probability in such systems is lowered, since the spin-orbit coupling causes a destructive interference of the two paths at the starting point, resulting in an enhanced conductivity. However, similar
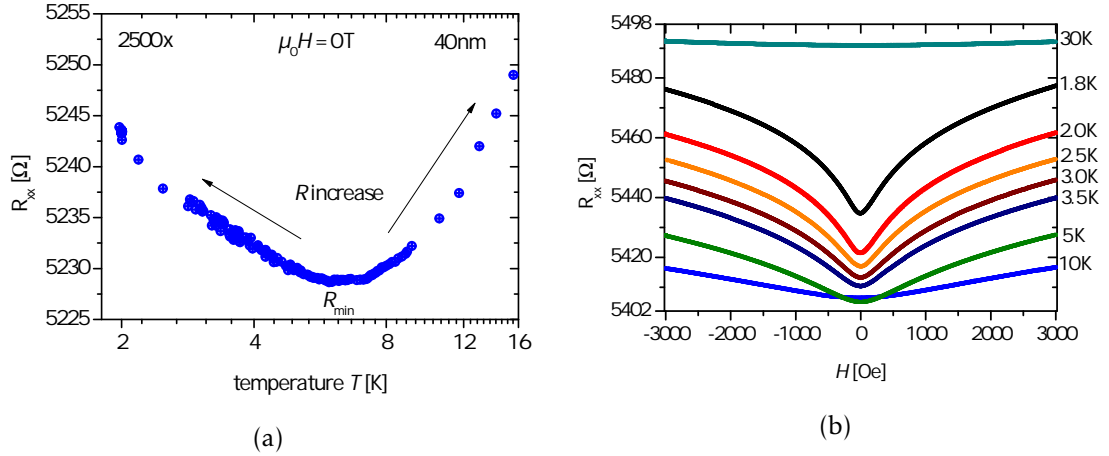
**Figure 6.9:** (a) The $R_{xx}(H = 0)$ with respect to the temperature shows a global minimum over the measured temperature regime. (b) the magnetic field dependence between $-3000\,\text{Oe} \leqslant H_0 \leqslant +3000\,\text{Oe}$ $R_{xx}$ for different temperatures (coloured lines) is shown, highlighting the positive LMR effect.

shaped curves are expected for conductive helical surface states (2D), known as topological insulators (TI), but the origin of the effect is different [65, 124, 125, 129, 134]. These surface states, reveal forward and backward propagating waves (time reversal symmetry - TRS), with oppositely orientated spins because of spin-momentum locking. The quantum correction to the conductivity caused by the Berry phase, which is associated with these TI surface states, shows an exactly identical amplitude and field dependence like the ordinary WAL effect [65, 124, 125, 135–137]. The increase of the conductivity is caused by the destructive electron self-interference between the back scattered electron wave function and its time reversal counterpart, leading to a total absence of back scattering in this states [138]. Actually, both mechanisms result in the very same magneto resistance field dependent behaviour. It is therefore impossible to distinguish between both (2D) mechanisms by just taking the low field magneto resistance results into account.

At high fields ($-9\,\text{T} \leqslant \mu_0 H \leqslant +9\,\text{T}$) and low temperatures a non saturating LMR can be observed (see figure 6.10 (b)), approximating to a linear dependence of MR in $H$. Such behaviour has been observed in chalcogenide $V_2VI_3$ bulk material as well as thin films [133, 139]. Three effects are related to such non-saturating linearity at high fields: first, strong disordered semiconductor systems, being consistent with the Anderson localisation [140]; second, Fermi surfaces with open orbits in some crystallographic direction could lead to this effect, highlighting the anisotropy of the $Sb_2Te_3$ in general (see figure 2.3), as well as the polycrystalline character of the ALD grown films in special [133]; third, Abrikosov *et al.* developed a theory, from which a linear and positive LMR is expected for the existence of linear $E - k$ dispersion relation in a gap-

less semiconductor, which can be related with topological insulator states because of their identical dispersion relation [139,141]. However, there are several explanations, the approximating linearity limit seems to be independent from temperature which would lead to the suggestion, that the responsible mechanisms does not depend on the carrier mobility. In fact, these low temperature magnetic field dependencies of
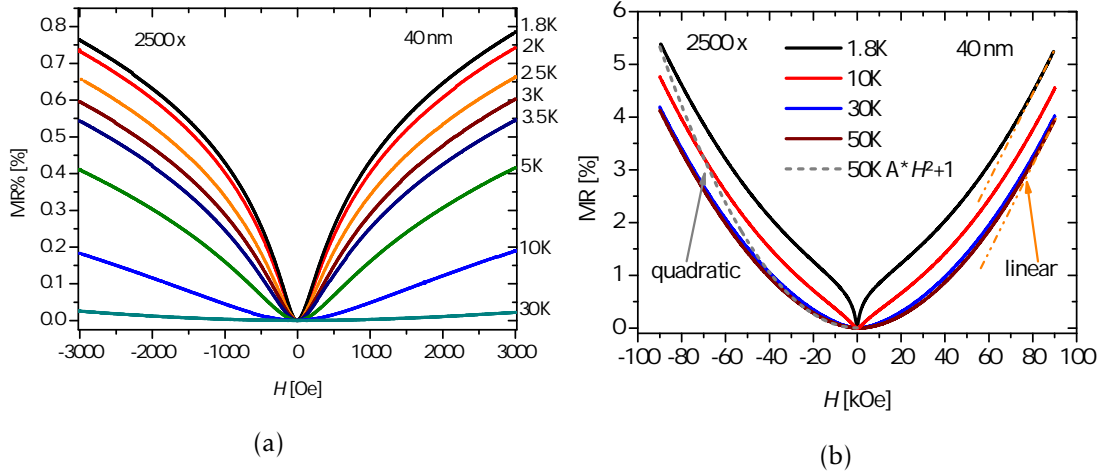


**Figure 6.10:** (a) The relative change of $R_{xx}(H)$ in respect to $R_{xx}(H = 0)$ in % for the low temperature regime. (b) Magnetoresistance for $-9\,\mathrm{T} \leqslant \mu_0 H \leqslant +9\,\mathrm{T}$ (solid lines). The dashed and dashed dotted lines indicated the quadratic behaviour for low fields and the linear behaviour for high fields.

$R_{xy}(H)$ and $R_{xx}(H)$ have been experimentally and theoretically associated with 2D (surface) states (TI surface states), especially in (doped) $V_x - VI_y$ nanostructures like $Sb_2Te_3$, $Bi_2Te_3$, $Bi_2Se_3$ thin films, heterostructures, nanoribbons and nanowires, see e.g. [80, 123–125, 129, 133, 134, 142–146]. Although, one might take these magneto transport properties as signatures of additional two dimensional conduction in the ALD grown $Sb_2Te_3$ thin films, these features are no evidence for a low dimensional transport channel[3] in this system.

## 6.4 Evaluation of the thickness dependence

Due to the good controllability of the ALD process, the film thickness can be precisely tuned. The lower limit of the thickness is given by the electrical non closeness of the films due to the island growth and can be found to be about 32 nm. The only upper limit can be addressed as the deposition time, since 100 nm film thickness take about 200 hours - more than one week (see section 4.2). Hence the magnetic field dependent

---

[3]Which of course includes also topological insulator states.

resistances described in section 6.3 are possible signatures of low dimensional conduction channels, amongst others, we are interested if we are able to observe indications of such features in the transport properties. Since a 2D conduction path should be constant in respect to the thin film thickness $t$ in a first approximation, $S$, $\sigma$ and $R_{\text{Hall}}$ should vary with $t$ if the 2D path conduction contribution is in the order of the bulk channel. Although low temperature measurement can show interesting effects, we should focus on the room temperature transport properties, since this is most likely the application temperature. For evaluation of this dependence, all measurement values have been plotted against the film thickness for $T = 300\,\text{K}$ (see figure 6.11). In
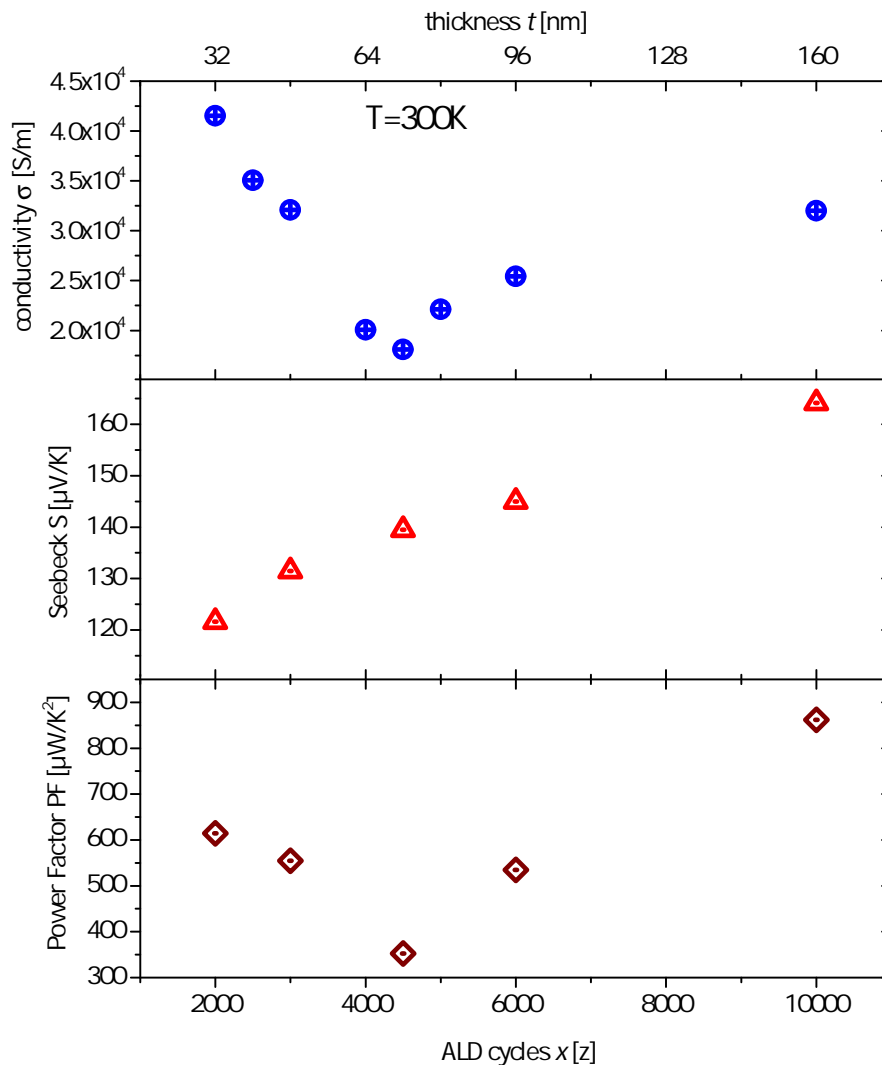


**Figure 6.11:** Transport properties as function of film thickness. From the top: Electrical conductivity, Seebeck coefficient and Power Factor at 300 K.

Transport properties of ALD grown $Sb_2Te_3$ thin films

the upper part of figure 6.11 the electrical conductivity $\sigma$ in respect to the film thickness $t$ is shown. The 300 K values of $\sigma$ variate between 1.8 and $4.2 \cdot 10^4$ S/m. What attract attention first, is the non monotonic behaviour of $\sigma(t)$ which splits up $\sigma(t)$ in two regimes. Above 72 nm, the upper conductivity regime (UCR), $\sigma$ increases inverse hyperbolic with the film thickness. Below 72 nm the conductivity (lower conductivity regime - LCR) increases nearly linear with decreasing $t$ (see figure 6.12). The Seebeck coefficient $S$ shows a clear trend over the whole thickness regime. Following the inverse hyperbolic trend of UCR, $S$ decreases from 165 µV/K for $t$=160 nm to 122 µV/K for $t$=32 nm film thickness (see figure 6.11). Since the power factor is determined by $PF = S^2\sigma$, the thickness dependence follows the trend of the stronger changing electrical conductivity but suppressed by the decreasing Seebeck coefficient.

With decreasing the thin film thickness the ratio of the contribution of different



(a)

(b)
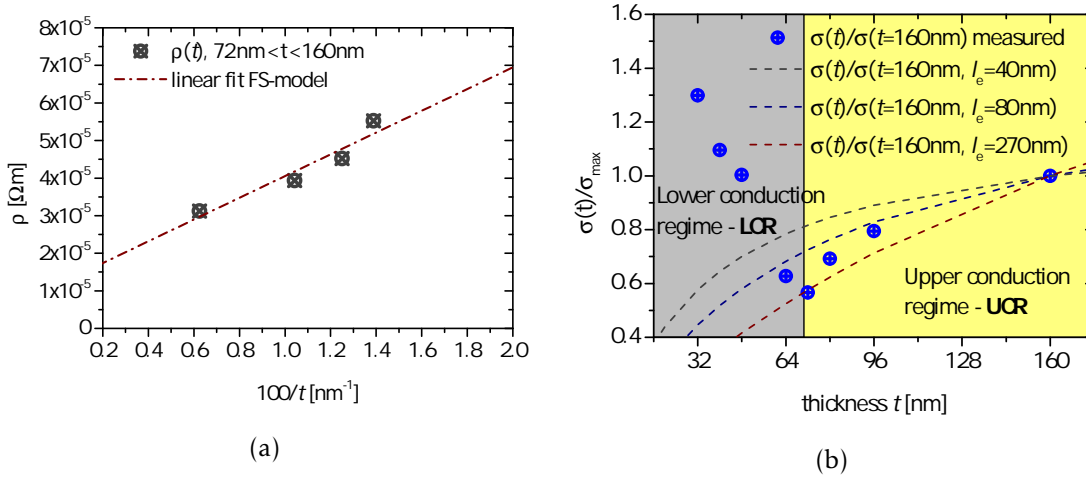
**Figure 6.12:** (a) The electrical resistivity in respect to inverse film thickness for 72 nm$\leqslant$ $t \leqslant$160 nm. The dash-dotted line correspond to the linear approximation of $\rho$ to $1/t$ in respect to the Fuchs-Sondheimer model (FS-model - see text). The measurements are in excellent qualitative agreement comparison to the work of Das *et al.* [61]. (b) The relative electrical conductivity as a function of film thickness - the two conduction regimes are highlighted. In blue circles the relative changes of $\sigma(t)/\sigma(t = 160\,\text{nm})$ are shown. The blue and wine dashed lines correspond to the calculations of the change of $\sigma(t)$ compared to $\sigma(t = 160\,\text{nm})$ using the FS-model for three different mean free paths $l_\text{e}$.

scattering mechanisms can change (e.g. surface or grain boundary see section 3.2). According to the Matthiesen rule (see equation 3.3) all scattering mechanisms effect the total mobility $\mu_\text{total}$ of the charge carriers and therefore the conductivity $\sigma$. We start the discussion of this influence with the decreasing trend of $\sigma$ down to 72 nm. This behaviour can be understood with the (semi)-classical Fuchs-Sondheimer model (FS-model) [61,67,68]. Fuchs *et al.* The total mobility is decreased by scattering of the charge with the film surface, if the film thickness $t$ is in the order of the mean path

of the charge carriers $l_e$ (see section 3.2) [67, 147]. With decreasing film thickness, the conductivity is reduced compared to the bulk conductivity, due to increasing surface scattering probability (see equation 3.6). This fact has been discussed by Das *et al.* who studied the influence of the film thickness (between 50 and 200 nm) on the electrical resistivity of polycrystalline $Sb_2Te_3$ films grown by co-evaporation [61]. By fitting the resistivity to equation 3.6, he estimated a hole mean free path of $270\pm20$ nm at 300 K but with unknown specularity factor $p$ [61]. In figure 6.12 (a) the very same evaluation has been made for UCR - resistivity data, showing an excellent qualitative agreement with the results of Das *et al.* (see figure 9.7 in the appendix) [61]. However, if we change the picture to the conductivity vs. thickness plot and do similar FS-model calculations, the deviation of the calculated values become apparent. In figure 6.12 (b) the relative change of $\sigma$ can be found. The dashed lines correspond to the calculated characteristics according to the FS-model for different electron mean free paths $l_e$=40 nm to 270 nm (specularity factor factor $p$ of 0.1 - representing the high diffusive scattering probability due to surface roughness). The range of the electron mean free path is chosen to be between the grain size found in this work for the lowest number of ALD cycles (see figure 4.14 (b)) as the lower limit and the value found by Das *et al.* as the highest limit [61]. These values of $p$ and $l_e$ are used for all further calculations. The reason for the deviation between the measurement and the calculated FS-model values can be found in the growth behaviour of $Sb_2Te_3$ thin films. The strong island growth leads to growing grains (grain size) with increasing film thickness [94]. Figure 6.13 (a) shows a scheme, which demonstrates the increasing grain size with increasing film thickness. For $t < 32$ nm the formation of polycrystalline free standing islands due to significant surface diffusion is preferred, resulting in electrical non closed films. This island growth is expected for low-temperature depositions on amorphous substrates [148]. With further increasing the number of ALD cycles ($t \geqslant 32$ nm), the amount of material is increased and the island grow together. With further increasing thickness, the system attempt to minimize the overall interface energy [94]. The drives the coalescence of the grains with the effect of an increasing grain size with increasing film thickness. As described in section 3.2, grain boundary scattering has to taken into account as an additional mechanisms in such thin films, where the electron mean free path $l_e$ is in the order of the grain size. To estimate the influence of both scattering mechanisms, surface and the decreasing grain boundary scattering with increasing thickness, the total conductivity $\sigma$ has been visualized by using *Mathematica*. Figure 6.13 (b) shows such plot. The thickness dependence of the conductivity $\sigma$ (z-axis) is calculated with the help of the FS-model. The y-axis correspond to the bulk conductivities $\sigma_{bulk}$, representing the changing conductivity (mobilities) as a function of the thin film thicknesses, which is a function of the grain
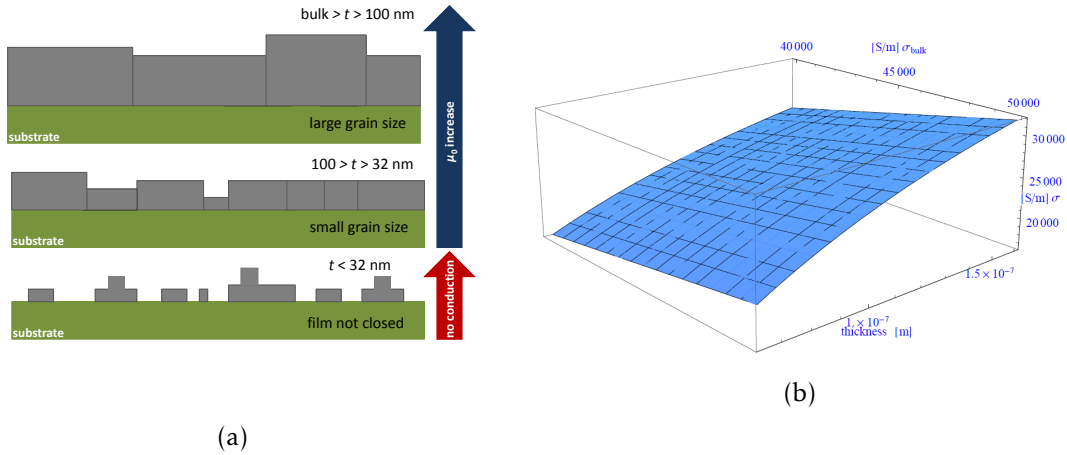
(a)

(b)

**Figure 6.13:** (a) Schematic diagram of the lateral grain size growth with increasing thickness as a consequence of the island growth of ALD $Sb_2Te_3$ thin films (see section 4.2 and [94]). Simulated behaviour of the total conductivity $\sigma$ (z-axis) as a function of the thickness $t$ (x-axis) with taking into account the FS-model (x-z-lines) for different bulk conductivities $\sigma_{bulk}$ (mobilities) in respect to the influence of different grain size (y-z-lines). The measured conductivity is probably a diagonal on this plain, depending on the grain size growth as a function of thin film thickness.

size. As a consequence both mobility contributions depended on the film thickness, which is shown on the x-axis for values of $t$ between $72 \cdot 10^{-9}$ m $< t < 160 \cdot 10^{-9}$ m, coherent with the UCR. The measured values can be found as a diagonal of this graph. So the derivations from the FS-model can be understood by an increase in the mobility (to be more precise: an increase of the hole mean free path, which also affects the FS-model-calculation) with increasing grain size as a function of $t$. However, since the dependence of grain size growth (mean free path) in respect to the film thickness is not known, eligibility of further (quantitative) data fitting is not given.

Now we have a reasonable model to describe the decrease of the conductivity with decreasing film thickness, we have to think about the LCR regime for thicknesses below 72 nm. Therefore one has to remind the magnetic field dependent resistances, discusses in section 6.3. The signatures can be found to be characteristic for an (or more) additional 2D conduction channel. Taking this into account, one can formulate a simple modification to the conductivity[4] of such films, with the approximation of two non interacting parallel channels. With $\sigma_{3D}$ represents the 3D channel as a function of $t$ corresponding to the FS-model and $\sigma_{2D}$ as the 2D conduction contribution one can find:

$$\sigma = \sigma_{3D} + \sigma_{2D}$$
$$= \sigma_{bulk}\left[1 - \frac{3}{8}\frac{l_e}{t}(1-p)\right] + G_{2D}/t. \tag{6.7}$$

---

[4]Obeying the Matthiessen rule, that independent scattering mechanisms are additive in conduction.

Since a constant 2D conduction $G_{2D}$ should be thickness independent, the contribution of $G_{2D}$ to the total conductivity is scaled with the thickness $t$. In figure 6.14 the trend of both contributing conductivities ($\sigma_{2D}$ and $\sigma_{3D}$) are plotted as a function of thickness. Similar to the scaling of the $\sigma_{FS}$ contribution, the calculated $\sigma_{2D}(t)$ has been scaled with the value of $\sigma_{2D}(t = 32\,\text{nm})$. For this calculations the carrier concentration of both channels is assumed to be constant in film thickness, which seems to be a reasonable approximation with respect to the temperature dependent results (see section 6.2). As mentioned earlier, the quantitative conduction values of both channels should not be extracted from this data, since the actual ratio is (1) not known and (2) may change with the film thickness for reasons like grain boundary scattering, film roughness and others. However, the qualitative trend of the thin film thickness dependency, including both, the FS-model and the 2D conductivity for the UCR and LCR respectively, is in good agreement with the experimental values. It seems that further unknown influences, play a minor role in contribution to the total conductivity in both regimes.

The best consistency check is, to apply the two channel conductivity model to the
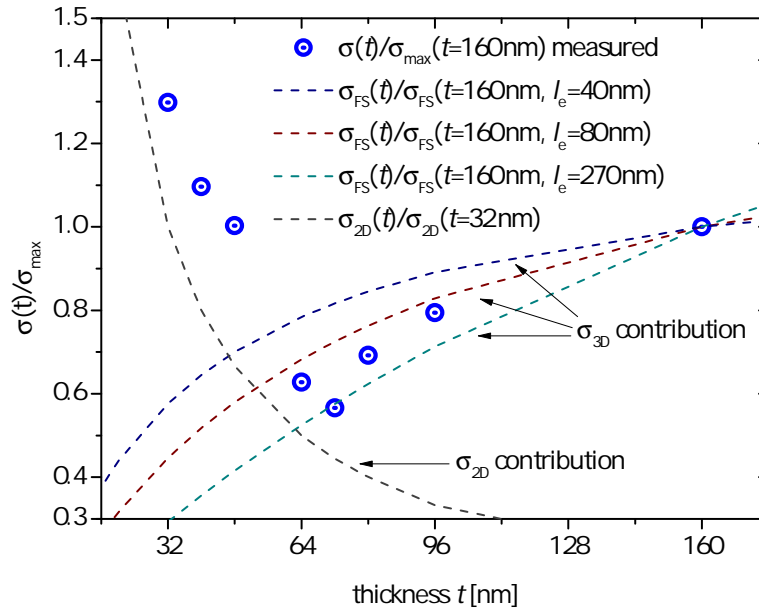


**Figure 6.14:** The dashed lines show the conductivity contribution of $\sigma_{3D}$ for two different $l_e$ in the UCR. As dotted line the calculated conductivity contribution of a second 2D conduction path $\sigma_{2D}$ is shown, being dominant in the LCR.

simultaneously measured values $S$ and $R_H$. The Seebeck coefficient shows a monotone decrease with decreasing film thickness and therefore, in contrast to the electrical conductivity, only one regime (see figure 6.11). However, this behaviour can be understood by using the 2-band Seebeck-model combined with the two conduction

---

Transport properties of ALD grown $Sb_2Te_3$ thin films

regime approach discussed above. If there are two parallel conduction paths in the direction of the temperature gradient, the total Seebeck coefficient $S_{\text{tot}}$ is determined by the following equation [6]:

$$S_{\text{tot}} = \frac{S_1 \sigma_1 + S_2 \sigma_2}{\sigma_1 + \sigma_2}.$$ (6.8)

Taking into account, that the contribution of one of the current (and heat) path is 2D like - in consistence with the conductivity calculations - we have to modify the equation in the following way:

$$S_{\text{tot}}(t) = \frac{S_{\text{3D}} \sigma_{\text{3D}} + S_{\text{2D}} \frac{G_{\text{2D}}}{t}}{\sigma_{\text{3D}} + \frac{G_{\text{2D}}}{t}}$$ (6.9)

Since $\sigma_{\text{3D}}$ is also thickness dependent, we have to modify the equation once again by using the FS-model for $\sigma_{\text{3D}}(t)$ (see equation 3.6):

$$S_{\text{tot}}(t) = \frac{S_{\text{3D}} \sigma_{\text{bulk}} \left[ 1 - \frac{3}{8} \frac{l_e}{t} (1-p) \right] + S_{\text{2D}} \frac{G_{\text{2D}}}{t}}{\sigma_{\text{bulk}} \left[ 1 - \frac{3}{8} \frac{l_e}{t} (1-p) \right] + \frac{G_{\text{2D}}}{t}}$$ (6.10)

Within this model, the Seebeck coefficient and the carrier concentration of both channels are assumed to be constant like in the conductivity calculations. Because we are not able to distinguish between the absolute Seebeck coefficients of the two channels, $S_{\text{3D}}$ and $S_{\text{2D}}$, we have to estimate the relation between both. Since the 2D-channel is assumed to be more metal like than the 3D state, $S_{\text{2D}} < S_{\text{3D}}$ seems to be a reasonable estimation [27]. Figure 6.15 shows the relative change of the measured Seebeck coefficient $S(t)/S(t = 160\,\text{nm})$ (red rectangulars) in respect to the layer thickness for $T = 300\,\text{K}$. The blue and wine dashed lines show the relative change of $S_{\text{tot}}(t)/S_{\text{tot}}(t=160\,\text{nm})$ calculated with the relative changes of the conductivity (shown as black dotted lines) using equation 6.10, a mean free path $l_e$ of 40 nm and a ratio of $S_{\text{3D}}/S_{\text{2D}}$ of 0.5 and 0.3 respectively. Similar to the conductivity calculation, small derivations from the calculated thickness dependency of the Seebeck coefficient, using the combined FS- and 2D-model, can be understood with the change of the mobility with decreasing film thickness due to the reduced grain size. In the presented calculations the mobility dependence of the bulk Seebeck coefficient is neglected. According to the Mott expression for degenerate semiconductors, the $S_{\text{3D}}$ is inverse proportional to the mobility $\mu_{\text{bulk}(t)}$ which possibly leads to a additional correction for $S_{\text{total}}$ [149,150].

As the third measurement value, the thickness dependency of the Hall coefficient $R_{\text{H}}(t)$ has to be evaluated with the 2-channel conduction-model used for $\sigma$ and $S$. Within the one band model, or if one conduction contribution is dominant, $R_{\text{H}}(t)$ is
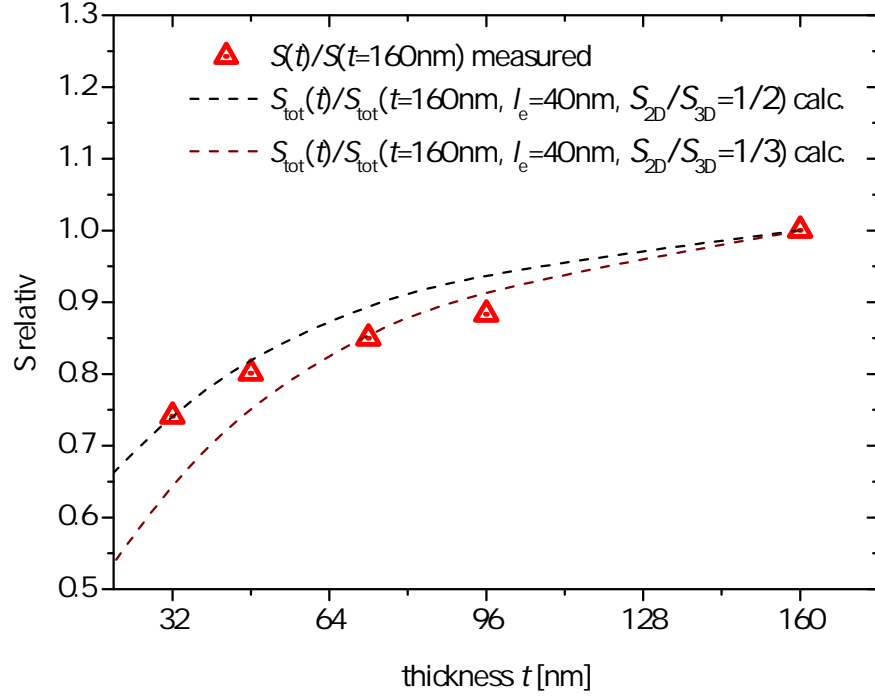
**Figure 6.15:** The red triangles show the relative change of the $S(t)$ in respect to maximum See-beck coefficient of $S(t=160\,\text{nm})$ as a function of film thickness. The blue and wine dashed lines correspond to the calculated change of the Seebeck coefficient using equation 6.10 for $S_{2D}/S_{3D}$ ratios of 0.5 and 0.3 respectively.

inverse proportional to the carrier concentration $n_{\text{Hall}}$ (see equation 6.4). In the case of two conduction paths contributing to the total conduction, the ratio of both, carrier concentrations as well as mobilities, has to be taken into account. Using the expression for $R_{\text{Hall}}(t)$ in such case, one can find [151]:

$$R_{\text{H}} = \frac{n_1\mu_1^2 + n_2\mu_2^2}{e(n_1\mu_1 + n_2\mu_2)^2}. \tag{6.11}$$

Equation 6.11 reveals the difficulty of modelling the two band Hall coefficient for unknown carrier concentrations $n_i$ and mobilities $\mu_i$ and of course in for additional thickness dependency. However, the mobilities $\mu_1$ and $\mu_2$ can be substituted by the conductivity $\sigma_1$ and $\sigma_2$ and equation 6.11 transforms to:

$$R_{\text{H}} = \frac{\frac{1}{n_1}\sigma_1^2 + \frac{1}{n_2}\sigma_2^2}{e(\sigma_1 + \sigma_2)^2}. \tag{6.12}$$

Now we have to extend the 3D two band model into one 3D (bulk) channel and one 2D channel, in the same way the Seebeck coefficient and the electrical conductivity have been evaluated: By the use of the expression for $\sigma_{3D}$ (FS-model) and the 2D

conductivity $\sigma_{2D} = G_{2D}/t$. Weighting $n_2$ with the thickness ($n_{2D}/t$, where $n_{2D}$ is the sheet carrier concentration), one can find equation 6.12 to:

$$R_{H} = \frac{\frac{1}{n_{3D}t}\left(\sigma_{bulk}\left[1 - \frac{3}{8}\frac{l_e}{t}(1-p)\right]\right)^2 + \frac{1}{n_{2D}}\frac{G_{2D}^2}{t^2}}{e\left(\sigma_{bulk}\left[1 - \frac{3}{8}\frac{l_e}{t}(1-p)\right] + \frac{G_{2D}}{t}\right)^2}. \tag{6.13}$$

Figure 6.16 shows the relative change of the measured (orange hexagons) and the
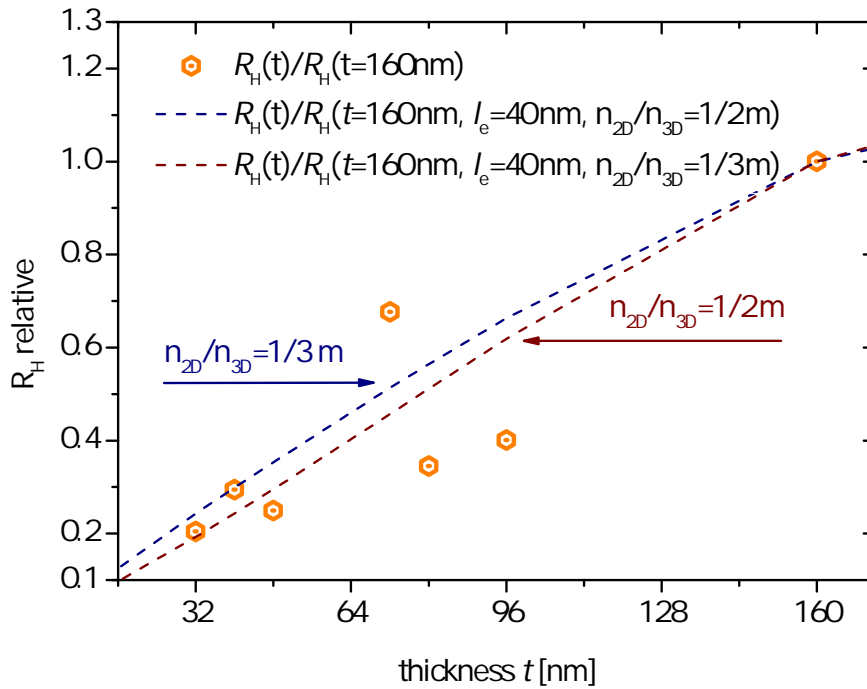


**Figure 6.16:** The relative change of $R_{H}(t)$ with film thickness (in orange hexagons). The blue and wine dashed lines correspond to the calculated change of $R_{H}(t)$ using equation 6.13 and $n_{2D}/n_{3D}$ ratios of $1/2$ m and $1/3$ m respectively.

calculated (dashed lines) Hall coefficients $R_{H}(t)/R_{H}(t=160\,\text{nm})$ as a function of film thickness. The carrier concentrations $n_{3D}$ and $n_{2D}$ are assumed to be constant, since the stoichiometry is not expected to change with changing film thickness. Again we have used $l_e = 40\,\text{nm}$ as the lower limit for the mean free path in the direction of transport and $p = 0.1$ as surface scattering factor. The calculations have been performed with ratios of $1/2$ m and $1/3$ m for $n_{2D}/n_{3D}$. In figure 6.16 the calculated thickness dependencies are shown as dashed lines. Although, the mobility change due to the grain size effects is neglected, the calculated values are in good agreement with the measurement results.

## 6.5 Conclusion on the thickness dependent properties

All measured transport properties, show a significant thickness dependence. Specifically, electrical conductivity $\sigma$ can be split up in two regime thickness regimes: (1), the upper conductivity regime UCR for $t \geqslant 72\,\text{nm}$, where the $\sigma$ is inversely proportional to $t$, and (2), the lower conductivity regime (LCR) for $t < 72\,\text{nm}$, where $\sigma$ is increases linearly with decreasing film thickness. In contrast to the thickness dependence of $\sigma$, the Seebeck coefficient $S$ does not split up in two regimes, but monotonously decreases with decreasing film thickness. The Hall coefficient $R_{\text{Hall}}$ shows a decreasing trend with respect to the film thickness.

Taking the results of the galvanomagnetic and low temperature transport behaviour into account, which show signatures of a 2D conduction channel contributing parallel to the bulk conduction, we have employed a 2 channel transport model for the thickness dependence of all transport properties at 300 K, modifying the t-dependence of each channel individually. While the UCR is dominated by the bulk channel, the LCR is dominated by the 2D channel. The change of $\sigma$ in the UCR can be understood with the Fuchs Sondheimer-model (FS-model), as it has been seen in co-evaporated $Sb_2Te$ thin films [61, 67, 147]. Surface scattering reduces the mobility of the charge carriers an therefore the conductivity (see equation 3.6), due to fact, that the thickness $t$ is in the order of the electron mean free path $l_e$ [67, 147]. However, while the general trend can be described within this model, the reduction of $\sigma$ on $t$ is larger compared to the calculated $\sigma_{\text{FS}}$ FS-model. This stronger reduction is a result of the decreasing grain size with decreasing film thickness, caused by the Volmer Weber island growth behaviour of ALD grown $Sb_2Te_3$ thin films (see figures 6.13 (a), (b) and 4.9) [37, 64, 94]. As lower limit, a mean free path of $l_e = 40\,\text{nm}$ with a specularity factor of $p = 0.1$ has been evaluated. In contrast the decreasing conductivity with decreasing film thickness in the UCR, $\sigma$ increases nearly linear with $t$ if the thickness is further reduced ($t < 72\,\text{nm}$ - the LCR). In this regime, the 2D conduction channel seems to start contributing significantly to the transport. Therefore this 2D conduction path is added into the calculations. The combination of both conduction paths trace the qualitative trend of the relative change of $\sigma$ in UCR as well as in the LCR (see figure 6.14) very well.

Because the conductivity can be described, the model is successfully transferred to the thickness dependent results of the Seebeck coefficient $S$ and the Hall coefficient $R_{\text{H}}$. The decreasing $S_{\text{tot}}$ with respect to $t$ is function of the conduction contributions of $\sigma_{\text{2D}}(t)$ and $\sigma_{\text{3D}}(t)$ as well as the ratio between $S_{\text{2D}}/S_{\text{3D}}$. In consistence with the conductivity calculation, the relative change $S_{\text{tot}}(t)$ is evaluated with the lower limit of the

carrier mean free path $l_e = 40\,nm$, a specularity factor of $p = 0.1$ and ratios of $S_{2D}/S_{3D}$ equal to 1/2 and 1/3 respectively, since the metallic $S_{2D}$ is calculated to be smaller compared to the semiconducting $S_{3D}$ [27]. However, there seems to be an influence of the changing mobility in $S_{3D}$, the calculated thickness trend of $S_{tot}(t)/S_{tot}(t=160\,nm)$ are in good agreement with the measured $S(t)/S(t=160\,nm)$.

The Hall coefficient $R_H(t)$ in the two band model depend on the contributing charge carrier densities $n_i$ and mobilities $\mu_i$. The mobilities have been substituted by $\sigma_{2D}(t)$ and $\sigma_{3D}(t)$ (see equation 6.11. For the relation of the carrier densities $n_{2D}/n_{3D}$ ratios of 1/2 m and 1/3 m are chosen[5] [129]. However, the variation of $R_H(t)$ with $t$ seems to be a bit higher as for the conductivity and the Seebeck coefficient, the qualitative trend of the decreasing relative Hall coefficient $R_H(t)/R_H(t=160\,nm)$ with decreasing $t$ is described by the model (see figure 6.16).

A 2-band conduction model has been investigated to evaluate the thickness dependence of the three independent measured values $\sigma(t)$, $S(t)$ and $R_H(t)$. The model include the Fuchs-Sondheimer equation for surface scattering and a 2D conduction channel, showing qualitatively good agreement between calculation and measurement. However, no quantitative results are given, since the relation between the 3D bulk and the 2D channel of $n_i$, $\mu_i$ and $S_i$ are not exactly known and cannot be extracted from the thickness dependent results without assuming further simplifications.

## 6.6 Conclusions of ALD grown $Sb_2Te_3$ thin films

The electronic and thermoelectric properties of bulk $Sb_2Te_3$ has been intensively studied since the 1950's especially because of it's good thermoelectric performance at around room temperature as p-type material (see e.g. [152,153]). After the theoretical prediction of the enhancement of the thermoelectric figure of merit $ZT$ in quantum-well structures by Hicks and Dresselhaus in 1993 and the $ZT$ record publication of Venkatasubramanian *et al.* in 2001, who claim to achieve a $ZT$ of 2.4 at MOCVD grown superlattice structure of alternating $Sb_2Te_3$-$Bi_2Te_3$ layers, the interest in $Sb_2Te_3$ thin films rise [13, 19]. The properties of such thin films grown with several different deposition methods have been studied (see figure 4.2) [58–64, 72–76]. However, in this work, it is the first time that the electronic and thermoelectric properties of ALD grown $Sb_2Te_3$ with respect to the temperature $T$ and the thickness dependence $t$ are presented. In addition, the influences of low temperature and high magnetic fields are analysed. To precisely study the transport properties, a characterization device with a 2-step lithography process is developed (see figure 5.2). Due to the low depo-

---

[5]With $l_e=40\,nm$ and $p=0.1$ as for the conductivity calculations.

sition temperature (80 °C), a pre-patterning step prior to the deposition benefits the structuring of the ALD layer before the contact matrix is patterned. This leads to fixed geometries and well designable ALD and contact structures (see figure 5.1).

Using the PPMS systems *Versalab* and *Dynacool* (both *QuatumDesign*), their inter-

| $t$ | $\sigma^{50\,K}$ | $\sigma^{300\,K}$ | $S^{100\,K}$ | $S^{300\,K}$ | $R_H^{50\,K}$ | $R_H^{300\,K}$ |
|---|---|---|---|---|---|---|
| [nm] | [S/m] | | [µV/K] | | [m$^3$/C] | |
| 160 | – | $3.20 \cdot 10^4$ | 80 | 157 | $1.37 \cdot 10^{-6}$ | $1.87 \cdot 10^{-6}$ |
| 96 | $3.28 \cdot 10^4$ | $2.54 \cdot 10^4$ | 65 | 145 | $5.40 \cdot 10^{-7}$ | $7.51 \cdot 10^{-7}$ |
| 72 | $2.22 \cdot 10^4$ | $1.81 \cdot 10^4$ | 62 | 140 | $1.11 \cdot 10^{-6}$ | $1.27 \cdot 10^{-6}$ |
| 48 | $4.35 \cdot 10^4$ | $3.21 \cdot 10^4$ | 56 | 131 | $4.04 \cdot 10^{-7}$ | $4.70 \cdot 10^{-7}$ |
| 32 | $4.97 \cdot 10^4$ | $4.15 \cdot 10^4$ | 42 | 121 | $3.13 \cdot 10^{-7}$ | $3.83 \cdot 10^{-7}$ |

**Table 6.1:** Overview of $\sigma$ and $R_{Hall}$ at 50 and 300 K, and $S$ at 100 and 300 K for different thin film thickness.

nal lock in amplifier (resistance measurements) and the external DC measurement equipment (heater and thermovoltage) (see figure 5.6), the electrical conductivity $\sigma$, the Hall coefficient $R_H$ (between 2-400 K) and the Seebeck coefficient $S$ (between 50-400 K) are measured. The thin film thickness $t$ is variate between 32 nm and 160 nm. The temperature dependent conductivity is decreases from 10-400 K which is a signature of a strong degenerated semiconductor. The relatively weak temperature dependence ($\sigma_{max}(T)/\sigma(T{=}300\,K){=}120\text{-}140\,\%$) is probably a result of the dominating grain size and/or surface scattering, highlighting the polycrystallinty of the ALD thin films due to the Volmer Weber like growth [61, 64, 154]. The Seebeck coefficient is proportional to $\ln(T)$ up to $T \approx 325\,K$ (see figure 6.5) indicating a constant carrier concentration and therefore the extrinsic regime of the $Sb_2Te_3$ thin films [6]. The Hall coefficient $R_H$ increases with increasing temperature to about 325 K, consistent with the peak of the Seebeck coefficient at the same temperature for all thicknesses investigated. However, the increasing $R_H$ with $T$ leads, within a simple one band model, to a paradoxical decrease of the Hall carrier concentration $n_{Hall}$. This behaviour has been related with either a change in the Hall scattering factor $r_H$ due to a change in the dominating scattering factor, or as a signature of a second band contributing to the charge transport, with different carrier concentration $n$ and mobility $\mu$ temperature dependencies [97, 109]. However, calculating $n_{Hall}$ with a simplified on band model, the evaluated carrier density is reduced compared to other thin film deposition methods, which we take as a sign of the suppressed defect formation due to the low deposition temperature of ALD [97].

To check further indications of such second transport channel, the (high) magnetic field and low temperature dependencies of the longitudinal and transversal magneto resistances (LMR: $R_{xx}$ and TMR: $R_{xy}$ respectively) have been analysed.Indeed, a

parabolic field dependency of ($R_{xx}B^2$) as well as a derivation in the linear field dependence of $R_{xy}$ at high magnetic fields ($B > \pm 2\,\text{T}$) was been found as signatures of two band conduction [105, 119–121, 128, 129]. At low temperatures ($T < 10\,\text{K}$), the LMR ($R_{xx}$) shows a symmetrical sharp dip as a function of low magnetic fields ($B < \pm 1\,\text{T}$) (see figure 6.10 (b)), which shape and field dependence is characteristic for the weak anti-localisation WAL effect, that occurs in 2-dimensional systems with strong spin orbit coupling [124, 134]. However, similar amplitude and field dependencies are expected for 2D conductive helical surface states, as known for topological insulators (TI), a phase of matter what has been experimentally validated in several chalcogenide V$_2$VI$_3$ compounds [65, 124, 125, 135–137].

We proofed the existence of a 2D conduction channel in the transport properties of
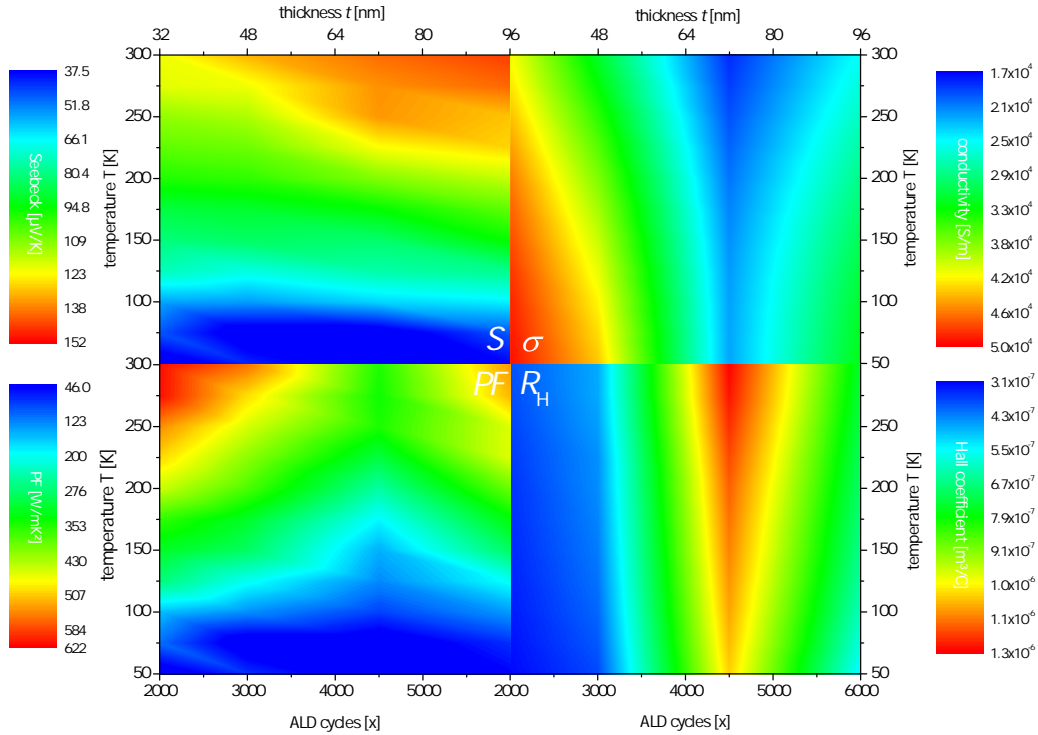


**Figure 6.17:** Combined picture of the transport properties, $S$, $\sigma$, $PF$ and $R_\text{H}$ as a function of temperature $T$ and film thickness $t$ or ALD cycles x respectively.

ALD grown Sb$_2$Te$_3$ by the thickness dependent measurements of $\sigma$, $S$ and $R_\text{H}$ at a fix temperature ($T = 300\,\text{K}$). The conductivity $\sigma$ is found to split up in two regimes (see figure 6.12 (b)): (1); the upper conductivity regime $t \geqslant 72\,\text{nm}$ (**UCR**), where $\sigma$ decreases inverse hyperbolic with decreasing thickness and (2); the lower conductivity regime $t < 72\,\text{nm}$ (**LCR**), in which the conductivity increases linearly with decreasing thickness. We developed a model which combines the effect of increasing surface scattering according to the Fuchs-Sondheimer equation for bulk thin films (see equa-

tion 3.6) and the effect of a 2D conduction channel contributing parallel to the conduction. The calculations based on that model reasonable describes the thickness dependence of the relative change of $\sigma$ with $t$ in both regimes, using a mean free path of $l_e = 40$ nm corresponding to the grain size found by XRD analysis [61,67,68,147,154]. The model employed has been expanded to the thickness dependence of $S$ and $R_H$ by substituting the necessary parameters with the conductivities $\sigma_{3D}$ and $\sigma_{2D}$. Approximating $S_{2D} < S_{3D}$ and $n_{2D} < n_{3D} \cdot t$, as it has been found by theoretical and experimental evaluations, and using the same $\sigma$-descriptions for all calculations, the qualitative t-evolution of all measured values can be well described, highlighting the consistence of the model in the case of ALD grown $Sb_2Te_3$ thin films [27,128].

It has turned out, that quite similar consideration of the thickness dependence in $Bi_{1-x}Sb_x$ thin films as well as the analysis of an increasing Hall coefficient with increasing temperature on flash-evaporated $(Bi_{1-x}Sb_x)_2Te_3$ films have been done by F. Völklein and E. Kessler in 1986 and U. Dillner and F. Völklein 1990 respectively [155,156]. In fact, F. Völklein and E. Kessler have observed a decreasing electrical conductivity with decreasing thickness over range of 400-20 nm in the $Bi_{1-x}Sb_x$ thin films. They were able to quantitative describe the thickness dependence of $\sigma$, using a combined model, including the influence of surface scattering (FS-model) and grain size growth with increasing thickness (MS-model). The decrease of the Seebeck coefficient to smaller $t$ was observed to be comparably weak. Additionally they observed a higher conductivity of the thinnest samples at 80 K, which was referred as an result of the increasing influence of the surface carrier concentration $n_S =_{2D} /t$ at to smaller $t$ [155]. Although $Bi(1-x)Sb_x$ crystal structure, band gap, effective masses and the electron mean free paths are of course different, the general consideration and assumption made in this work are transferable to $Sb_2Te_3$ thin films and can bee found to bee quite similar.

U. Dillner and F. Völklein have evaluated the temperature dependence of the electronic transport properties in flash-evaporated thermoelectrically optimized $(Bi_{1-x}Sb_x)_2Te_3$ films by assuming either a change of the density-of-state effective mass $m_{dF}$, a change of the scattering factor $r$ or both with temperature [156]. The calculations made assuming such changes were found to influence e.g. the Hall coefficient in a way, that $_H$ increases with increasing temperature, without the a change in the charge carrier concentration. This facts are in good agreement with the results found for the temperature dependencies of the ALD $Sb_2Te_3$ thin films [97].

However the calculations and measurements of both publications are in qualitative good agreement with the the results of the ALD $Sb_2Te_3$ thin films in this work, there are several parameters unknown which can influence the transport properties. Possible changes of e.g., the stoichiometry (defect content), the qualitative grain growth

and the surface roughness as a function of thin film thickness $t$ can not be ruled out to further affect $\sigma$, $S$ and $R_{\mathrm{H}}$. Additionally, the dependence of the anisotropy of the transport coefficient, the non parabolic many-valley two-valence-band structure of Sb$_2$Te$_3$ and the energy dependence of the different charge carrier scattering times $\tau_i$ can play a role in the electronic transport. The calculations presented in this work are limited to the parabolic one-band-model with energy independent scattering time approximation. Furthermore, the temperature dependence of the conductivity with respect to the thickness found in this work do not show a linear decreasing slope in $T$ with decreasing film thickness, as it is expected and observed if the surface states become more dominant with decreasing $t$ [155], indicating that the thickness and temperature dependence of $n_{\mathrm{3D}}$, $n_{\mathrm{2D}}$, $\mu_{\mathrm{3D}}$ and $\mu_{\mathrm{2D}}$ may change due to one of the influences above, or to an unknown coupling of both conduction channels.

# Chapter 7

# Synthesis and transport properties of ALD coated $Bi_2Te_3$ particles

In this chapter, the synthesis and the transport property measurement results of the ALD coated particles are discussed. All coating is done by the self developed particle reactor. The new developed flow-through modus of the chamber, where the precursor gas is pulled through the particles, is designed to increase the reactivity between the precursor gas and the particle surface. This is the first time this concept and the machine itself is tested.

In contrast to the thin film synthesis, a compacting step prior to the thermoelectric measurements is necessary, since we are interested in the transport properties of the "bulk" material. All particle charges where produced with a mortar, using commercially available $Bi_2Te_3$ powder with purity of 99.99 % (*INTATRADE Chemicals GmbH*), and are split up into two parts. One half is compacted without coating, while the other is part is coated with the respective number of ALD cycles. As mentioned in chapter 4 the growth rate of $Al_2O_3$ on the $Bi_2Te_3$ is reduced compared to the results found on $Si/SiO_2$. The compacting step (see figure 7.1) is done by "Direct Hot Press-

| number of ALD cycles | $t$ on $Si/SiO_2$ [Å] | $t$ on $Bi_2Te_3$ particles [Å] |
|:---:|:---:|:---:|
| 10 | 15 | 2.5-5 |
| 25 | 37.5 | 6.25-12.5 |
| 50 | 75 | 12.5-25 |
| 200 | 300 | 50-100 |

**Table 7.1:** Film thickness of different numbers of $Al_2O_3$ ALD cycles on $Si/SiO_2$ substrates found by ellipsometry (see figure 4.15) and on $Bi_2Te_3$ particles estimated via TEM results (see figure 4.18).

ing" (DHP[1]), using a DSP 510 (*Dr. Fritsch*) at a temperature of 320 °C. In contrast to the "Spark Plasma Sintering" (SPS), no pulsed current is used to heat up the powder but a constant DC current [157, 158]. Therefore a typical amount of 2-3 g of powder
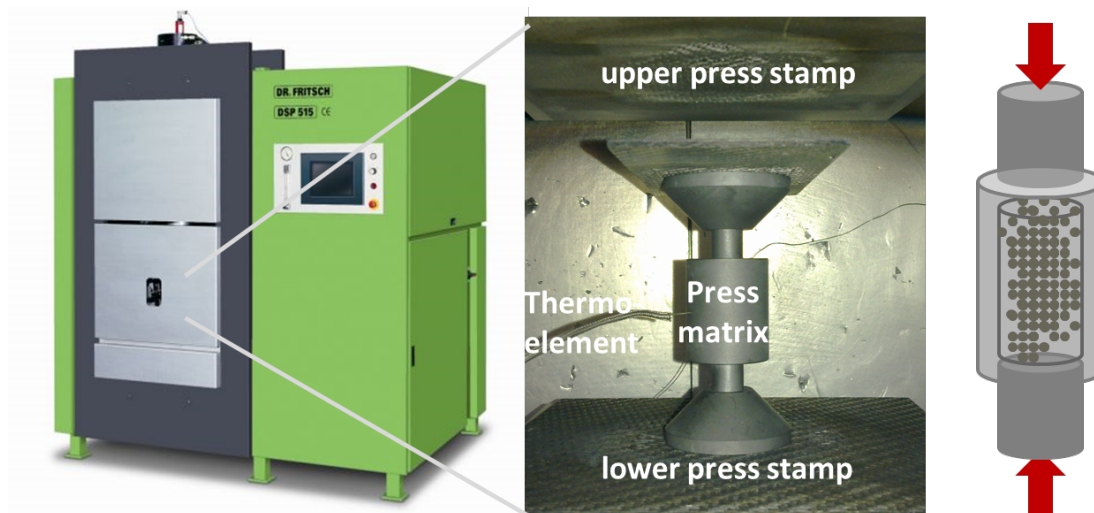


**Figure 7.1:** Sintering Press DSP 510 (*Dr. Fritsch*) and the inner view of the graphite press matrix with the thermoelement.

is loaded in the graphite press matrix. The powder is enclose by two graphite press stamps on each side and pre-compacted by using a hand press. The sintering machine heats up the powder by applying a DC current through the sample while a pressure of 2.5 MPa is applied between the two stamps (see figure 7.1). The chamber is evacuated and a linear heating ramp of 5 min from 25 °C to 320 °C, 5 min holding time and 5 min of cooling time is used. A dice of 12 mm in diameter and around 5-10 mm in height is formed, which density is evaluated with an Archimedes scale and can be found to be close to the theoretical bulk density (7.64 - 7.70 g · cm$^{-3}$) for both, the reference and the coated samples.

## 7.1 Transport properties of Al$_2$O$_3$-Bi$_2$Te$_3$ core shell particles

After the sintering step, the dices are cut into rectangular bars with a height of around 10 mm and width and depth of around 5 mm, using a diamond saw. This is necessary, since the measurement system used, a LSR-3 (*Linseis - Thermal Analysis*), needs at least 10 mm in height for the conductivity measurements. The measurements are performed between 55 °C and 255 °C with a step width of around 25 °C during heating and cooling. For the conductivity measurements a DC-current of 100 mA is applied

---

[1]Also known as "Rapid Hot Pressing" (RHP) or "FAST Direct Hot Pressing"' (FAST DHP)

| sample | reference density [$g \cdot cm^{-3}$] | $Al_2O_3$ cycles | coated density [$g \cdot cm^{-3}$] |
|--------|--------------------------------------|------------------|------------------------------------|
| 11 | 7.60 | 10 | 7.53 |
| 10 | 7.59 | 10 | 7.47 |
| 13 | 7.63 | 25 | 7.51 |
| 12 | 7.56 [$T = 250\,°C$] | 25 | 7.60 |
| 08 | 7.56 | 50 | 7.55 |
| 05 | 7.60 | 50 | 7.58 |
| 02 | - | 200 | 7.51 |
| average | 7.60 | - | 7.53 |

**Table 7.2:** Density of coated and uncoated particle after sintering. All particles are sintered at 320 °C, except reference sample 12. For the 200 ALD cycle step, no reference sample is available. The theoretical density is about 7.64-7.70 $g \cdot cm^{-3}$.

between the electrodes. The voltage drop is measured between the thermocouples which contacts the sample with a distance between both of around 3.5 mm. For Seebeck measurements a temperature gradient of around 20 °C is applied by a gradient heater at bottom electrode, resulting in a temperature difference between both voltage contacts of about 2-3 K. The temperature difference is evaluated with two S-type (Pt/Rh 90 %/10 %) thermocouples and the thermovoltage is evaluated from the voltage difference of the thermocouples (corrected with the temperature-voltage dependence of the S-type thermocouples arising from the temperature difference).

### 7.1.1 Electrical conductivity of $Al_2O_3$-$Bi_2Te_3$ core shell particles

The temperature dependence of the conductivity of the average reference $\sigma_{ref}$ and the ALD coated $\sigma_{coa}$ samples are shown in figure 7.2 (a) and (b) respectively. The reference sample values $\sigma_{ref}$ for 10 and 50 cycles are averaged over two samples, while the reference for 25 ALD cycles is a single sample. The reference of sample 200 is the average of all reference samples since no reference sample was available in this charge. For the conductivity $\sigma_{coa}$ of the coated samples, the values of 10, 25, and 50 cycles are averaged - for 200 cycle only one sample is available. Both, the reference and the coated samples show similar temperature dependence, indicating that the stoichiometry is not influenced by the $Al_2O_3$ coating. At around 120 °C all samples show a minimum in the conductivity, as a signature of the transition form degenerate to non-degenerate statistics [159]. Since this minimum does not shift with increasing thickness of the $Al_2O_3$ shell, the relation between the extrinsic and the intrinsic conductivity seems not to change, if we assume that the parallel two channel conduction approximation is valid [42]. The absolute values are in good agreement with the results for $Bi_2Te_3$
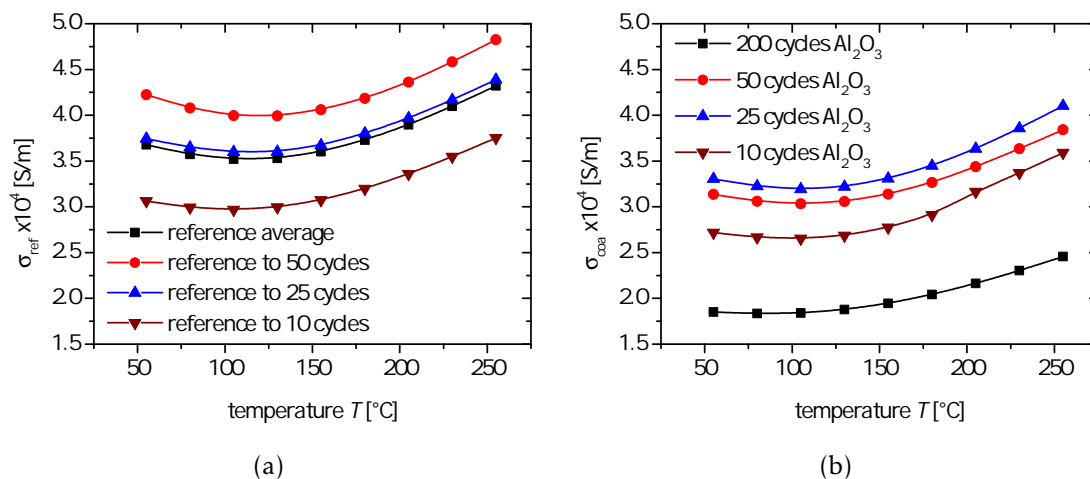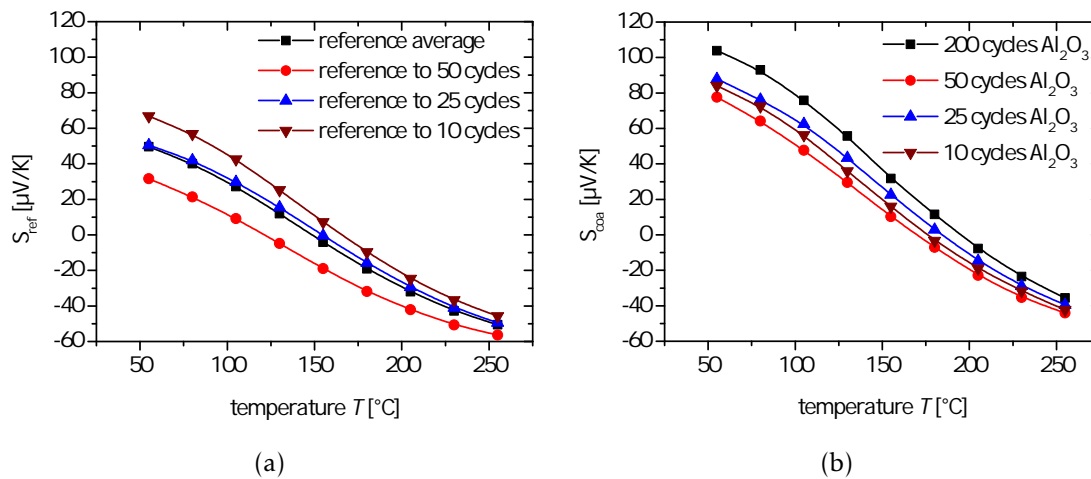
**Figure 7.2:** Temperature dependence of the conductivity of the coated (b) and the corresponding reference samples (a). Some of the values are averaged (see text).

bulk samples in other works, see i.g. [28, 34, 160].

To evaluate the influence of the ALD coating, the electrical conductivity of the reference $\sigma_{ref}$ and the coated samples $\sigma_{coa}$ are compared with each other at 55 °C. In figure 7.3 (a) and (b) the absolute values of both conductivities are shown as a function of $Al_2O_3$ ALD cycles (reference to the corresponding sample, respectively). $\sigma_{ref}$ variates between about 2.7 and $4.2 \cdot 10^4$ S/m indicating fluctuations in stoichiometry, amount of foreign elements and/or a grain size distribution of the initial $Bi_2Te_3$ powder, since the electronic properties of $Bi_2Te_3$ are very sensitive to small differences in the Te/Bi ratio [34]. The differences in the conductivities between coated and uncoated samples (see figure 7.3 (c)) of $\sigma_{coa}$-$\sigma_{ref}$ exhibit, that the reduction is a function of the $Al_2O_3$ shell thickness.

### 7.1.2 Seebeck coefficient of $Al_2O_3$-$Bi_2Te_3$ core shell particles

In the temperature dependence of the Seebeck coefficients (see figure 7.4 (a) and (b)) the transition from the extrinsic to the intrinsic behaviour is more pronounced in comparison to the conductivity. The Seebeck coefficients have been average in the same way as it has been done for the conductivity values. At 55 °C the Seebeck coefficient is positive for all samples, but comparably low to thermoelectric optimized $Bi_2Te_3$ material [34]. The absolute Seebeck coefficients of the reference samples $S_{ref}$ variate between 30-70 μV/K at 55 °C indicating the presence of a p-type dopant foreign element in the initial powder, since the values of hot pressed $Bi_2Te_3$ particles are generally found to be around ~-150 μV/K at this temperature [53, 160]. The linear link between Seebeck coefficient and electrical resistivity (see figure 9.6 in the appendix)
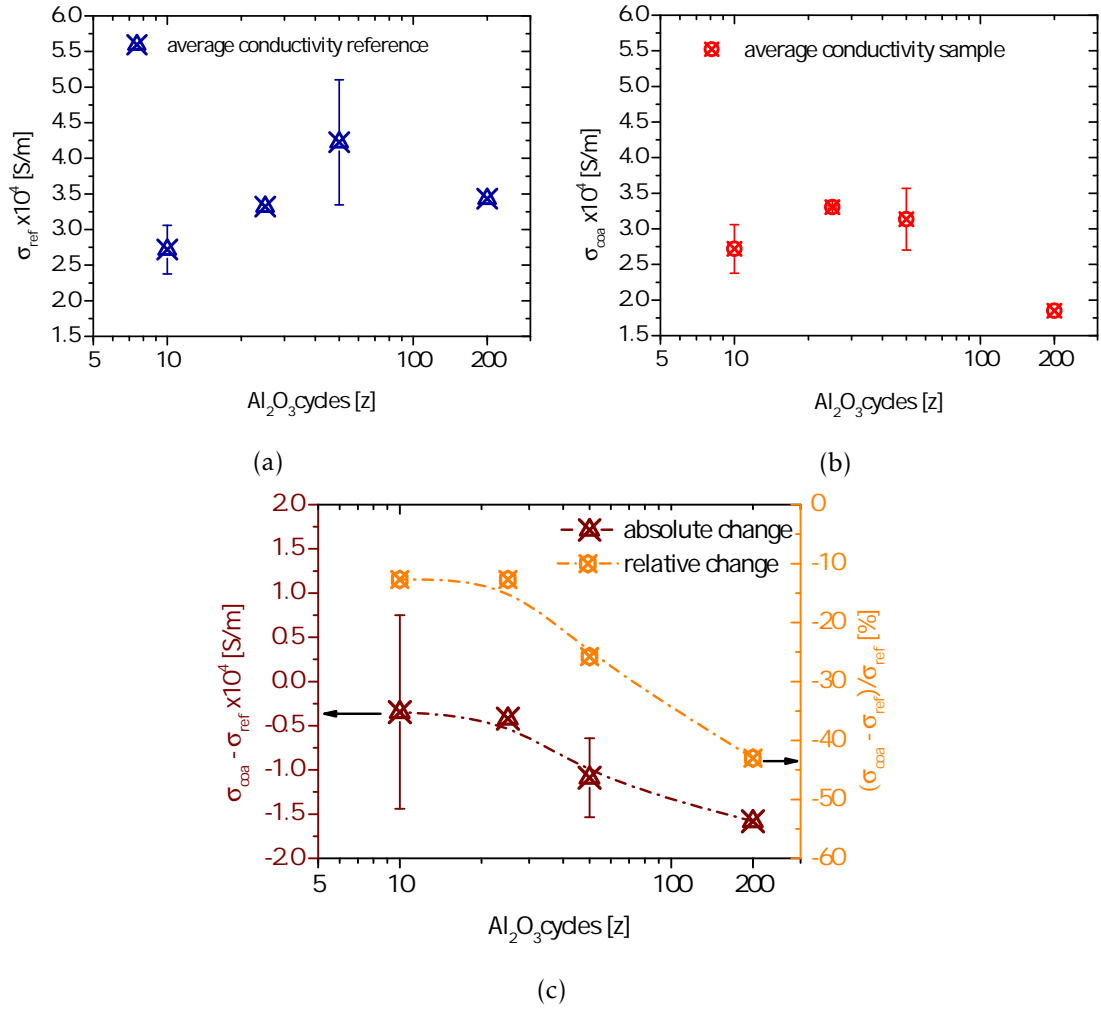
**Figure 7.3:** (a) and (b): Average conductivity of $\sigma_{ref}$ and $\sigma_{coa}$ as a function of Al$_2$O$_3$ ALD cycles at 55 °C. (c): The absolute and relative changes with respect to the Al$_2$O$_3$ shell. Note that the x-axis of $\sigma_{mathrmref}$ is in reference to the corresponding coated samples.

supports this estimation, since small variations in the dopant content should decrease both values in this regime. The differences in the Seebeck coefficient of the coated sample $S_{coa}$ is smaller (between around 80-100 μV/K at 55 °C) compared to $S_{ref}$. With increasing temperature both, the Seebeck coefficients of the reference $S_{ref}$ and the coated samples $S_{coa}$, crosses the zero line, switching from p- to n-type behaviour but in different temperature regimes. For $S_{ref}$ this regime is between 120 °C$\leqslant T \leqslant$ 170 °C, while $S_{coa}$ crosses the zero Seebeck line between 170 °C$\leqslant T \leqslant$ 200 °C. In contrast to conductivity, where the minimum is found to be similar for the coated and uncoated samples, the Al$_2$O$_3$ shell seems to influence the contribution of the p- and n-type Seebeck coefficients. However, temperature dependence of $S_{ref}$ and $S_{coa}$ is quite similar and $S_{coa}$ approximates $S_{ref}$ with increasing temperature, indicating similar intrinsic

**Figure 7.4:** Temperature dependence of the Seebeck coefficient of the coated (b) and the corresponding reference samples (a). Some of the values are averaged (see text).

behaviour [159]. This is expected if the $Al_2O_3$ shell does not change the stoichiometry of the particle $Bi_2Te_3$ which is in good agreement with the results of the electrical conductivity. Thus the effect of ALD coating seems to be different compared to the change of the transport properties in the case of classical doping, where the carrier concentration is optimised by adding a certain amount of ad-atoms. The change of the Seebeck coefficient of the ALD coated particles is more likely due to a change of the carrier mobility [34]. However, the influence of the $Al_2O_3$ shell thickness on the Seebeck coefficient (see figure 7.5 (c)) is much stronger compared to the difference in the conductivity (see figure 7.3 (c)). The relative difference of $\sigma_{coa}$-$\sigma_{ref}$ is more the 100 % if the ALD cycle number is larger than 50.

### 7.1.3  Thermal conductivity of $Al_2O_3$-$Bi_2Te_3$ core shell particles

The thermal conductivity $\kappa$ of the $Al_2O_3$ ALD coated particles is determined by the heat diffusivity $\lambda$, the density $\rho$ and the specific heat capacity $C$

$$\kappa = \lambda \cdot \rho \cdot C. \tag{7.1}$$

The heat diffusivity has been measured by laser flash analysis (LFA)[2], while the density is evaluated with a Archimedes scale (see table 7.2 for both, the ALD coated and the uncoated reference samples. For the evaluation of $\kappa$ a maximum capacity $C$, given by the Dulong-Petit-law[3], is used. The total thermal conductivity of the reference

---

[2]Thanks to DLR-team (Christian Stiewe), using a LFA 300 *Netsch*.

[3]Using a molar heat capacity of $Bi_2Te_3$ of $C_{mol} = 3\dot{N} \cdot 25$ J/(mol K) and a molar mass of $Bi_2Te_3$ of 800 g/mol.

(a)

(b)

(c)
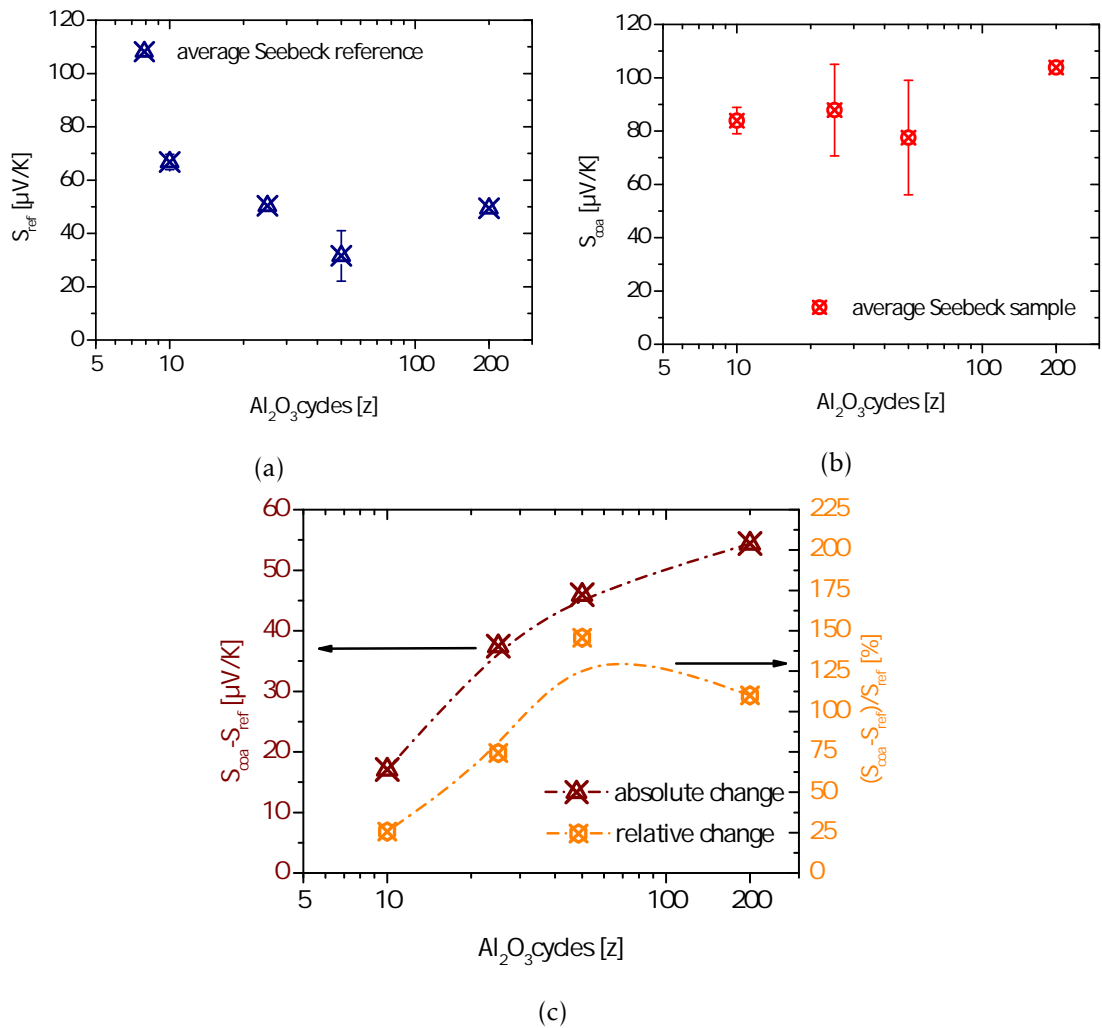
**Figure 7.5:** (a) and (b): Average Seebeck coefficient of $\sigma_{\text{ref}}$ and $\sigma_{\text{coa}}$ as a function of Al$_2$O$_3$ ALD cycles at 55 °C. (c): The absolute and relative changes with respect to the Al$_2$O$_3$ shell.

$\kappa_{\text{ref}}$ and the coated $\kappa_{\text{coa}}$ samples are shown in figure 7.6 as a function of temperature. All samples show a linear increasing trend with increasing temperature, from around 1.0 W/(m·K) at 50 °C to $\approx$1.5 W/(m·K) at 250 °C, which is in good agreement with the results for hot pressed grained Bi$_2$Te$_3$ with similar densities, produced via hot pressing [160]. The thermal conductivity of the reference samples $\kappa_{\text{ref}}$ is found to be similar for all samples and is not influenced of the fluctuations in the electrical conductivity $\sigma_{\text{ref}}$ (see figure 7.3 (a)). Sumithra *et al.* have distinguished between lattice $\kappa_l$ and electronic part $\kappa_e$ of the thermal conductivity for hot-pressed Bi$_2$Te$_3$ by using the Wiedemann-Franz law in their work [160]. However, one has to be careful using this approximation in semiconducting materials. Although the Wiedemann-Franz law is valid for metals and highly degenerated semiconductors in the extrinsic regime, in
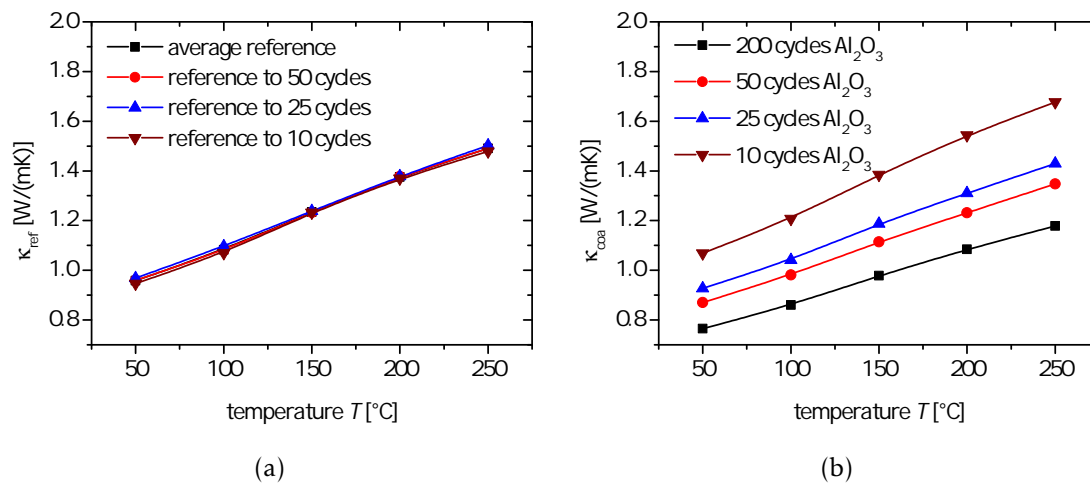
**Figure 7.6:** Thermal conductivity of reference and ALD coated $Bi_2Te_3$ particles.

the case of intrinsic electron-hole conduction contributing to the electronic transport, using the metallic Lorenz value[4] $L_0$ to calculate the $\kappa_e$ is not longer a good approximation [161]. For intrinsic conduction, the Fermi-level position of a semiconductor is located in the band gap and the Seebeck coefficients are reduced due to the bipolar diffusion, leading to an enhanced contribution of the electronic part to the thermal conductivity [161]. Since the Seebeck coefficient as well as the electrical conductivity strongly indicate an intrinsic behaviour, the Lorenz factor $L$ for our material system is unknown and probably differs from the metallic $L_0$. Therefore the separation between lattice and electrical thermal conductivity is not possible.

The total thermal conductivity $\kappa$ of the coated particles with an ALD cycle number of larger than 25, is found to be reduced compared to their reference counterpart (see figure 7.7 (c)). However, we cannot provide evidence, if the reduction of $\kappa$ as a function of ALD $Al_2O_3$ cycle number is only due to the reduced electrical conductivity, or if the lattice thermal conductivity $\kappa_l$ is effected by the ALD coating, too. Although the average phonon mean free path is expected to be very small (around a few nm), the low frequency and long mean free path phonons can contribute significantly to the heat transport [162]. Since the size distribution of the initial $Bi_2Te_3$ particles is probably wide, meaning the existence of interlayers in different length scales, a reduction of the lattice thermal conductivity can not be ruled out.

---

[4]Lorenz number $L_0$ can be found to be $\approx 2.45 \cdot 10^{-8}\,\mathrm{W\Omega K^{-2}}$.

---

**Figure 7.7:** (a) and (b) thermal conductivity $\kappa_{ref}$ and $\kappa_{coa}$ as a function of $Al_2O_3$ ALD cycles at 50 °C. (c): The absolute and relative changes with respect to the $Al_2O_3$ shell.

## 7.2 Conclusions of the transport properties of core shell particles

Although the used initial, commercial available, $Bi_2Te_3$ powder is not optimized for thermoelectric applications, the results can bee seen as a general case study of the influence of $Al_2O_3$ ALD coating. As expected, the electrical conductivity is decreasing as function of the (insulating) shell thickness. In contrast to classical doping, this is probably not a result of a change in the carrier concentration, since the temperature at which the minimum in the conductivity is observable is not changing with increasing $Al_2O_3$ amount.

The temperature dependence of the Seebeck coefficient of the reference samples $S_{ref}(T)$

is lower compared to those of the coated samples $S_{coa}(T)$. Starting from a value of about $S_{coa} \sim 90\,\mu V/K$ at 55 °C is approximating the value of $\sim$-50 $\mu V/K$ of $S_{ref}$(T=255 °C), as a consequence of the transition from extrinsic to intrinsic behaviour. This indicates again, that the stoichiometry of the initial powder has not been influenced by the ALD coating.

In figure 7.8 (a) and (b) the calculated figure of merit of the reference $ZT_{ref}$ and coated



(a)

(b)

(c)
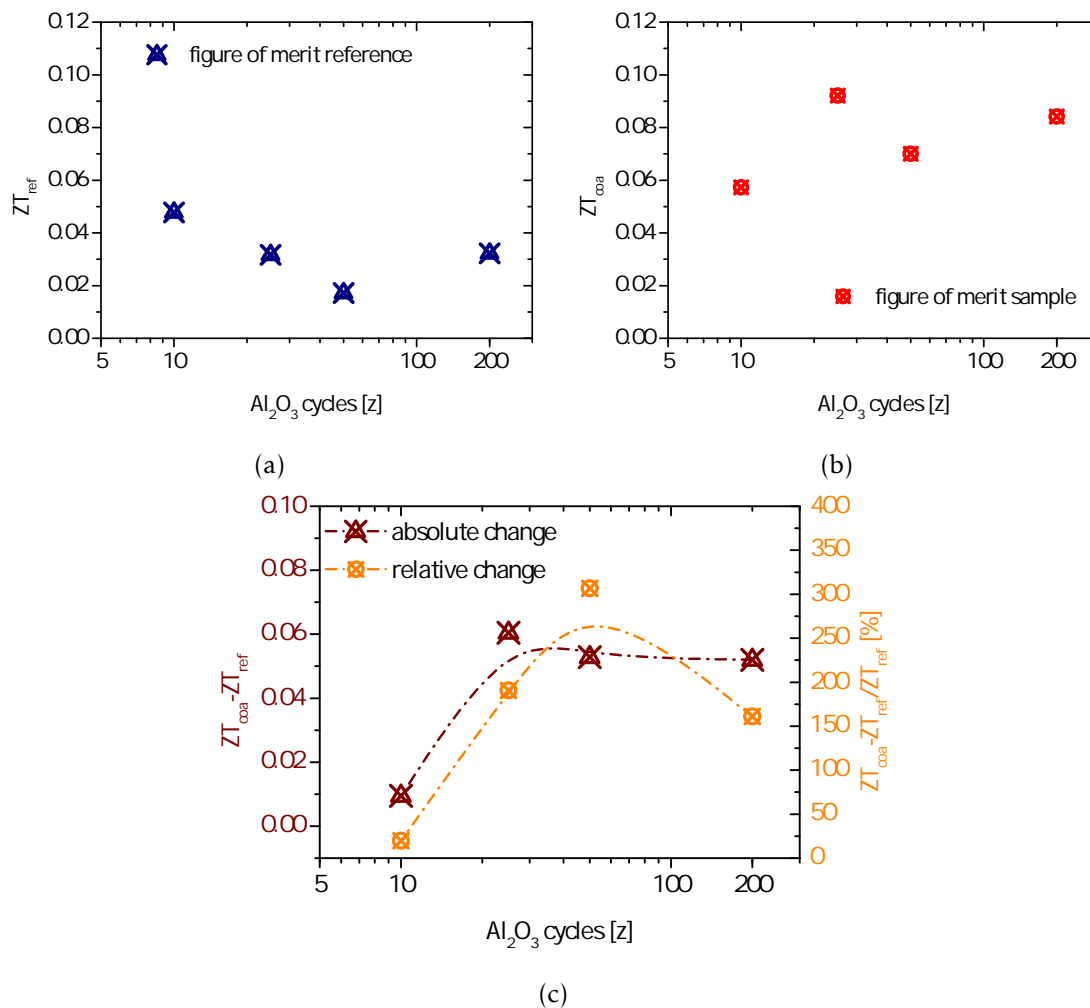
**Figure 7.8:** (a) and (b) Figure of merit of the reference $ZT_{ref}$ and coated samples $ZT_{coa}$ with respect to the number of $Al_2O_3$ ALD cycles. (c) absolute and relative change of $ZT$ as a function of $Al_2O_3$ ALD cycles. The corresponding temperature is $T = 50\,°C$ (see text).

$ZT_{coa}$ samples are shown. The values have been evaluated with

$$ZT = \frac{S_{\perp}^2(T = 55°C) \cdot \sigma_{\perp}(T = 55°C)}{\kappa_{\|}(T = 50°C)} \cdot 50°C,$$ 
(7.2)

where the $\perp$ symbols mark the values measured cross plane, and $\parallel$ mark the values which are measured in plane to the pressing direction. Since the lowest temperature where values of $S$ and $\sigma$ are available is 55 °C, the thermal conductivities of $\kappa(T = 50\,\text{K})$ have been used. Due to the decreasing trend of $S$ and $\sigma$ and the increasing $\kappa$ with $T$ in this temperature regime, the calculated $ZT$'s are fairly underestimated.

As well as the Seebeck coefficient and the electrical conductivity of the reference samples, the $ZT$ values variate between $0.015 - 0.05$ at $T = 50$ °C as a function of the corresponding sample ALD cycles (see figure 7.8 (a)). The absolute values are comparably low, since the initial $Bi_2Te_3$ powder was not optimized in terms of the best thermoelectric performance. The coated samples show an enhanced figure of merit compared to the corresponding reference sample of values between $0.06 - 0.09$ (see figure 7.8 (b)). In figure 7.8 (c) the absolute and relative changes of $ZT_{\text{coa}}$ with respect to $ZT_{\text{ref}}$ are plotted as a function of the ALD $Bi_2Te_3$ shell thickness. Although the thermal conductivity is found to be lower in the coated samples, the largest contribution of the enhancement of $ZT$ at this temperature is obviously due to the increased Seebeck coefficient.

However the $ZT$ factor of the coated samples (see figure 7.8) is found to be increased in contrast to the reference samples at around 50-100 °C, the $ZT$ factor of both lowers to higher temperature due to the suppressed Seebeck coefficient caused by the bipolar conduction of the intrinsic $Bi_2Te_3$.

# Chapter 8

# Summary and Outlook

Only a very limited number of publications on ALD grown nanostructures of thermo-electric materials and even less on thermoelectric properties of ALD grown thin films are available[1] (see e.g. [64, 96, 163, 164]). However, the publications of thermoelec-tric properties of nanostructured materials is still very high. In this work we present for the first time electronic thermoelectric measurements of ALD grown $Sb_2Te_3$ thin films as well as the thermoelectric properties of surface modified $Bi_2Te_3$ particles by ALD, sintered via SPS. This surface modified particles have been synthesized by a new designed particle flow-through/exposure reactor, enabling the conformal coating via constant rotation of the reaction chamber.

The depositions for the thin film analysis have been made with a home-made exposure-reactor with an additional precursor-boost to lower the growth temperature to $80\,°C$. Structural and compositional analysis have been performed using SEM, XRD, EDX and PIXE. The SEM results show a Volmer-Weber like growth behaviour of the $Sb_2Te_3$ with non closed islands up to thickness of about $t < 32\,nm$ and random orientated hexagonal plates due to the hexagonal crystal structure of $Sb_2Te_3$. In the XRD pattern the preferential growth direction was found to be along the c-axis, while the grain size analysis using the Sherrer equation leads to an average grain size of about $40\,nm$ (for an about $40\,nm$ thick film). Both results highlighting the polycrystallinity of the ALD films. EDX and PIXIE confirm the estimation of a good stoichiometry due to low temperature chemical process, with results, within the error, of nearly ideal 2:3 Sb to Te atomic ratio.

The electronic thermoelectric properties $\sigma$, $S$ and $R_H$ of the thin films have been mea-sured with a self developed measurement device, patterning the ALD film and the contact mask via a 2-step photolithography process [97]. This enables the temperature dependent measurement of all properties of a single film using a commercial available

---

[1]Web of science™search conditions: TITLE: Thermoelectric AND Atomic Layer Deposition.

cryostat system in combination with an external DC measurement setup. Different film thicknesses between $32 \leqslant t \leqslant 160\,\text{nm}$ have been analysed with respect to their temperature, magnetic field and thickness dependence. The ALD grown $Sb_2Te_3$ films show a degenerated semiconducting characteristic, with a peak of the Seebeck coefficient $S$ at around 325 K corresponding to the increasing intrinsic carrier concentration observable in the Hall coefficient $R_H$ at the same temperature. However, $R_H$ shows an untypical decreasing trend with decreasing temperature below 325 K, which have been correlated with either, a change of the Hall scattering factor $r_H$ due to a change of the dominant scattering mechanism [97, 156], or the existence of a second band contributing to electronic transport [109]. Therefore the films have been studied under the influence of high magnetic fields and low temperatures. It has turned out that the magnetic field dependent resistances ($R_{xx}$ and $R_{xy}$) show signatures of a second band. Additionally, the low temperature and low magnetic field dependence of the LMR $R_{xx}(B)$ show a characteristic sharp dip. This feature has been correlated with the weak anti-localisation effect (WAL), that occurs in 2-dimensional (2D) systems with spin-orbit coupling, but which is also expected to show up in 2D conductive helical surface states, called topological insulators (TI).

A 2-band transport model has been developed to proof if a 2D transport channel significantly contributes to the thickness dependent transport properties $\sigma$, $S$ and $R_H$. The influence of the classical size effect of surface scattering has to be taken into account, since an decrease of the conductivity with decreasing thickness was found for $t \geqslant 72\,\text{nm}$ (UCR), as it has been observed previously in $Sb_2Te_3$ and $Bi_{1-x}Sb_x$ thin films [61, 155]. However the trend was found to be similar, with further decreasing thickness ($t < 72\,\text{nm}$), the conductivity rises again, which has been attributed as the contribution of the 2D channel. In consistence with the conductivity evaluation, the qualitative thickness dependence of both, Seebeck and Hall coefficient have been evaluated. All measured transport properties show a reasonable good agreement with the calculated behaviour. However, there are further parameters which are a function of thickness and influence the electronic transport. The growing grain size with increasing thickness probably changes the in plane mobility of the charge carriers with $t$. Eventually the stoichiometry slightly changes with thickness, since the diffusion length is increased with dwell time in the reactor.

In this work we have presented the advantages of combining thermoelectrics, nanostructuring and ALD for: (1) general and systematically studies of high purity thin film materials, (2) creating core shell nanostructures and (3) the proof of principle of the up-scaling ability of this method for creating bulk material of ALD coated particles with enhanced thermoelectric performances. A systematic study of other materials with interesting thermoelectric properties, e.g. $Bi_2Te_3$ and compounds of

$Bi_2Sb_{2-x}Te_3$, deposited by ALD consequentially follows from the results of the $Sb_2Te_3$ thin film study done in this work. $Bi_2Te_3$ and superlattices of PbTe and PbSe for example have already been produced by ALD but without the evaluation of the electronic and thermoelectric properties [64, 164]. Although the magnetic field and the thickness dependent results show signatures of an additional 2D channels contributing to the transport, further studies of the thermal conductivity and the Nernst coefficient are necessary. Additionally, the influence of the: stoichiometry, grain size, contributing of different conduction channels (3D and 2D) and other effects as a function of the thickness on the electronic transport properties have to be evaluated to get a better understanding of the transport mechanisms in $Sb_2Te_3$ ALD grown thin films.

The case study of particle surface coatings have shown interesting effects on the thermoelectric properties. Although the starting material was not thermoelectrically optimised, the Seebeck coefficient was increased probably without effecting the carrier concentration, since the minimum of the electrical conductivity as a function of temperature was not influenced by the surface coating. However the electrical conductivity is decreased as a function of the $Al_2O_3$ shell, the Power Factor at 55 °C was found to be higher compared to the initial material. The thermal conductivity is found to be decreased as a function of the $Al_2O_3$ ALD cycles as well. Therefore the $ZT$ factor was significantly increased at temperatures of 50-100 °C.

The systematic study of the thermoelectric properties of created core shell structures via ALD coating is just at the beginning. Several patents and publications for synthesising as well as theoretical calculations of such structures to enhance the thermoelectric figure of merit are available [165–168]. Although most of them are on a 1 - 500 nm length scale, and therefore probably in a different size regime, ALD has the advantage of coating large quantities, a wide range of materials/compounds and variable shell thicknesses [21, 24]. Since the initial particle size is tunable, e.g. via ball milling or chemical synthesis methods [169, 170], it should be possible to reproduce such coatings with smaller particle sizes. Prior to the reduction of the particle size, it is necessary to reproduce the results with initial material which thermoelectric properties are optimized, e.g. $Sb_xBi_{2-x}Te_3$ solid solutions. However covering smaller grain sizes with ALD could lead to a grater impact on the thermoelectric properties, it is maybe challenging to prevent the surface of the particles from oxidation before covering with ALD. This can be of vital importance, if semiconducting materials with different band gaps should be deposited, without having an oxide shell reducing the electrical conductivity [53]. Including the reactor into a glove-box would enable a direct transfer of the synthesised particles into the ALD chamber.

Atomic Layer Deposition has been successfully introduced creating different kinds of thermoelectric nanostructures by functionalising the surface of 3D geometries. The

developed flow-through/exposure particle reactor has shown the possibility to transfer such surface coatings even to larger quantities. However, since the parameter-space in material design and surface-functionalisable geometries is large and still not all process parameter dependencies have been evaluated, there are nearly boundless opportunities which can be explored using such processes and reactor designs as presented in this work.

# Danksagung

Wie in einem Orchester entsteht wissenschaftliche Arbeit nur durch das Zusammenspiel viele Akteure. Ein Zahnrad greift in das nächste - fällt nur eines aus, steht alles. Und oft sind es kleine Dinge, deren enorme Beiträge nicht auf den auf den ersten Blick zu erkennen sind, für mich jedoch so oft so entscheidend waren. Für die Unterstützung während meiner Zeit am Institut für Angewandte Physik der Universität Hamburg und für die Mithilfe beim Anfertigen dieser Arbeit danke ich:

# Bibliography

[1] T. J. Seebeck. Ueber die magnetische Polarisation der Metalle und Erze durch Temperaturdifferenz. *Annalen der Physik*, 82(3):253–286, 1826.

[2] J.C.A. Peltier. Nouvelles expériences sur la caloricitfe des courants felectrique. *Annales de Chimie et de Physique*, 56:371Ű386, 1834.

[3] Christophe Goupil, Wolfgang Seifert, Knud Zabrocki, Eckhart Müller, and G. Jeffrey Snyder. Thermodynamics of thermoelectric phenomena and applications. *Entropy*, 13(8):1481–1517, 2011.

[4] G. Magnus. Ueber thermoelektrische ströme. *Poggendorf's Annalen der Physik*, 83:469–504, 1851.

[5] George S. Nolas, Jeffrey Sharp, and H. Julian Goldsmid. *Thermoelectrics: basic principles and new materials developments*. Springer, Berlin [etc.], 2001.

[6] H. Julian Goldsmid. *Introducton to Thermoelectricity*. Springer, 2009.

[7] E. Becquerel. Annales de chimie et de physsique. *Ann. de chim. et phys.*, 4, 1866.

[8] Gilles Dennler, Radoslaw Chmielowski, Stéphane Jacob, Frédéric Capet, Pascal Roussel, Sebastian Zastrow, Kornelius Nielsch, Ingo Opahle, and Georg K. H. Madsen. Are binary copper sulfides/selenides really new and promising thermoelectric materials? *Advanced Energy Materials*, pages n/a–n/a, 2014.

[9] H. Julian Goldsmid. The electrical conductivity and thermoelectric power of bismuth telluride. *Proceedings of the Physical Society*, 71(4):633–646, April 1958.

[10] A. F. Ioffe. *Semiconductor Thermoelements and Thermoelectric Cooling*. Infosearch, 1957.

[11] D. A. Wright. Thermoelectric properties of bismuth telluride and its alloys. *Nature*, 181(4612):834–834, March 1958.

[12] H. J. Goldsmid and R. W. Douglas. The use of semiconductors in thermoelectric refrigeration. *BRITISH JOURNAL OF APPLIED PHYSICS*, 5(NOV):386–390, 1954.

[13] L. D. Hicks and M. Dresselhaus. Effect of quantum-well structures on the thermoelectric figure of merit. *Physical Review B*, 47(19):12727–12731, May 1993.

[14] L. D. Hicks, T. C. Harman, X. Sun, and M. S. Dresselhaus. Experimental study of the effect of quantum-well structures on the thermoelectric figure of merit. *Phys. Rev. B*, 53:R10493–R10496, Apr 1996.

[15] T. C. Harman, P. J. Taylor, D. L. Spears, and M. P. Walsh. Thermoelectric quantum-dot superlattices with high ZT. *Journal of Electronic Materials*, 29(1):L1–L4, 2000.

[16] T. C. Harman, P. J. Taylor, M. P. Walsh, and B. E. LaForge. Quantum dot superlattice thermoelectric materials and devices. *Science*, 297(5590):2229–2232, 2002.

[17] T. Koga, S. B. Cronin, M. S. Dresselhaus, J.L. Liu, and K. L. Wang. Experimental proof-of-principle investigation of enhanced Z(3D)T in (001) oriented Si/Ge superlattices. *Applied Physics Letters*, 77(10):1490–1492, 2000.

[18] R. Venkatasubramanian. MOCVD of $Bi_2Te_3$, $Sb_2Te_3$ and their superlattice structures for thin-film thermoelectric applications. *Journal of Crystal Growth*, 170(1-4):817–821, 1997.

[19] R. Venkatasubramanian, E. Siivola, T. Colpitts, and B. O'Quinn. Thin-film thermoelectric devices with high room-temperature figures of merit. *NATURE*, 413(6856):597–602, OCT 11 2001.

[20] Riikka L. Puurunen. Surface chemistry of atomic layer deposition: A case study for the trimethylaluminum/water process. *Journal of Applied Physics*, 97(12):–, 2005.

[21] Steven M. George. Atomic layer deposition: An overview. *Chemical Reviews*, 110(1):111–131, 2010. PMID: 19947596.

[22] M. Leskelä. Atomic layer deposition (ALD): from prepcursors to thin film structures. *Thin Solid Films*, 409(1):138–146, April 2002.

[23] Gijs Dingemans and WMM Kessels. Status and prospects of al2o3-based surface passivation schemes for silicon solar cells. *Journal of Vacuum Science & Technology A*, 30(4):040802, 2012.

[24] V. Miikkulainen, M. Leskelä, M. Ritala, and R. L. Puurunen. Crystallinity of inorganic films grown by Atomic Layer Deposition: Overview and general trends. *Journal of Applied Physics*, 113(2):021301, 2013.

[25] V. Pore, T. Hatanpää, M. Ritala, and M. Leskelaä. Atomic Layer Deposition of Metal Tellurides and Selenides Using Alkylsilyl Compounds of Tellurium and Selenium. *Journal of the American Chemical Society*, 131(10):3478–3480, March 2009.

[26] V. Pore, K. Knapas, T. Hatanpää, T. Sarnet, M. Kemell, M. Ritala, M. Leskelä, and K. Mizohata. Atomic Layer Deposition of Antimony and its Compounds Using Dechlorosilylation Reactions of Tris(triethylsilyl)antimony. *Chemistry of Materials*, 23(2):247–254, 2011.

[27] F. Rittweger, N. F. Hinsche, P. Zahn, and I. Mertig. Signature of the topological surface state in the thermoelectric properties of $Bi_2Te_3$. *Phys. Rev. B*, 89:035439, Jan 2014.

[28] David Rowe. *Thermoelectrics handbook : macro to nano*. CRC/Taylor & Francis, Boca Raton, 2006.

[29] K. Nielsch, J. Bachmann, J. Kimling, and H. Boettner. Thermoelectric Nanostructures: From Physical Model Systems towards Nanograined Composites. *Advanced Energy Materials*, 1(5):713–731, 2011.

[30] Siegfried Hunklinger. *Festkörperphysik*. Oldenbourg, München; Wien, 2007.

[31] F.D. Rosi, B. Abeles, and R.V. Jensen. Materials for thermoelectric refrigeration. *Journal of Physics and Chemistry of Solids*, 10(23):191 – 200, 1959.

[32] Robert Heikes. *Thermoelectricity: Science and Engineering*. Interscience Publishers, 1961.

[33] H. J Goldsmid. *Electronic refrigeration*. London : Pion, 1986.

[34] David Rowe. *CRC handbook of thermoelectrics*. CRC Press, Boca Raton FL, 1995.

[35] J. S. Dyck, P. Hájek, P. Lošták, and C. Uher. Diluted magnetic semiconductors based on $Sb_{2-x}V_xTe_3$ $(0.0 < x < 0.03)$. *Phys. Rev. B*, 65:115212, Mar 2002.

[36] J. Horák, č. Drašar, R. Novotný, S. Karamazov, and P. Lošťák. Non-stoichiometry of the crystal lattice of antimony telluride. *Physica Status Solidi (a)*, 149(2):549–556, 1995.

[37] X. Zhang, Z. Zeng, C. Shen, Z. Zhang, C. Wang, Z.and Lin, and Z. Hu. Investigation on the electrical transport properties of highly (00l)-textured $Sb_2Te_3$

films deposited by molecular beam epitaxy. *Journal of Applied Physics*, 115(2), 2014.

[38] B. Yu. Yavorsky, N. F. Hinsche, I. Mertig, and P. Zahn. Electronic structure and transport anisotropy of $Bi_2Te_3$ and $Sb_2Te_3$. *Phys. Rev. B*, 84:165208, Oct 2011.

[39] T. L. Anderson and H. B. Krause. Refinement of the $Sb_2Te_3$ and $Sb_2Te_2Se$ structures and their relationship to nonstoichiometric $Sb_2Te_{3-y}Se_y$ compounds. *Acta Crystallographica Section B*, 30(5):1307–1310, May 1974.

[40] W. Kullmann, J. Geurts, W. Richter, N. Lehner, H. Rauh, U. Steigenberger, G. Eichhorn, and R Geick. Effect of hydrostatic and uniaxial pressure on structural-properties and Raman active lattice-vibrations in $Bi_2Te_3$. *Physica Status Solidi B-Basic Research*, 125(1):131–138, 1984.

[41] M. J. Smith, R. J. Knight, and C. W. Spencer. Poperties of $Bi_2Te_3 - Sb_2Te_3$ Alloys. *Journal of Applied Physics*, 33(7):2186–&, 1962.

[42] H. J. Goldsmid. *Introduction to thermoelectricity*. Springer, Heidelberg New York, 2010.

[43] V. A. Kulbachinskii, Z. M. Dashevskii, M. Inoue, M. Sasaki, H. Negishi, W. X. Gao, P. Lostak, J. Horak, and A. de Visser. Valence-band changes in $Sb_{2-x}In_xTe_3$ and $Sb_2Te_{3-y}Se_y$ by transport and shubnikovde haas effect measurements. *Phys. Rev. B*, 52:10915–10922, Oct 1995.

[44] J. Horak, K. Cermak, and L. Koudelka. Energy formation of antisite defects in doped $Sb_2Te_3$ and $Bi_2Te_3$ crystals. *Journal of Physics and Chemistry of Solids*, 47(8):805 – 809, 1986.

[45] P. Lošák, R. Novotný, J. Horák, and J. Klikorka. Properties of $Sb_2Te_3$, single crystals doped with Ti atoms. *physica status solidi (a)*, 89(1):K55–K59, 1985.

[46] D. M. Rowe and Gao Min. Alpha-plot in sigma-plot as a thermoelectric material performance indicator. *Journal of Materials Science Letters*, 14(9):617–619, 1995.

[47] G. Jeffrey Snyder and Eric S. Toberer. Complex thermoelectric materials. *Nature Materials*, 7(2):105–114, February 2008.

[48] Johannes Kimling. *Transport Phenomena in Thermoelectric and Ferromagnetic Naonostrucures*. PhD thesis, Universität Hamburg - Institut für Angewandte Physik, 2013.

[49] C. Dames and G. Chen. *Thermoelectrics Handbook : Macro to Nano*. CRC Press, 2005.

[50] G. Pernot, M. Stoffel, I. Savic, F. Pezzoli, P. Chen, G. Savelli, A. Jacquot, J. Schumann, U. Denker, I. Mönch, Ch. Deneke, O. G. Schmidt, J. M. Rampnoux, S. Wang, M. Plissonnier, A. Rastelli, S. Dilhaire, and N. Mingo. Precise control of thermal conductivity at the nanoscale through individual phonon-scattering barriers. *Nature Materials*, 9(6):491–495, May 2010.

[51] Kornelius Nielsch, Julien Bachmann, Johannes Kimling, and Harald Böttner. Thermoelectric nanostructures: From physical model systems towards nanograined composites. *Advanced Energy Materials*, 1(5):713–731, October 2011.

[52] M. Hu and D. Poulikakos. Si/Ge Superlattice Nanowires with Ultralow Thermal Conductivity. *Nano Letters*, 12(11):5487–5494, 2012.

[53] B. Poudel, Q. Hao, Y. Ma, Y. Lan, A. Minnich, B. Yu, X. Yan, D. Wang, A. Muto, D. Vashaee, X. Chen, J. Liu, M. S. Dresselhaus, G. Chen, and Z. Ren. High-Thermoelectric Performance of Nanostructured Bismuth Antimony Telluride Bulk Alloys. *Science*, 320(5876):634–638, 2008.

[54] Pooja Puneet, Ramakrishna Podila, Mehmet Karakaya, Song Zhu, Jian He, Terry M. Tritt, Mildred S. Dresselhaus, and Apparao M. Rao. Preferential scattering by interfacial charged defects for enhanced thermoelectric performance in few-layered n-type Bi2Te3. *Scientific Reports*, 3, November 2013.

[55] Christopher J. Vineis, Ali Shakouri, Arun Majumdar, and Mercouri G. Kanatzidis. Nanostructured thermoelectrics: Big efficiency gains from small features. *Advanced Materials*, 22(36):3970–3980, 2010.

[56] Y Takagaki, B Jenichen, U Jahn, M Ramsteiner, K-J Friedland, and J Lähnemann. Hot wall epitaxy of topological insulator films. *Semiconductor Science and Technology*, 26(12):125009, 2011.

[57] T. J. Coutts. *Electrical Conduction in Thin Metal Films*. Elsvier Scientific Publishing Company, 1974.

[58] Baoling Huang, Chris Lawrence, Andrew Gross, Gi-Suk Hwang, Niloufar Ghafouri, Sang-Woo Lee, Hanseup Kim, Chang-Peng Li, Ctirad Uher, Khalil Najafi, and Massoud Kaviany. Low-temperature characterization and micropatterning of coevaporated $Bi_2Te_3$ and $Sb_2Te_3$ films. *Journal of Applied Physics*, 104(11):113710, 2008.

[59] Zhaoquan Zeng, Timothy A. Morgan, Dongsheng Fan, Chen Li, Yusuke Hirono, Xian Hu, Yanfei Zhao, Joon Sue Lee, Jian Wang, Zhiming M. Wang, Shuiqing Yu,

Michael E. Hawkridge, Mourad Benamara, and Gregory J. Salamo. Molecular beam epitaxial growth of $Bi_2Te_3$ and $Sb_2Te_3$ topological insulators on gaas (111) substrates: a potential route to fabricate topological insulator p-n junction. *AIP Advances*, 3(7):–, 2013.

[60] A Giani, A Boulouz, F Pascal-Delannoy, A Foucaran, E Charles, and A Boyer. Growth of Bi2Te3 and Sb2Te3 thin films by MOCVD. *Materials Science and Engineering: B*, 64(1):19–24, September 1999.

[61] D. V. Das, N. Soundararajan, and Manjunatha Pattabi. Electrical conductivity and thermoelectric power of amorphous $Sb_2Te_3$ thin films and amorphous-crystalline transition. *JOURNAL OF MATERIALS SCIENCE*, 22(10):3522–3528, OCT 1987.

[62] M. Winkler, X. Liu, J. D. König, S. Buller, U. Schürmann, L. Kienle, W. Bensch, and H. Böttner. Electrical and structural properties of $Bi_2Te_3$ and $Sb_2Te_3$ thin films grown by the nanoalloying method with different deposition patterns and compositions. *Journal of Materials Chemistry*, 22(22):11323, 2012.

[63] Diefeng Gu, David Nminibapiel, Helmut Baumgart, Hans Robinson, and Vladimir Kochergin. Atomic layer deposition of antimony telluride thin films using $(Me_3Si)_2Te$ with $SbCl_3$ as precursor. *ECS Transactions*, 41(2):255–261, 2011.

[64] Kai Zhang, David Nminibapiel, Madhavi Tangirala, Helmut Baumgart, and Vladimir Kochergin. Fabrication of $Sb_2Te_3$ and $Bi_2Te_3$ multilayer composite films by atomic layer deposition. *ECS Transactions*, 50(13):3–9, 2013.

[65] Y. Takagaki, A. Giussani, J. Tominaga, U. Jahn, and R. Calarco. Transport properties in a Sb-Te binary topological-insulator system. *Journal of Physics: Condensed Matter*, 25(34):345801, 2013.

[66] A. F. Mayadas and M. Shatzkes. Electrical-resistivity model for polycrystalline films: the case of arbitrary reflection at external surfaces. *PHYSICAL REVIEW B*, 1(4):1382–&, 1970.

[67] K. Fuchs. The conductivity of thin metallic films according to the electron theory of metals. *Mathematical Proceedings of the Cambridge Philosophical Society*, 34:100–108, 1 1938.

[68] E. H. Sondheimer. The mean free path of electrons in metals. *Advances in Physics*, 1(1):1–42, 1952.

[69] L. Hicks and M. Dresselhaus. Thermoelectric figure of merit of a one-dimensional conductor. *Physical Review B*, 47(24):16631–16634, June 1993.

[70] M. S. Dresselhaus, G. Dresselhaus, X. Sun, Z. Zhang, S. B. Cronin, and T. Koga. Low-dimensional thermoelectric materials. *Physics of the Solid State*, 41(5):679–682, May 1999.

[71] M. S. Dresselhaus, G. Chen, M. Y. Tang, R. G. Yang, H. Lee, D. Z. Wang, Z. F. Ren, J.-P. Fleurial, and P. Gogna. New directions for low-dimensional thermoelectric materials. *Advanced Materials*, 19(8):1043–1053, April 2007.

[72] Yunki Kim, Antonio DiVenere, George K. L. Wong, J. B. Ketterson, Sunglae Cho, and Jerry R. Meyer. Structural and thermoelectric transport properties of $Sb_2Te_3$ thin films grown by molecular beam epitaxy. *Journal of Applied Physics*, 91(2):715, 2002.

[73] N. Peranio, M. Winkler, Z. Aabdin, J. Koenig, H. Böttner, and O. Eibl. Room temperature MBE deposition of $Bi_2Te_3$ and $Sb_2Te_3$ thin films with low charge carrier densities. *physica status solidi (a)*, 209(2):289–293, February 2012.

[74] L. M. Goncalves, Carlos Couto, Pedro Alpuim, D. Michael Rowe, and J. Higino Correia. Thermoelectric properties of $Bi_2Te_3/Sb_2Te_3$. *Materials Science Forum*, 514 - 516:156–160, 2006.

[75] Tianbao Chen, Ping Fan, Zhuanghao Zheng, Dongping Zhang, Xingmin Cai, Guangxing Liang, and Zhaokun Cai. Influence of substrate temperature on structural and thermoelectric properties of antimony telluride thin films fabricated by RF and DC cosputtering. *Journal of Electronic Materials*, 41(4):679–683, February 2012.

[76] Fan Ping, Zheng Zhuang-Hao, Liang Guang-Xing, Cai Xing-Min, and Zhang Dong-Ping. Composition-dependent characterization of $Sb_2Te_3$ thin films prepared by ion beam sputtering deposition. *Chinese Physics Letters*, 27(8):087201, August 2010.

[77] V.A. Kulbachinskii, A.Yu. Kaminskii, V.G. Kytin, P. Lostak, C. Drasar, and A. Visser. Influence of silver on the galvanomagnetic properties and energy spectrum of mixed $(Bi_{1-x}Sb_x)_2Te_3$ crystals. *Journal of Experimental and Theoretical Physics*, 90(6):1081–1088, 2000.

[78] Raimar Rostek, Vladimir Sklyarenko, and Peter Woias. Influence of vapor annealing on the thermoelectric properties of electrodeposited $Bi_2Te_3$. *Journal of Materials Research*, 26:1785–1790, 8 2011.

[79] Christian Schumacher, Klaus G. Reinsberg, Raimar Rostek, Lewis Akinsinde, Svenja Baessler, Sebastian Zastrow, Geert Rampelberg, Peter Woias, Christophe Detavernier, José A. C. Broekaert, Julien Bachmann, and Kornelius Nielsch. Optimizations of pulsed plated p and n-type $Bi_2Te_3$-based ternary compounds by annealing in different ambient atmospheres. *Advanced Energy Materials*, 3(1):95–104, 2013.

[80] Bacel Hamdou, Johannes Kimling, August Dorn, Eckhard Pippel, Raimar Rostek, Peter Woias, and Kornelius Nielsch. Thermoelectric characterization of bismuth telluride nanowires, synthesized via catalytic growth and post-annealing. *Advanced Materials*, 25(2):239–244, 2013.

[81] Beneq. Ald equipment in general. `http://www.beneq.com/ald-equipment-general.html`. Last accessed on 2014-01-06.

[82] Ultratech/CambridgeNanoTech. Thin film deposition systems. `http://www.cambridgenanotechald.com/thin-film-deposition-systems.html`. Last accessed on 2014-01-06.

[83] Oxford Instruments. Atomic layer deposition (ald). `http://www.oxford-instruments.com/products/etching-deposition-and-growth/plasma-etch-deposition/atomic-layer-deposition`. Last accessed on 2014-01-06.

[84] Picosun. Products. `http://www.picosun.com/en/products/`. Last accessed on 2014-01-06.

[85] Changdeuck Bae, Hyunjung Shin, and Kornelius Nielsch. Surface modification and fabrication of 3D nanostructures by atomic layer deposition. *MRS BULLETIN*, 36(11):887–897, NOV 2011.

[86] R. Zierold and K. Nielsch. Tailor-made, Magnetic Nanotubes by Template-Directed Atomic Layer Deposition. In Elam, JW and Londergan, A and VanDerStraten, O and Roozeboom, F and DeGendt, S and Bent, SF and Delabie, A, editor, *Atomic Layer Deposition Applications 7*, volume 41 of *ECS Transactions*, pages 111–121, 2011. 7th Symposium on Atomic Layer Deposition Applications/220th Meeting of the Electrochemical-Society (ECS), Boston, MA, OCT 10-12, 2011.

[87] Michael A. Weimer, Luis F. Hakim, David M. King, Xinhua Liang, Alan W. Weimer, Steven M. George, Peng Li, and Markus D. Groner. Ultrafast metal-insulator varistors based on tunable $Al_2O_3$ tunnel junctions. *Applied Physics Letters*, 92(16):–, 2008.

[88] Luis F Hakim, Candace L Vaughn, Heather J Dunsheath, Casey S Carney, Xinhua Liang, Peng Li, and Alan W Weimer. Synthesis of oxidation-resistant metal nanoparticles via atomic layer deposition. *Nanotechnology*, 18(34):345603, 2007.

[89] Monan Liu, Xianglin Li, Siva Krishna Karuturi, Alfred Iing Yoong Tok, and Hong Jin Fan. Atomic layer deposition for nanofabrication and interface engineering. *Nanoscale*, 4:1522–1528, 2012.

[90] Shigeharu Morooka, Tatsuya Okubo, and Katsuki Kusakabe. Recent work on fluidized bed processing of fine particles as advanced materials. *Powder Technology*, 63(2):105 – 112, 1990.

[91] Jarod Alan McCormick. *Atomic Layer Deposition on Nanoparticles in a Rotary Reactor*. PhD thesis, University of Colorado, 2007.

[92] Kjell Knapas, Timo Hatanpää, Timo, Mikko Ritala, and Markku Leskelä. In situ reaction mechanism studies on atomic layer deposition of $Sb_2Te_3$ and GeTe from $(Et_3Si)_2Te$ and chlorides. *Chemistry of Materials*, 22(4):1386–1391, February 2010.

[93] Jamie S. Ritch, Tristram Chivers, Mohammad Afzaal, and Paul O'Brien. The single molecular precursor approach to metal telluride thin films: iminobis(diisopropylphosphine tellurides) as examples. *Chem. Soc. Rev.*, 36:1622–1631, 2007.

[94] I. Petrov, P.B. Barna, L. Hultman, and J.E. Greene. Microstructural evolution during film growth. *Journal of Vacuum Science Technology A: Vacuum, Surfaces, and Films*, 21(5):S117–S128, 2003.

[95] Y Takagaki, B Jenichen, U Jahn, Y Manzke, M Ramsteiner, and K-J Friedland. Hot wall epitaxy of $Sb_2Te_3$ layers: coherent hetero-epitaxy on inas(1 1 1) and sb substitution in cu-mediated growth. *Semiconductor Science and Technology*, 28(2):025012, 2013.

[96] David Nminibapiel, Kai Zhang, Madhavi Tangirala, Helmut Baumgart, V. S. K. Chakravadhanula, Christian Kuebel, and Vladimir Kochergin. Microstructure Analysis of ALD $Bi_2Te_3$/$Sb_2Te_3$ Thermoelectric Nanolaminates. In Roozeboom, F and Delabie, A and Londergan, A and DeGendt, S and Elam, JW and VanDerStraten, O, editor, *Atomic Layer Deposition Applications 9*, volume 58 of *ECS Transactions*, pages 59–66. Electrochem Soc; Electrochem Soc, Dielectr Sci & Technol Div; Electrochem Soc, Elect & Photon Div, 2013.

[97] Sebastian Zastrow, Johnnes Gooth, Tim Böhnert, Sonja Heiderich, William Toellner, Stefan Heimann, Stephan Schulz, and Kornelius Nielsch. Thermoelectric transport and hall measurements of low defect $Sb_2Te_3$ăthin films grown by atomic layer deposition. *Semiconductor Science and Technology*, 28(3):035010, 2013.

[98] P. Scherrer. Bestimmung der größe und der inneren struktur von kolloidteilchen mittels röntgenstrahlen. *Nachrichten von der Gesellschaft der Wissenschaften zu Göttingen, Mathematisch-Physikalische Klasse*, 1918:98–100, 1918.

[99] Uwe Holzwarth and Neil Gibson. The scherrer equation versus the "Debye-Scherrer equation". *Nat Nano*, 6(9):534–534, September 2011.

[100] J. I. Langford and A. J. C. Wilson. Scherrer after sixty years: A survey and some new results in the determination of crystallite size. *Journal of Applied Crystallography*, 11(2):102–113, Apr 1978.

[101] J. Lu, Y. Lei, and J. W. Elam. *Noble Metals*. InTech, 2012.

[102] QuantumDesign. Technical support - ppms. `http://www.qdusa.com/techsupport/index.html`. Last accessed on 2014-03-23.

[103] Svenja Bäsler, Tim Böhnert, Johannes Gooth, Christian Schumacher, Eckhard Pippel, and Kornelius Nielsch. Thermoelectric power factor of ternary single-crystalline $Sb_2Te_3$ - and $Bi_2Te_3$ -based nanowires. *Nanotechnology*, 24(49):495402, 2013.

[104] Tim Böhnert, Victor Vega, Ann-Kathrin Michel, Victor M. Prida, and Kornelius Nielsch. Magneto-thermopower and magnetoresistance of single Co-Ni alloy nanowires. *Applied Physics Letters*, 103(9):–, 2013.

[105] Sonja Heiderich. *Investigation on Electrodeposited Bismuth and Bismuth Antimony Thin Films and Nanowires*. PhD thesis, Department of Physics - University of Hamburg, 2013.

[106] M. Stordeur and G. Simon. Investigation of the weak-field charge transport in semiconducting $V_2VI_3$ compounds with trigonal symmetry ii. interpretation of the weak-field charge transport in $Sb_2Te_3$ single crystals. *physica status solidi (b)*, 124(2):799–806, 1984.

[107] Michael Thompson Pettes, Jesse Maassen, Insun Jo, Mark S. Lundstrom, and Li Shi. Effects of surface band bending and scattering on thermoelectric transport in suspended bismuth telluride nanoplates. *Nano Letters*, 13(11):5316–5322, 2013.

[108] Ch. Kittel. *Einführung in die Festkörperphysik*. Olendenbourg Wissenschaftsverlag, 2006.

[109] V A Kulbachinskii, N Miura, H Nakagawa, C Drashar, and P Lostak. Influence of Ti doping on galvanomagnetic properties and valence band energy spectrum of $Sb_{2-x}Ti_xTe_3$ single crystals. *Journal of Physics: Condensed Matter*, 11(27):5273, 1999.

[110] W. Eichler and G. Simon. Galvanomagnetic transport properties of $Sb_2Te_3$. *physica status solidi (b)*, 86(1):K85–K88, 1978.

[111] V. A. Kutasov. *Thermoelectrics Handbook : Macro to Nano - 47*. CRC Press, 2005.

[112] N. F. Hinsche, B. Yu. Yavorsky, I. Mertig, and P. Zahn. Influence of strain on anisotropic thermoelectric transport in $Bi_2Te_3$ and $Sb_2Te_3$. *Phys. Rev. B*, 84:165214, Oct 2011.

[113] John N. Lalena, editor. *Inorganic materials synthesis and fabrication*. Wiley-Interscience, Hoboken, N.J, 2008.

[114] A. von Middendorff, K. Dietrich, and G. Landwehr. Shubnikov-de haas effect in p-type $Sb_2Te_3$. *Solid State Communications*, 13(4):443 – 446, 1973.

[115] M. Stordeur and W. Heiliger. Anisotropy of the thermopower of p-type $Sb_2Te_3$. *physica status solidi (b)*, 78:K103, 1976.

[116] Christian Schumacher, Klaus G. Reinsberg, Lewis Akinsinde, Sebastian Zastrow, Sonja Heiderich, William Toellner, Geert Rampelberg, Christophe Detavernier, José A. C. Broekaert, Kornelius Nielsch, and Julien Bachmann. Optimization of electrodeposited p-doped $Sb_2Te_3$ thermoelectric films by millisecond potentiostatic pulses. *Advanced Energy Materials*, 2(3):345–352, March 2012.

[117] V. Damodara Das and N. Soundararajan. Thermoelectric power and electrical resistivity of crystalline antimony telluride $Sb_2Te_3$ thin films: Temperature and size effects. *Journal of Applied Physics*, 65(6):2332–2341, 1989.

[118] D. A. Anderson and N. Apsley. The hall effect in III-V semiconductor assessment. *Semiconductor Science and Technology*, 1(3):187, 1986.

[119] John H. Davies. *The physics of low-dimensional semiconductor: an introduction*. Cambridge University Press, 2006.

[120] S. Ishiwata, Y. Shiomi, J. S. Lee, M. S. Bahramy, T. Suzuki, M. Uchida, R. Arita, Y. Taguchi, and Y. Tokura. Extremely high electron mobility in a phonon-glass semimetal. *Nat Mater*, 12(6):512–517, June 2013.

[121] D. J. Kim, S. Thomas, T. Grant, J. Botimer, Z. Fisk, and Jing Xia. Surface hall effect and nonlocal transport in SmB6: evidence for surface conduction. *Scientific Reports*, 3, November 2013.

[122] Bacel Hamdou, Johannes Gooth, August Dorn, Eckhard Pippel, and Kornelius Nielsch. Aharonov-Bohm oscillations and weak antilocalization in topological insulator $Sb_2Te_3$ nanowires. *Applied Physics Letters*, 102(22):–, 2013.

[123] Bacel Hamdou, Johannes Gooth, August Dorn, Eckhard Pippel, and Kornelius Nielsch. Surface state dominated transport in topological insulator bi2te3 nanowires. *Applied Physics Letters*, 103(19):–, 2013.

[124] Y. Takagaki, A. Giussani, K. Perumal, R. Calarco, and K.-J. Friedland. Robust topological surface states in $Sb_2Te_3$ layers as seen from the weak antilocalization effect. *Physical Review B*, 86(12), September 2012.

[125] Y. Takagaki, U. Jahn, A. Giussani, and R. Calarco. Multiple state transport deduced by weak antilocalization and electron-electron interaction effects in $Sb_xTe_{1-x}$ layers. *Journal of Physics: Condensed Matter*, 26(9):095802, 2014.

[126] R. A. Smith. *Semiconductors*. Cambridge University Press, 1978.

[127] L.M. L.M. Goncalves, P. Alpuim, A. G. Rolo, and J. H. Correia. Thermal co-evaporation of $Sb_2Te_3$ thin-films optimized for thermoelectric applications. *Thin Solid Films*, 519(13):4152 – 4157, 2011.

[128] Liang He, Faxian Xiu, Xinxin Yu, Marcus Teague, Wanjun Jiang, Yabin Fan, Xufeng Kou, Murong Lang, Yong Wang, Guan Huang, Nai-Chang Yeh, and Kang L. Wang. Surface-dominated conduction in a 6 nm thick $Bi_2Se_3$ thin film. *Nano Letters*, 12(3):1486–1490, 2012.

[129] A. A. Taskin, Satoshi Sasaki, Kouji Segawa, and Yoichi Ando. Manifestation of topological protection in transport properties of epitaxial $Bi_2Se_3$ thin films. *Phys. Rev. Lett.*, 109:066803, Aug 2012.

[130] J. S. Kim, S. S. A. Seo, M. F. Chisholm, R. K. Kremer, H.-U. Habermeier, B. Keimer, and H. N. Lee. Nonlinear hall effect and multichannel conduction in $LaTiO_3/SrTiO_3$ superlattices. *Phys. Rev. B*, 82:201407, Nov 2010.

[131] Patrick A. Lee and T. V. Ramakrishnan. Disordered electronic systems. *Rev. Mod. Phys.*, 57:287–337, Apr 1985.

[132] P. W. Anderson. Absence of diffusion in certain random lattices. *Phys. Rev.*, 109:1492–1505, Mar 1958.

[133] Z. J. Yue, X. L. Wang, Y. Du, S. M. Mahboobeh, Frank F. Yun, Z. X. Cheng, and S. X. Dou. Giant and anisotropic magnetoresistances in p-type Bi-doped $Sb_2Te_3$ bulk single crystals. *EPL (Europhysics Letters)*, 100(1):17014, October 2012.

[134] Hai-Zhou Lu and Shun-Qing Shen. Weak localization of bulk channels in topological insulator thin films. *Phys. Rev. B*, 84:125138, Sep 2011.

[135] Hidekatsu Suzuura and Tsuneya Ando. Crossover from symplectic to orthogonal class in a two-dimensional honeycomb lattice. *Phys. Rev. Lett.*, 89:266603, Dec 2002.

[136] E. McCann, K. Kechedzhi, Vladimir I. Fal'ko, H. Suzuura, T. Ando, and B. L. Altshuler. Weak-localization magnetoresistance and valley symmetry in graphene. *Phys. Rev. Lett.*, 97:146805, Oct 2006.

[137] G. Tkachov and E. M. Hankiewicz. Weak antilocalization in hgte quantum wells and topological surface states: Massive versus massless dirac fermions. *Phys. Rev. B*, 84:035444, Jul 2011.

[138] Kentaro Nomura, Mikito Koshino, and Shinsei Ryu. Topological delocalization of two-dimensional massless dirac fermions. *Phys. Rev. Lett.*, 99:146806, Oct 2007.

[139] Yanfei Zhao, Cui-Zu Chang, Ying Jiang, Ashley DaSilva, Yi Sun, Huichao Wang, Ying Xing, Yong Wang, Ke He, Xucun Ma, Qi-Kun Xue, and Jian Wang. Demonstration of surface transport in a hybrid $Bi_2Se_3$/$Sb_2Te_3$ heterostructure. *Scientific Reports*, 3, October 2013.

[140] H. G. Johnson, S. P. Bennett, R. Barua, L. H. Lewis, and D. Heiman. Universal properties of linear magnetoresistance in strongly disordered mnas-gaas composite semiconductors. *Phys. Rev. B*, 82:085202, Aug 2010.

[141] A. A. Abrikosov. Quantum magnetoresistance of layered semimetals. *Phys. Rev. B*, 60:4231–4234, Aug 1999.

[142] Hong-Tao He, Gan Wang, Tao Zhang, Iam-Keong Sou, George K. L Wong, Jian-Nong Wang, Hai-Zhou Lu, Shun-Qing Shen, and Fu-Chun Zhang. Impurity effect on weak antilocalization in the topological insulator $Bi_2Te_3$. *Phys. Rev. Lett.*, 106:166805, Apr 2011.

[143] Lihong Bao, Liang He, Nicholas Meyer, Xufeng Kou, Peng Zhang, Zhi-gang Chen, Alexei V. Fedorov, Jin Zou, Trevor M. Riedemann, Thomas A. Lograsso, Kang L. Wang, Gary Tuttle, and Faxian Xiu. Weak anti-localization and quan-

tum oscillations of surface states in topological insulator $Bi_2Se_2TeBi2Se2Te$. *Sci. Rep.*, 2, October 2012.

[144] Shao-Pin Chiu and Juhn-Jong Lin. Weak antilocalization in topological insulator $Bi_2Te_3$ microflakes. *Phys. Rev. B*, 87:035122, Jan 2013.

[145] Murong Lang, Liang He, Xufeng Kou, Pramey Upadhyaya, Yabin Fan, Hao Chu, Ying Jiang, Jens H. Bardarson, Wanjun Jiang, Eun Sang Choi, Yong Wang, Nai-Chang Yeh, Joel Moore, and Kang L. Wang. Competing weak localization and weak antilocalization in ultrathin topological insulators. *Nano Letters*, 13(1):48–53, 2013.

[146] Zuocheng Zhang, Xiao Feng, Minghua Guo, Yunbo Ou, Jinsong Zhang, Kang Li, Lili Wang, Xi Chen, Qikun Xue, Xucun Ma, Ke He, and Yayu Wang. Transport properties of $Sb_2Te_3/Bi_2Te_3$ topological insulator heterostructures. *physica status solidi (RRL) Rapid Research Letters*, 7(1-2):142–144, 2013.

[147] P. Arun and A. G. Vedeshwar. Influence of grain size on the electrical properties of $Sb_2Te_3$ polycrystalline films. *eprint arXiv:cond-mat/0408116*, August 2004.

[148] Carl.V. Thompson and Roland Carel. Texture development in polycrystalline thin films. *Materials Science and Engineering: B*, 32(3):211 – 219, 1995. Containing papers presented at the Indo-US Workshop on Nucleation and Growth in Solids.

[149] Melvin Cutler and N. F. Mott. Observation of anderson localization in an electron gas. *Phys. Rev.*, 181:1336–1340, May 1969.

[150] Joseph P. Heremans, Vladimir Jovovic, Eric S. Toberer, Ali Saramat, Ken Kurosaki, Anek Charoenphakdee, Shinsuke Yamanaka, and G. Jeffrey Snyder. Enhancement of thermoelectric efficiency in PbTe by distortion of the electronic density of states. *Science*, 321(5888):554–557, 2008.

[151] P Gonzalez, J A Agapito, and D Pardo. Two-band model parameters deduced from hall coefficient measurements in polycrystalline films of snte. *Journal of Physics C: Solid State Physics*, 19(6):899, 1986.

[152] T.C. Harman, B. Paris, S.E. Miller, and H.L. Goering. Preparation and some physical properties of $Bi_2Te_3$, $Sb_2Te_3$, and $As_2Te_3$. *Journal of Physics and Chemistry of Solids*, 2(3):181 – 190, 1957.

[153] B. Rönnlund, O. Beckman, and H. Levy. Doping properties of $Sb_2Te_3$ indicating a two valence band model. *Journal of Physics and Chemistry of Solids*, 26(8):1281 – 1286, 1965.

[154] Tik Sun, Bo Yao, Andrew P. Warren, Katayun Barmak, Michael F. Toney, Robert E. Peale, and Kevin R. Coffey. Surface and grain-boundary scattering in nanometric Cu films. *Phys. Rev. B*, 81:155454, Apr 2010.

[155] F. Völklein and E. Kessler. Temperature and thickness dependence of electrical and thermal transport coefficients of $Bi_{1-x}Sb_x$ films in an anisotropic, non-degenerate two-band model. *physica status solidi (b)*, 134(1):351–362, 1986.

[156] U. Dillner and F. Völklein. Transport properties of flash-evaporated $(Bi_{1-x}Sb_x)_2Te_3$ films ii: Theoretical analysis. *Thin Solid Films*, 187(2):263 – 273, 1990.

[157] Andreas Schmitz. *Bleitellurid mit erhöhter mechanischer Stabilität für zylindrische thermoelektrische Generatoren*. PhD thesis, RWTH Aachen University, 2013.

[158] Roberto Orru, Roberta Licheri, Antonio Mario Locci, Alberto Cincotti, and Giacomo Cao. Consolidation/synthesis of materials by electric current activated/assisted sintering. *Materials Science and Engineering: R: Reports*, 63(4-6):127 – 287, 2009.

[159] R Mansfield and W Williams. The electrical properties of bismuth telluride. *Proceedings of the Physical Society*, 72(5):733, 1958.

[160] S. Sumithra, Nathan J. Takas, Dinesh K. Misra, Westly M. Nolting, P.F.P. Poudeu, and Kevin L. Stokes. Enhancement in thermoelectric figure of merit in nanostructured $Bi_2Te_3$ with semimetal nanoinclusions. *Advanced Energy Materials*, 1(6):1141–1147, 2011.

[161] N. F. Hinsche, B. Yu. Yavorsky, M. Gradhand, M. Czerner, M. Winkler, J. König, H. Böttner, I. Mertig, and P. Zahn. Thermoelectric transport in $Bi_2Te_3/Sb_2Te_3$ superlattices. *Phys. Rev. B*, 86:085323, Aug 2012.

[162] Yucheng Lan, Austin Jerome Minnich, Gang Chen, and Zhifeng Ren. Enhancement of thermoelectric figure-of-merit by a bulk nanostructuring approach. *Advanced Functional Materials*, 20(3):357–376, February 2010.

[163] J. Lybeck, M. Valkeapaa, S. Shibasaki, I. Terasaki, H. Yamauchi, and M. Karppinen. Thermoelectric Properties of Oxygen-Tuned ALD-Grown [Ca2CoO3](0.62)[CoO2] Thin Films. *CHEMISTRY OF MATERIALS*, 22(21):5900–5904, NOV 9 2010.

[164] Kai Zhang, Arun Deepak Ramalingom Pillai, David Nminibapiel, Madhavi Tangirala, Venkata S Chakravadhanula, Christian Kübel, Helmut Baumgart, and

Vladimir Kochergin. Ald growth of pbte and pbse superlattices for thermoelectric applications. *ECS Transactions*, 58(10):131–139, 2013.

[165] Q. Xiao, Y. Lu, J. Wang, and M. Zhang. Homogeneous thermoelectric nanocomposite using core-shell nanoparticles, April 17 2008. US Patent App. 11/549,203.

[166] M.P. Rowe and M. Zhang. Core-shell nanoparticles and process for producing the same, September 2 2010. WO Patent App. PCT/US2010/025,148.

[167] Y. C. Dou, X. Y. Qin, D. Li, L. L. Li, T. H. Zou, and Q. Q. Wang. Enhanced thermopower and thermoelectric performance through energy filtering of carriers in (bi2te3)0.2(sb2te3)0.8 bulk alloy embedded with amorphous sio2 nanoparticles. *Journal of Applied Physics*, 114(4):–, 2013.

[168] O.N. Ivanov, O.N. Maradudina, and R.A. Lyubushkin. Electric conductivity of a bulk composite based on bi2te3/sio2 core-shell nanoparticles. *Technical Physics Letters*, 40(1):65–68, 2014.

[169] Marcus Scheele, Niels Oeschler, Katrin Meier, Andreas Kornowski, Christian Klinke, and Horst Weller. Synthesis and thermoelectric characterization of bi2te3 nanoparticles. *Advanced Functional Materials*, 19(21):3476–3483, 2009.

[170] Li-Dong Zhao, Bo-Ping Zhang, Wei-Shu Liu, and Jing-Feng Li. Effect of mixed grain sizes on thermoelectric performance of bi2te3 compound. *Journal of Applied Physics*, 105(2):–, 2009.

# List of Figures

# Chapter 9

# Appendix

## 9.1 Error discussion

### 9.1.1 Error of the Seebeck coefficient $S$ for thin film measurements

The Seebeck coefficient is a function of the temperature gradient $\Delta T$ and the thermovoltage $V_{\text{te}}$. For reasonable small temperature gradients, the linear Seebeck approximation $S = \frac{V_{\text{te}}}{\Delta T}$ is valid. However, small temperature gradients means large uncertaincies in the temperature measurements. To minimize the error, the Seebeck coefficients have been evaluated by the linear approximation for different temperature gradients according to different heater voltages (see figure 5.8). However, the linear approximation is reasonable, to use the error of the linear regression would mean to neglect the high error of the calculated temperature difference. Although, the error of every Seebeck value individually calculated with the corresponding temperature gradient $S_{\text{in}}$ is much larger then the error of the Seebeck calculated with the linear regression method $S_{\text{lr}}$, we can estimate this as the upper border for the error of $S$

$$\delta S = \underbrace{\left| \frac{\partial S}{\partial \Delta T} \right| \cdot \delta \Delta T}_{\text{error component} \Delta T} + \underbrace{\left| \frac{\partial S}{\partial V_{\text{te}}} \right| \cdot \delta V_{\text{te}}}_{\text{error component} V_{\text{te}}} . \tag{9.1}$$

The error of the temperature $\delta \Delta T$ gradient is a function of the second order polynomial ($T = a \cdot R^2 + b \cdot R + c$) and the error of the resistance measurement itself

$$\delta \Delta T = \left| \frac{\partial T_1(R_1)}{\partial R_1} \right| \cdot \delta R_1 + \left| \frac{\partial T_2(R_2)}{\partial R_2} \right| \cdot \delta R_2. \tag{9.2}$$

Since both resistance dependence on temperature is quite similar, we can find the error of $\delta\Delta T$ to

$$\delta\Delta T \approx 2 \cdot (2 \cdot a \cdot R + b) \cdot \delta R \approx 2 \cdot (0.003 \cdot R + 2.5) \cdot 0.005, \qquad (9.3)$$

where $\delta R = 0.005$ (assumed to be constant with $T$), because the resistance is averaged over 10 measurement for each step. However the error of $\Delta T$ seems to be small at RT, the error is dominant especially for lower temperature. Since the maximum temperature gradient decreases fast with decreasing $T$ due to the lower heater resistance and the decreasing device resistance (see figure 5.7). The error of the thermovoltage
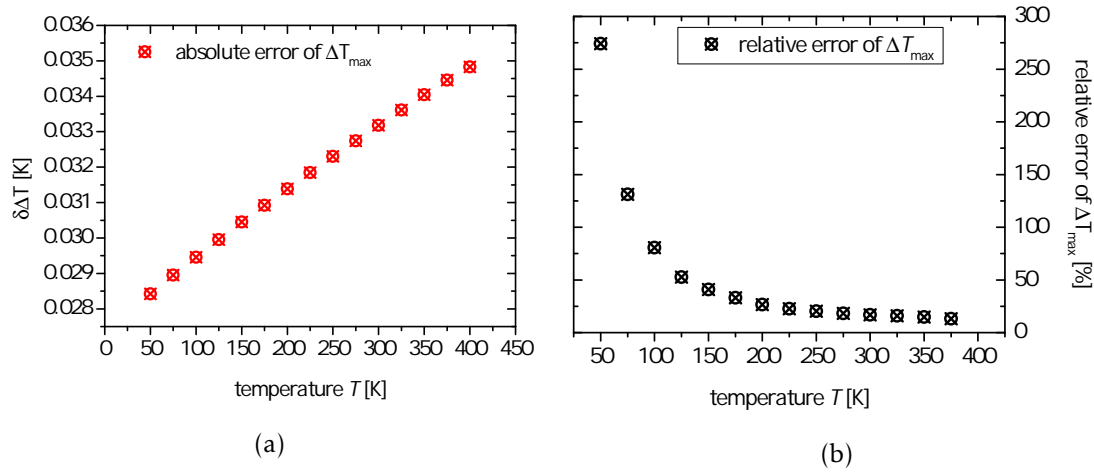


Figure 9.1

increases with decreasing temperature, since the Seebeck coefficient decreases. However, since the thermovoltage is averaged over 20 points for each step, the error is much smaller then the error of the temperature gradient. So we can find $\delta S$ with using

$$\left| \frac{\partial S}{\partial \Delta T} \right| \cdot \delta\Delta T >> \left| \frac{\partial S}{\partial V_{\text{te}}} \right| \cdot \delta V_{\text{te}}, \qquad (9.4)$$

to

$$\delta S = \frac{V_{\text{te}}}{(\Delta T)^2} \cdot 2 \cdot (0.003 \cdot R + 2.5) \cdot 0.005 \qquad (9.5)$$

### 9.1.2 Error of the electrical conductivity $\sigma$ for thin film measurements

The error of the electrical conductivity is dominated by the error of the thin film thickness $t$. The geometry of the ALD thin film as well as the contact structure dimensions are patterned by photolithography with an error of about $1/10\,\mu\text{m}$ giving an approxi-
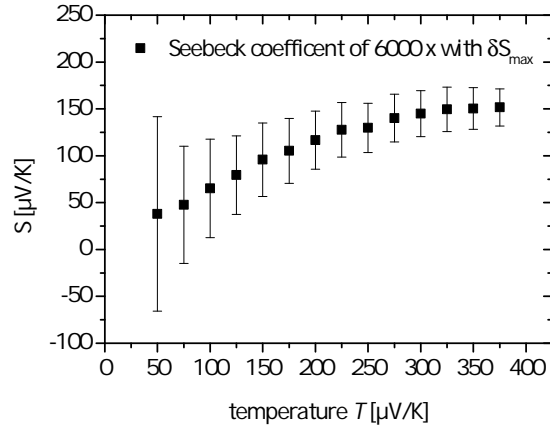
**Figure 9.2:** $S$ of 6000 cycle film with the maximal error $\delta S_{\mathrm{max}}$ according to equation 9.4

mal structural error in $d/b$ (distance between the voltage contacts and with of the film respectively) of maximal 1%. Since also the resistance error is in that range, the thin film growth rate as well as the uncertaincies due to the surface roughness have the highest influence on the calculation of both parameters. We can find for the error $\delta\sigma$

$$\delta\sigma = \left|\frac{\partial\sigma}{\partial t}\right| \cdot \delta t + \left|\frac{\partial\sigma}{\partial R}\right| \cdot \delta R + \left|\frac{\partial\sigma}{\partial b}\right| \cdot \delta b + \left|\frac{\partial\sigma}{\partial d}\right| \cdot \delta d. \tag{9.6}$$

Since all errors are neglectabelly small in comparison to the thickness error, we can find

$$\delta\sigma \approx \left|\frac{\partial\sigma}{\partial t}\right| \cdot \delta t = \frac{1}{R_{\mathrm{film}}}\frac{b}{d}\frac{1}{t^2} \cdot \delta t. \tag{9.7}$$

If we assume the the growth rate to $0.016\,\mathrm{nm/cycle} \pm 0.004\,\mathrm{nm/cycle}$ the error is

$$\delta\sigma \approx \frac{10}{R_{\mathrm{film}}}\frac{1}{t^2} \cdot 0.004\,\mathrm{nm} \cdot \mathrm{cycle}. \tag{9.8}$$

Since the geometry is fixed for every sample/device, the error of the conductivity $\delta\sigma$ is a function of the thin film thickness (number of ALD cycles) and the thin film resistance

### 9.1.3 Error of the Hall coefficient $R_{\mathrm{H}}$ for thin film measurements

Similar to the error of the conductivity, the error of the of the Hall coefficient is dominated by the error of the thickness $t$. The overall error $\delta R_{\mathrm{H}}$ is

$$\delta R_{\mathrm{H}} = \left|\frac{\partial R_{\mathrm{H}}}{\partial t}\right| \cdot \delta t + \left|\frac{\partial R_{\mathrm{H}}}{\partial R_{xy}}\right| \cdot \delta R_{xy} + \left|\frac{\partial R_{\mathrm{H}}}{\partial B}\right| \cdot \delta B. \tag{9.9}$$

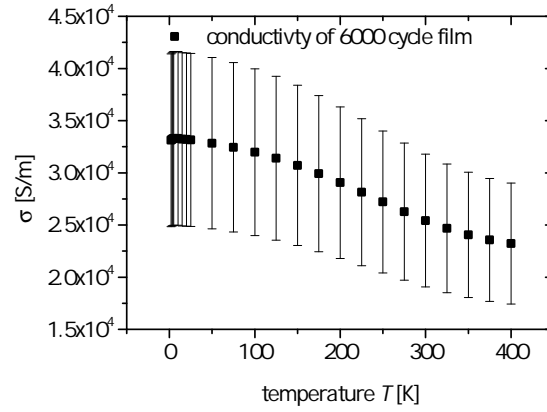**Figure 9.3:** $\sigma$ of 6000 cycle film with the maximal error $\delta\sigma$ according to equation 9.8.

Using the approximation of the dominating thickness error, we can find

$$\delta R_{\mathrm{H}} = \left| \frac{\partial R_{\mathrm{H}}}{\partial t} \right| \cdot \delta t = R_{\mathrm{Hall}} \frac{1}{t^2} \cdot \delta t \qquad (9.10)$$
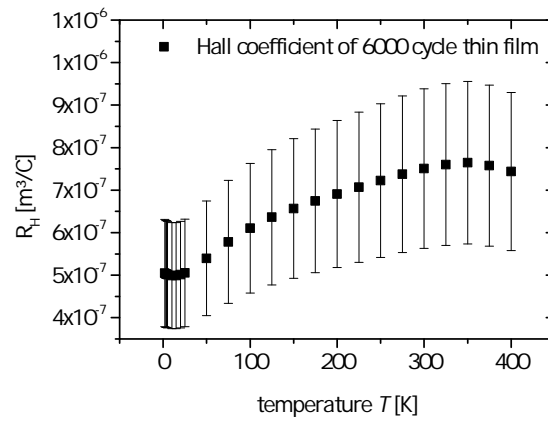


**Figure 9.4:** $R_{\mathrm{H}}$ of 6000 cycle film with the maximal error $\delta R_{\mathrm{H}}$ according to equation 9.10.

## 9.2 further information

| Sb in A% | Te in A% | Sb:SbTe in % | Te:SbTe in % | sample | cycles |
|---|---|---|---|---|---|
| 19,92 | 32,41 | 38,07 | 61,93 | unknown | unknown |
| 20,15 | 32,38 | 52,53 | 38,36 | unknown | unknown |
| 20,25 | 31,02 | 39,50 | 60,50 | unknown | unknown |
| 4,17 | 6,33 | 39,71 | 60,29 | 23 | unknown |
| 3,76 | 5,21 | 41,92 | 58,08 | 23 | unknown |
| 2,72 | 3,6 | 43,04 | 56,96 | 23 | unknown |
| 13,25 | 21,07 | 38,61 | 61,39 | 23 | unknown |
| 12,41 | 18,03 | 40,77 | 59,23 | 23 | unknown |
| 9,23 | 12,82 | 41,86 | 58,14 | 23 | unknown |
| 7,71 | 11,27 | 40,62 | 59,38 | 22 | unknown |
| 7,67 | 11,91 | 39,17 | 60,83 | 22 | unknown |
| 7,83 | 12,01 | 39,47 | 60,53 | 22 | unknown |
| 10,55 | 14,87 | 41,50 | 58,50 | 22 | unknown |
| 4,53 | 14,87 | 41,50 | 58,50 | 22 | unknown |
| 5,62 | 8,79 | 39,04 | 60,96 | 22 | unknown |
| 5,59 | 8,74 | 39,01 | 60,99 | 22 | unknown |
| 5,32 | 8,73 | 37,86 | 62,14 | 22 | unknown |
| 38,75 | 61,25 | 38,75 | 61,25 | 72 | 3000 |
| 0,53 | 0,79 | 40,15 | 59,85 | 57 | 2500 |
| average and standard deviation | | 39,96 | 60,04 | $\pm$ 1,50 | |

**Table 9.1:** EDX results of different measurement points and sample thicknesses of ALD grown $Sb_2Te_3$ on Si/$SiO_2$ substrates. Only measurements with high enough overall counts have been taken into account.
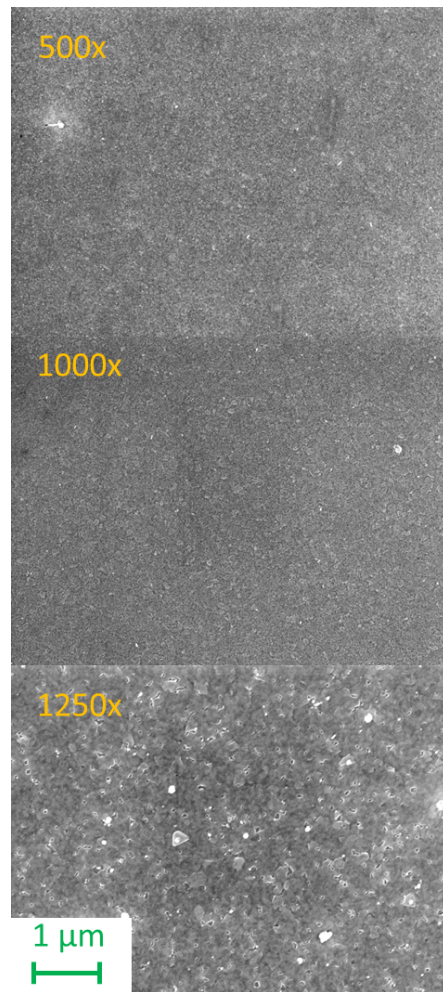
**Figure 9.5:** Different number of ALD cycles of $Sb_2Te_3$ on GaAs substrates. The growth can be found to be quite similar to the growth on $Si/SiO_2$ substrates, although the lattice parameter is different.
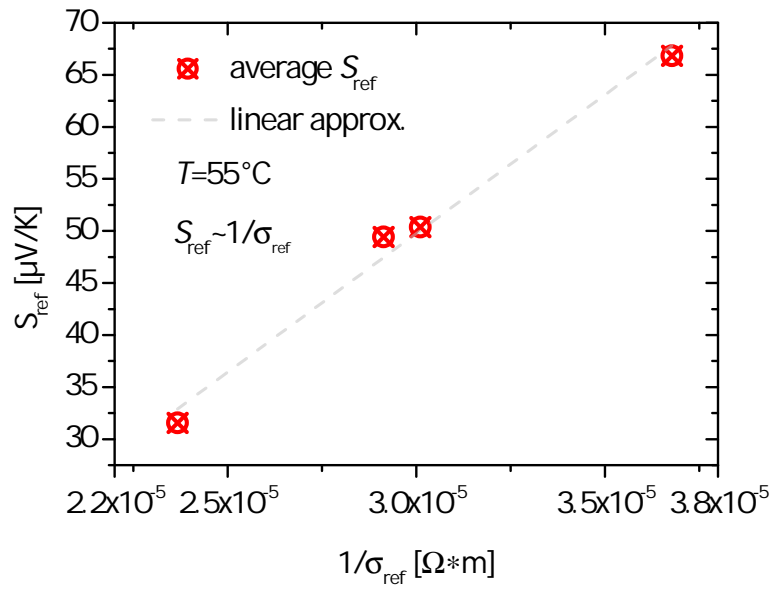
**Figure 9.6:** Seebeck coefficient of the $Bi_2Te_3$ reference sample $S_{ref}$ against $1/\sigma$ at 55 °C and the linear approximation indicating the doping regime.
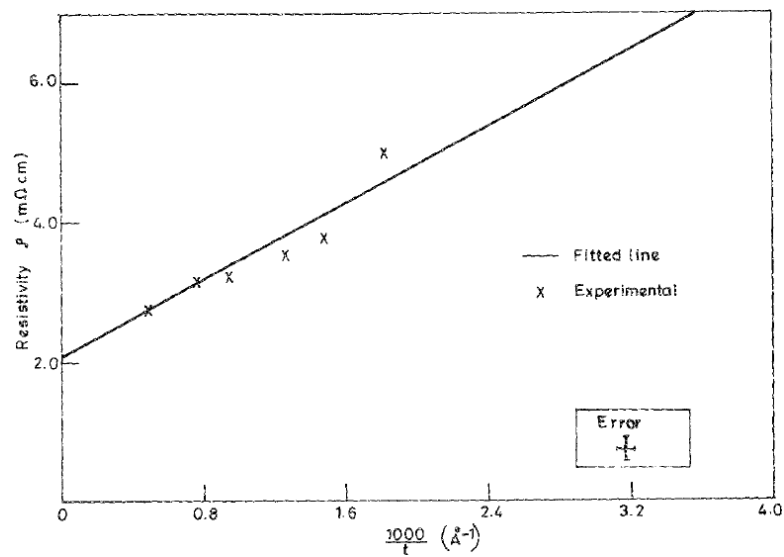


**Figure 9.7:** Linear approximation of the increase of the resistivity with decreasing thickness of co-evaporated $Sb_2Te_3$ thin films by Das *et al.* out of [61].

# List of Publications

1. G. Dennler, R. Chmielowski, S. Jacob, F. Capet, P. Roussel, S. Zastrow and Nielsch, Kornelius and Opahle, Ingo and Madsen, Georg K. H., Are Binary Copper Sulfides/Selenides Really New and Promising Thermoelectric Materials? *Advanced Energy Materials*, doi 10.1002/aenm.201301581, 2014.

2. S. Heiderich, W. Töllner, T. Böhnert, J. G. Gluschke, S. Zastrow, K. Nielsch, Magnetotransport and thermopower of single $Bi_{0.92}Sb_{0.08}$ nanowires, *physica status solidi (RRL) Rapid Research Letters*, vol. 7, no. 10, pp. 898–902, 2013.

3. G. Bendt, S. Schulz, S. Zastrow, K. Nielsch, Single-Source Precursor-Based Deposition of $Sb_2Te_3$ Films by MOCVD *Chemical Vapor Deposition*, vol. 19, no. 7-8-9, pp. 235–241, 2013.

4. S. Zastrow, J. Gooth, T. Böhnert, S. Heiderich, S. Schulz, S. Heimann K. Nielsch, Thermoelectric transport and Hall measurements of low defect $Sb_2Te_3$ thin films grown by atomic layer deposition, *Semiconductor Science and Technology*, vol. 28, no. 3, pp. 035010, 2013.

5. KG. Reinsberg, C. Schumacher, S. Zastrow, K. Nielsch, J. A. C. Broekaert, U. E. A. Fittschen, Investigation on the homogeneity of pulsed electrochemically deposited thermoelectric films with synchrotron mu-XRF, mu-XRD and mu-XANES, *Journal of Materials Chemistry A*, vol. 1, no. 13, pp. 4215-4220, 2013.

6. C. Schumacher, KG. Reinsberg, R. Rostek, L. Akinsinde, S. Baessler, S. Zastrow, C. Detavernier, J. A. C. Broekaert, J. Bachmann, K. Nielsch, Optimizations of Pulsed Plated p and n-type $Bi_2Te_3$-Based Ternary Compounds by Annealing in Different Ambient Atmospheres, *Advanced Energy Materials*, vol. 3, no. 1, pp. 95–104, 2013.

7. C. Schumacher, KG. Reinsberg, L. Akinsinde, S. Zastrow, S. Heiderich, C. Detavernier, W. Töllner, G. Rampelberg, C. Detavernier, J. A. C. Broekaert, K. Nielsch, J. Bachmann, Optimization of Electrodeposited p-Doped $Sb_2Te_3$ Thermoelectric

Films by Millisecond Potentiostatic Pulses, *Advanced Energy Materials*, vol. 2, no. 3, pp.345–352, 2012.

8. A. Sesselmann, T. Dasgupta, K. Kelm, E. Müller, S. Perlt, S. Zastrow, Transport properties and microstructure of indium-added cobalt-antimony-based skutterudites, *Journal of Materials Research*, vol. 26, no. 15, pp.1820-1826, 2011.